

DOCTORAL DISSERTATION

**STUDY ON  
PLANAR-TYPE FERROMAGNETIC NANOSCALE DEVICES  
FABRICATED BY  
NOVEL NANOFABRICATION TECHNIQUES**

A DISSERTATION SUBMITTED IN PARTIAL FULFILLMENT  
OF THE REQUIREMENTS FOR THE DEGREE  
OF  
DOCTOR OF ENGINEERING

February, 2010

**Presented by Yusuke Tomoda**

**Directed by Associate Professor Jun-ichi Shirakashi**

Department of Electronic and Information Engineering  
Graduate School of Engineering  
Tokyo University of Agriculture and Technology

# *Preface*

Ferromagnetic single-electron transistors (FMSETs) have attracted much interest as novel functional devices. Since ultra-small ferromagnetic tunnel junctions have the tunability of the interplay of spin and charge, FMSETs are able to control the modulation amplitude of the tunnel magnetoresistance (TMR). In *RC*-coupled FMSETs, several metastable charge states within the Coulomb blockade range cause a clear hysteresis of TMR, suggesting the multivalued functions of the device. For the fabrication of the FMSETs, novel lithography techniques are also required because of the nanometer-scale dimensions of the devices. We have investigated the novel nanofabrication techniques using scanning probe microscopy (SPM) and electromigration (EM). In these methods, one can easily obtain insulating barrier with a feature size of around several nm, which strongly suggests that lateral or planar-type ferromagnet/insulator/ferromagnet (FM/I/FM) tunnel junctions can be obtained using this unique fabrication process.

The reaction mechanism of the SPM local oxidation is considered to be anodic oxidation, and this oxidation process proceeds through an electrochemical reaction driven by a negative bias voltage applied to the SPM tip. The voltage applied to the tip-sample junction results in a high electric field, which attracts a stable water meniscus from the water absorbed on the sample surface to the tip-sample junction. Thus the high electric field creates oxyanions from water molecules, and transports these oxyanions through the growing oxide film. In this dissertation, we study the electrical and magnetoresistive properties of planar-type Ni-Ni oxide-Ni ferromagnetic tunnel junctions, which are the basic single-barrier structure of the FMSETs. In order to induce

magnetic shape anisotropy, Ni channels were constricted by focused ion beam and photolithography before formation of Ni oxide barriers. The resistance of planar-type Ni-Ni oxide-Ni ferromagnetic tunnel junction was change by applying a magnetic field, and magnetoresistance (MR) ratio exhibited above 100 % at 16 K. With increasing the bias voltage at 16 K, the MR ratio was decreased. Furthermore, the MR ratio at 0.5 mV decreases with increasing the measurement temperature. This result implies that planar-type ferromagnetic tunnel junctions have potential use as nanoscale magnetoresistive elements.

We propose a stepwise feedback-controlled electromigration (SFCE) for the fabrication of planar-type Ni-Vacuum-Ni ferromagnetic tunnel junctions. Electromigration, which is refers to the transport of mass in conducting subjects induced by large current density, has been known to be a major failure mode of integrated circuits. Using the SFCE approach, a wide-range control of the resistance of metal nanowires was achieved ranging from metallic regime to tunneling regime without catastrophic breaks of the nanowires. Tunneling properties were obtained from the devices formed by SFCE technique. Moreover, MR ratio of approximately 4 % also exhibited at 16 K. These results imply that the nanogaps fabricated by SFCE procedure act as vacuum tunnel barriers in planar-type ferromagnetic tunnel junctions.

We have also investigated novel technique using electromigration for the fabrication of nanogaps with separation of less than 10 nm. This technique is based on the motion of atoms caused by field-emission-induced electromigration (activation). The tunnel resistance of the nanogaps was controlled by the magnitude of the preset current during activation procedure and decreased from the order of 100 T $\Omega$  to 100 k $\Omega$  with increasing the preset current from 1 nA to 150  $\mu$ A. The nanogaps formed by this

technique act as vacuum tunnel barriers in planar-type ferromagnetic tunnel junctions. The resistance of planar-type Ni-Vacuum-Ni ferromagnetic tunnel junctions was changed by applying a magnetic field, and MR ratio exhibited above 300 % at 16 K. Furthermore, the devices formed by the activation with the preset current from 100 nA to 1.5  $\mu$ A exhibited Coulomb blockade phenomena at room temperature. Coulomb blockade voltage of the devices was clearly modulated by the gate voltage quasi-periodically, resulting in the formation of multiple tunnel junctions of the SETs at room temperature. With increasing the preset current, the charging energy of the SETs was decreased from 1030 meV to 320 meV. These results strongly suggest that the activation technique is possible to fabricate planar-type ferromagnetic tunnel devices with vacuum tunnel barriers.

# Table of Contents

<i>Preface</i> .....	i
<b>Chapter 1 Overview and Objective of This Research</b> .....	1
<b>Chapter 2 Theoretical Prospects of Ferromagnetic Single-Electron Transistors</b> .....	7
2.1 Introduction .....	7
2.2 Fundamental Characteristics of SET.....	9
2.3 C-coupled FMSET with Multiple Tunnel Junctions.....	16
2.4 R-coupled FMSET .....	24
2.5 RC-coupled FMSET .....	30
2.6 Summary.....	38
<b>Chapter 3 Novel Nanofabrication Techniques for Nanoscale Tunnel Devices</b> .....	39
3.1 Introduction .....	39
3.2 Scanning Probe Microscopy Local Oxidation .....	40
3.3 Stepwise Feedback-Controlled Electromigration .....	47
3.4 Field-Emission-Induced Electromigration .....	58
3.5 Summary.....	72
<b>Chapter 4 Planar-Type Ni-Ni oxide-Ni Ferromagnetic Tunnel Junctions Obtained by Scanning Probe Microscopy Local Oxidation</b> .....	73
4.1 Introduction .....	73
4.2 Planar-Type Ni-Ni oxide-Ni ferromagnetic Tunnel Junctions .....	74
4.3 Magnetoresistance Properties .....	77
4.3.1 Channel Constriction Using Focused Ion Beam .....	77
4.3.1.1 Devices with Constricted Channel Width of 1.5 $\mu\text{m}$ .....	77
4.3.1.2 Devices with Constricted Channel Width of 800 nm .....	83

4.3.2 Channel Constriction Using Photolithography.....	88
4.3.2.1 Devices with Constricted Channel Width of 500 nm .....	88
4.3.2.2 Devices with Constricted Channel Width of 120 nm .....	92
4.4 Comparison of Constriction Methods.....	96
4.5 Summary.....	99
<b>Chapter 5 Stepwise Feedback-Controlled Electromigration for Fabrication of Planar-Type Ni-Vacuum-Ni Ferromagnetic Tunnel Junctions .....</b>	<b>100</b>
5.1 Introduction .....	100
5.2 Micromagnetic Simulation .....	102
5.3 Planar-Type Ni-Vacuum-Ni Ferromagnetic Tunnel Junctions Fabricated by SFCE Technique.....	107
5.3.1 Asymmetrical Butterfly-Shape Electrodes .....	107
5.3.2 Asymmetrical Broad Bean-Shape Electrodes.....	114
5.4 Summary.....	118
<b>Chapter 6 Formation of Planar-Type Ni-Vacuum-Ni Ferromagnetic Tunnel Junctions Using Field-Emission-Induced Electromigration .....</b>	<b>119</b>
6.1 Introduction .....	119
6.2 Micromagnetic Simulation .....	120
6.3 Planar-Type Ni-Vacuum-Ni Ferromagnetic Tunnel Junctions Fabricated by Activation Technique.....	126
6.3.1 Asymmetrical Butterfly-Shape Electrodes with the Size of 720×500 nm <sup>2</sup> .....	126
6.3.2 Asymmetrical Butterfly-Shape Electrodes with the Size of 1440×1000 nm <sup>2</sup> .....	136
6.4 Summary.....	141
<b>Chapter 7 Planar-Type Single-Electron Transistors Produced by Field-Emission-Induced Electromigration .....</b>	<b>142</b>
7.1 Introduction .....	142
7.2 Experimental Procedure.....	144

7.3 Drain Current-Drain Voltage Properties @ RT.....	148
7.4 Drain Current-Drain Voltage Properties @ 16 K.....	154
7.5 Summary.....	158
<b>Chapter 8 General Conclusions .....</b>	<b>159</b>
8.1 Planar-Type Ni-Ni oxide-Ni Ferromagnetic Tunnel Junctions Obtained by SPM Local Oxidation .....	159
8.2 Stepwise Feedback-Controlled Electromigration for Fabrication of Planar-Type Ni-Vacuum-Ni Ferromagnetic Tunnel Junctions .....	160
8.3 Formation of Planar-Type Ni-Vacuum-Ni Ferromagnetic Tunnel Junctions Using Field-Emission-Induced Electromigration .....	160
8.4 Planar-Type Single-Electron Transistors Produced by Field- Emission-Induced Electromigration .....	161
8.5 Summary.....	162
<b>Acknowledgements.....</b>	<b>163</b>
<b>References .....</b>	<b>164</b>
<b>List of Publications.....</b>	<b>174</b>

# Chapter 1

## Overview and Objective of This Research

60 years ago, the Shockley group at Bell Laboratories was frantically attempting to prove the concept of the field-effect transistor [1, 2]. The revolutionary idea promoted by Shockley was that a (metal) gate, placed in the close vicinity of a semiconductor material, can induce a charge in the surface conductivity. In order for such a conductivity modulation to be discernible, a very thin semiconductor slab was needed as well as two pressure probes serving as drain and source contacts. The first transistor consisted of a thin Ge slab, gate SiO<sub>2</sub> insulator, and an Au gate. After a series of more or less successful attempts and manipulation hazards, Bardeen, Brattain, and Shockley ended up demonstrating transistor action and brilliantly elucidating its secret: the predictable metal oxide semiconductor (MOS) transistor turned out to operate as a bipolar transistor.

MOS field effect transistor (MOSFET) devices have dominated computer technologies for several reasons including their low operating voltages, low power consumption, high speed and the ease with which they have been scaled down in dimension. Indeed, in the past MOSFETs could be scaled down simply by shrinking each component part by a constant factor and operating the devices as usual. Unfortunately, it is not at all certain that the operating principles of the MOSFET will scale as the size decreases even below 10 nm. As the n-p-n regions in the transistor shrink, their ability to control the flow of electrons is overcome by the quantum mechanical probability that the electrons simply tunnel through the n-p interface. Furthermore, as the transistor density increases, the probability that an electron can



tunnel between neighboring transistors increases. These tunneling processes cause error in data manipulation and storage. There is also concern that as the size of a MOSFET decreases, the ability to make any two transistors with the same electronic properties will be lost.

In the scaling of complementary MOS (CMOS) transistors into the deep sub-10 nm regime, both fundamental limits and technological challenges are encountered. In order to extend the prodigious progress of large scale integration (LSI) performance in this regime, it is essential to introduce into future LSIs new devices having an operation principle, which is more effective at smaller dimensions than is the operation principle currently employed. Single-electron transistors (SETs) are promising candidate for new nano-scale devices, because SETs has the good scalability as well as the low-power property.

On the other hand, magnetoresistance is one of several relatively new phenomena that have contributed to the growth of the young field of 'spintronics'. Spintronics can be defined as the art and science of utilizing the spin of the electron (as well as its charge) to accomplish some purpose. The birth of spintronics can be dated from 1988 when groups led by Albert Fert and Peter Grünberg independently discovered the phenomenon of giant magnetoresistance (GMR) [3, 4]. Their contribution was recognized at 2007 by the award of the Nobel Prize in physics. GMR is a change in the resistance of a magnetically inhomogeneous material when an applied magnetic field brings the magnetic moments of the material into alignment. The magnetically inhomogeneous system usually consists of a magnetic multilayer in which the layers are typically a few nanometers in thickness. It is useful and customary to divide GMR into two major types, Current in the Plane (CIP) GMR and Current Perpendicular to the

Plane (CPP) GMR. The physics of these two types of GMR are quite different. The type of GMR first observed by the teams led by Fert and Grünberg is CIP GMR.

Tunnel Magnetoresistance (TMR) is geometrically similar to CPP-GMR. The difference is that the nonmagnetic metallic spacer layer is replaced by an insulator or semiconductor. It would appear that band-matching between one of the spin-channels and the spacer layer (the origin of CPP GMR) can no longer occur because there are no bands at the Fermi energy in an insulator. For this reason (as will be described below) the theory of TMR was based on the Fermi energy density of states of the ferromagnetic electrodes. Somewhat surprisingly, as will also be described below, it turns out that a new and different kind of band matching can occur and this can be used to achieve a very large ratio of tunneling conductance between parallel and anti-parallel alignment of the spins.

Tunneling magnetoresistance was first reported by Julliere in 1975 [5]. Julliere made a Co–Ge–Fe sandwich and measured the change in electrical resistance on switching the relative alignment of the Co and Fe magnetic moments from parallel to anti-parallel. He reported a 14% increase in resistance at a temperature of 4.2 K. This short paper is also famous for the introduction of the Julliere model for TMR which continues to be the most often used theory for analyzing the results of TMR experiments. Julliere's work may have been inspired in part by the work of Tedrow and Meservey [6] who had earlier measured the spin-dependence of tunneling currents through an amorphous aluminum oxide tunnel barrier separating various ferromagnetic electrodes from superconducting aluminum. After the discovery of GMR in 1988, tunneling magnetoresistance received much more attention. In 1995 Miyazaki *et al* [7] and Moodera *et al* [8] independently reported TMR in excess of 10% at room temperature.

This was sufficient to make TMR interesting for applications.

Recently, ferromagnetic single-electron transistors (FMSETs) have drawn much attention as magnetoresistive nanoscale devices. Typical FMSETs are consisted of two ferromagnetic tunnel junctions and ferromagnetic quantum dot. In this devices, the interplay of single-electron charging and spin-dependent tunneling effects in FMSETs is currently an attractive topic for both experimental and theoretical studies. The enhanced TMR in the FMSETs has been reported in some experimental studies at low temperature [9-12]. In the theoretical work, the enhancement of the TMR in the ferromagnetic tunnel junctions with a small ferromagnetic metal island has been attributed to contributions from cotunneling processes [13-16]. These reports imply that a new functionality of the FMSETs.

There are eight chapters through this dissertation, and overview of this dissertation is shown in Fig. 1.1. Following this chapter, characteristics of ferromagnetic single-electron transistors are described in Chapter 2. In this chapter, transport properties of the electron in *C*-, *R*- and *RC*-coupled FMSETs are calculated using the Monte Carlo method, which is suitable for the treatment of the stochastic tunneling process. The higher-order tunneling processes are also considered in the calculation.

The Chapter 3 describes development of fabrication techniques for nanoscale devices. In this chapter, novel methods are proposed such as scanning probe microscopy (SPM) local oxidation, stepwise feedback-controlled electromigration (SFCE), and field-emission-induced electromigration (activation), for fabrication of planar-type ferromagnetic tunnel junctions.

In Chapter 4, planar-type Ni-Ni oxide-Ni ferromagnetic tunnel junctions fabricated by SPM local oxidation technique are described. In order to induce magnetic

shape anisotropy, Ni asymmetrical channels were patterned by focused ion beam and photolithography method before formation of Ni oxide wires. Non-linear current-voltage ( $I$ - $V$ ) and magnetoresistive (MR) properties were obtained from planar-type Ni-Ni oxide-Ni ferromagnetic tunnel junctions at 16 K. The results imply that Ni oxide wires formed by SPM local oxidation act as an insulating barrier for the electron.

Chapter 5 and 6 discuss planar-type Ni-Vacuum-Ni ferromagnetic tunnel junctions formed by stepwise feedback-controlled electromigration (SFCE) and field-emission-induced electromigration (activation). These techniques can fabricate the gaps with nanometer scale and control the separation of the gaps. This implies that nanogaps act as vacuum tunnel barriers in planar-type ferromagnetic tunnel junctions. Tunneling transport and MR characteristics are obtained from planar-type Ni-Vacuum-Ni ferromagnetic tunnel junctions at 16 K.

Planar-type single-electron transistors (SETs) fabricated using activation are described in Chapter 7. The devices formed by activation technique exhibited Coulomb blockade phenomena at room temperature. Since the activation technique is based on the motion of the atoms, islands of SETs can be directly formed. Moreover, the charging energy and the number of islands of the SETs are controllable by the magnitude of current during activation procedure.

Finally, concluding remarks of this study are summarized at last part, Chapter 8.

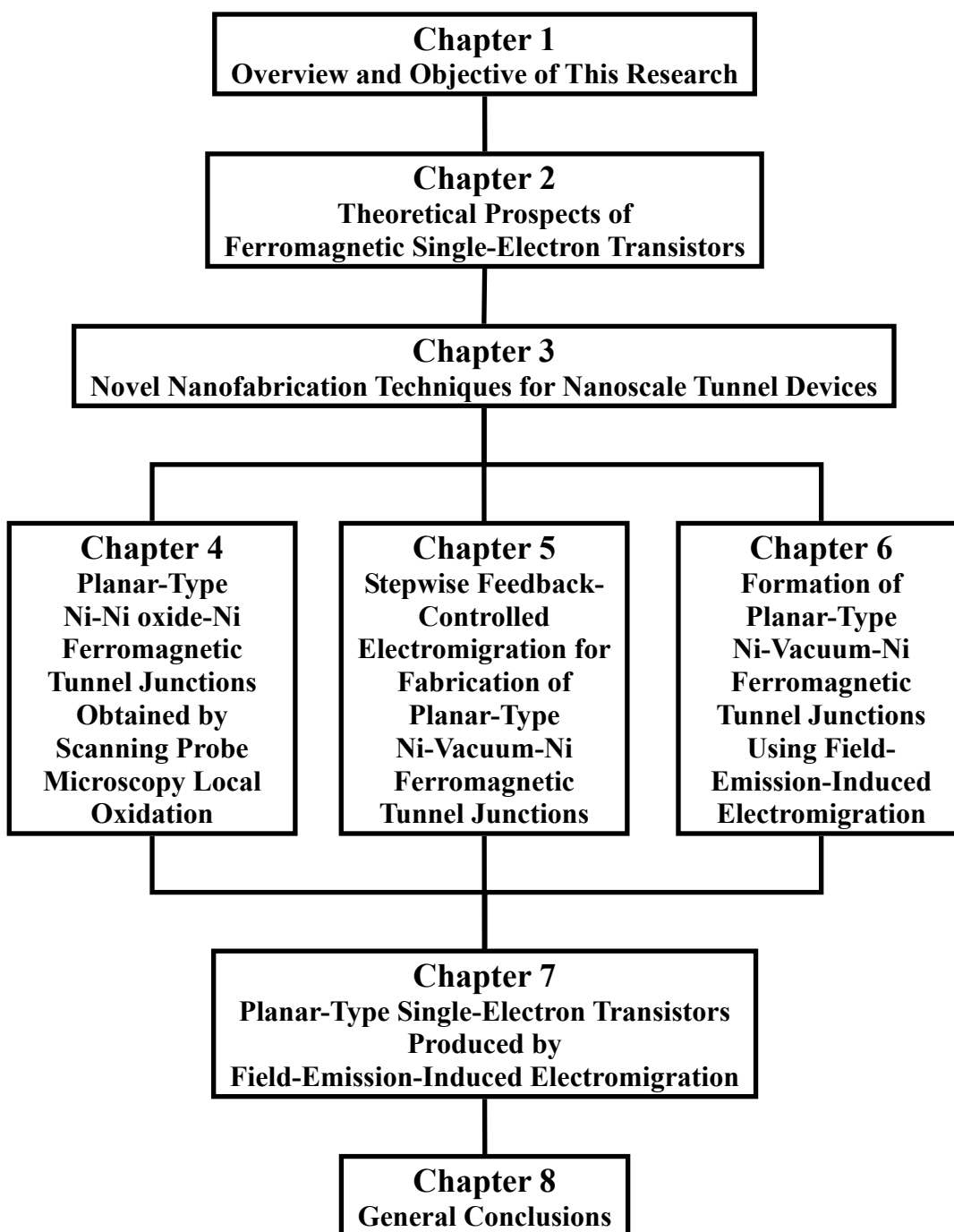


Fig. 1.1. Overview of this research.

# Chapter 2

## Theoretical Prospects of Ferromagnetic Single-Electron Transistors

### 2.1 Introduction

The manipulation of single electron was demonstrated in the seminal experiments by Millikan at the very beginning of the century, but in solid-state circuits it was not implemented until the late 1980's, despite some important earlier background work [1, 2]. The main reason for this delay is that the manipulation requires the reproducible fabrication of very small conducting particles, and their accurate positioning with respect to external electrodes. The necessary nanofabrication techniques have become available during the past two decades and have made possible a new field of solid-state science and technology: single electronics.

Single-electronics, which is based on the discrete charge of the electron, is the ultimate in miniaturization and electro-sensitivity. Capacitively and resistively coupled single-electron transistors (*C*- and *R*-SETs) were first reported by Likarev in 1987 [3]. Since the structure of a *C*-SET is easily realized experimentally, it has been studied in great detail. In *R*-SETs, the gate resistance should be much larger than the quantum resistance to prevent quantum fluctuations in island charge.

Spintronics, which is based on manipulating electron spins [4], delivers high magneto-sensitivity and nonvolatile memory effect. The potential of hybrid single-electronic/spintronic devices and the fundamental importance of spin phenomena at nanoscale have motivated number of studies of spin transport in the Coulomb blockade

regime [5-9].

The potential of hybrid single-electronic/spintronic devices and the fundamental importance of spin phenomena at nanoscale have motivated number of studies of spin transport in the Coulomb blockade regime. Furthermore, Shirakashi and Takemura proposed three types of FMSET which is coupled to the controlling gate potential  $V_g$  by the gate capacitance  $C_g$  ( $C$ -FMSET) [10], the gate resistance  $R_g$  ( $R$ -FMSET) [11], and  $R_g$  and  $C_g$  in series ( $RC$ -FMSETs) [12].

In this chapter, fundamental properties and magnetoresistance properties of FMSETs are described.

## 2.2 Fundamental Characteristics of SET

Consider the simplest system (Fig 2.1) with two electrodes forming the tunnel junction and electrically disconnected from the environment. Let a single electron cross the tunnel barrier. The resulting change  $\Delta V = e/C$  of the junction voltage, where  $C$  is the junction capacitance, is typically very small.

If the tunnel junction area becomes very small or the temperature becomes very low, the condition

$$E_C = \frac{e^2}{2C} \gg k_B T, \quad (2.1)$$

can be fulfilled. For 100 nm scale devices, which were typical for the initial stages of experimental single electronics, charging energy  $E_C$  is of the order of 1 meV, i.e.,  $\sim 10$  K in temperature units. Since thermal fluctuations suppress most single-electron effects unless

$$E_C \geq 10k_B T \quad (2.2)$$

these experiments have to be carried out in the sub-1 K range (typically, using helium dilution refrigerators). In this case the situation can change radically, provided that the tunnel resistance  $R_T$  of the junction is low as well:

$$R_T = \frac{h}{e^2} \approx 26.5 \text{ k}\Omega, \quad (2.3)$$

where  $h$  is Planck constant. The change of the electrostatic energy  $W$  due to the tunneling event is given by

$$\Delta W = \frac{Q^2}{2C} - \frac{(Q \pm e)^2}{2C} = \mp \frac{e}{C} \left( Q \pm \frac{e}{2} \right), \quad (2.4)$$

where  $Q$  is the net electric charge of the junctions of a capacitor. If  $Q$  is located within



the Coulomb blockade range of

$$-\frac{e}{2} < Q < \frac{e}{2}, \quad (2.5)$$

any tunneling event would increase the energy (Fig. 2.2) and is hence impossible at  $T = 0$ . The physical reason of this effect is quite simple: the dominating contribution to the system energy is the electrostatic energy  $Q^2/2C$  of the junction.

Figure 2.3 shows schematic of capacitively coupled SET. SET consists of source, drain, gate, and island electrodes. A DC voltage  $V$  applied between the two parts of the external electrode. The device is reminiscent of a usual MOSFET, but with a small conducting island embedded between two tunnel barriers, instead of the usual inversion channel. In an array of two junctions an electron is transferred via one intermediate state, in which an extra electron or hole charges the central metal electrode between the two junctions. The Coulomb energy of this intermediate state is equal to  $E_1$  or  $E_2$  if the first tunneling event occurs across the left or right junction, respectively:

$$W(n_1, n_2) = \frac{Q_1^2}{2C_1} + \frac{Q_2^2}{2C_2} - Q_e V = \frac{Q^2}{2C_\Sigma} - Q_e V + const., \quad (2.6)$$

where  $C_\Sigma = C_1 + C_2$ ,  $C_1$  is the capacitance of the left junction,  $C_2$  of the right junction,  $Q_1$  is the charge of the left junction, and  $Q_2$  is the charge of the right junction.  $Q_e$  is the charge passed through the DC voltage source, which is given by

$$Q_e = e \left( n_1 \frac{C_2}{C_\Sigma} + n_2 \frac{C_1}{C_\Sigma} \right) + const., \quad (2.7)$$

where  $n_1$  and  $n_2$  is the numbers of electrons passed through the left junction and right junction. The same numbers  $n_{1,2}$  participate in an expression

$$Q = en + Q_0, \quad n \equiv n_1 - n_2, \quad (2.8)$$

for the net charge of the island electrode. Here  $Q_0$  is a sum of the charge injected from

gate electrode.

$$\begin{aligned}
 \Delta W_1^\pm &= W(n_1, n_2) - W(n_1 \pm 1, n_2) \\
 &= \frac{Q^2}{2C_\Sigma} - \frac{(Q \pm e)^2}{2C_\Sigma} \pm \frac{eC_2}{C_\Sigma} V \\
 &= \frac{e}{C_\Sigma} \left\{ -\frac{e}{2} \mp (ne + Q_0) \pm C_2 V \right\}
 \end{aligned} \tag{2.9a}$$

$$\Delta W_2^\pm = \frac{e}{C_\Sigma} \left\{ -\frac{e}{2} \pm (ne + Q_0) \pm C_1 V \right\} \tag{2.9b}$$

Figure 2.4 shows the phase diagram of the double junction SET. The straight lines correspond to the equations  $\Delta W_{1,2}^\pm = 0$  for various of  $n$ . Within each rhombic-shaped region covering the  $Q_0$  axis there exist some value of  $n$ , which provides the equilibrium state of the junction ( $\Delta W_1^\pm < 0, \Delta W_2^\pm < 0$ ).

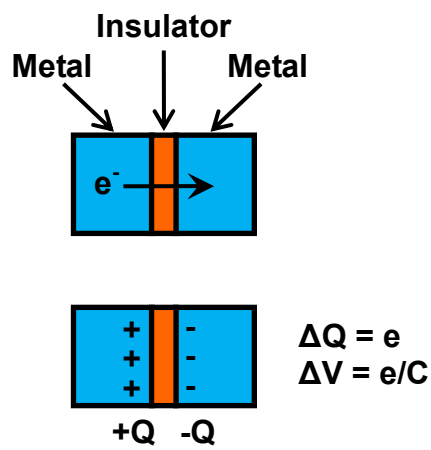


Fig. 2.1. The simplest system exhibiting the Coulomb blockade of tunneling, an isolated tunnel junction with a small capacitance  $C$ , before and after a single-electron tunneling event.

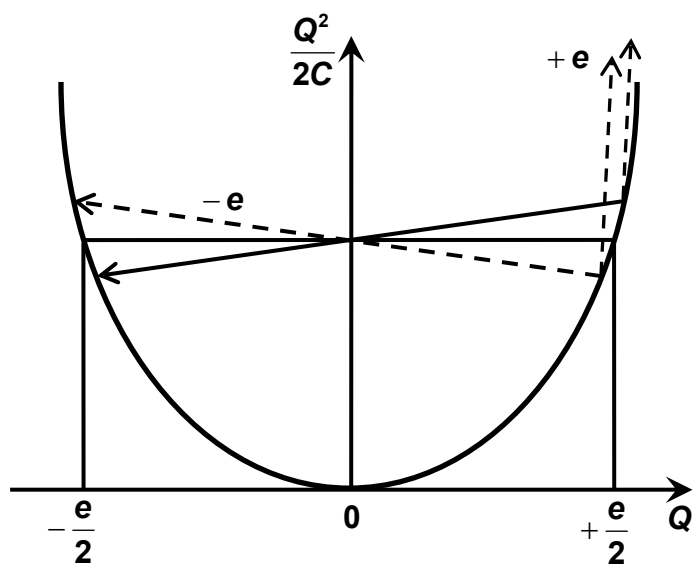


Fig. 2.2. Energy diagram illustrating the physical origin of the Coulomb blockade of tunneling. The dashed lines show energy-disadvantageous tunneling events, while the solid line shows the energy favorable event possible at  $Q > e/2$  and  $Q < -e/2$ .

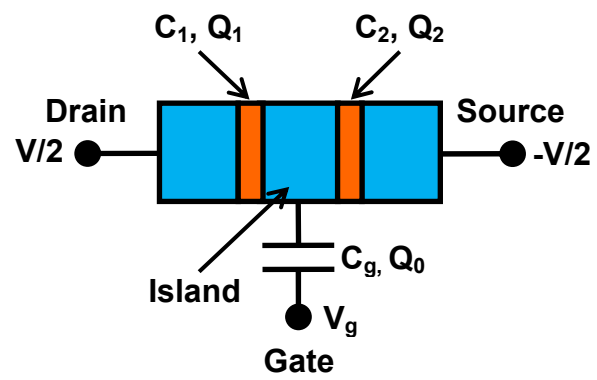


Fig. 2.3. Schematic of capacitively coupled single-electron transistor.

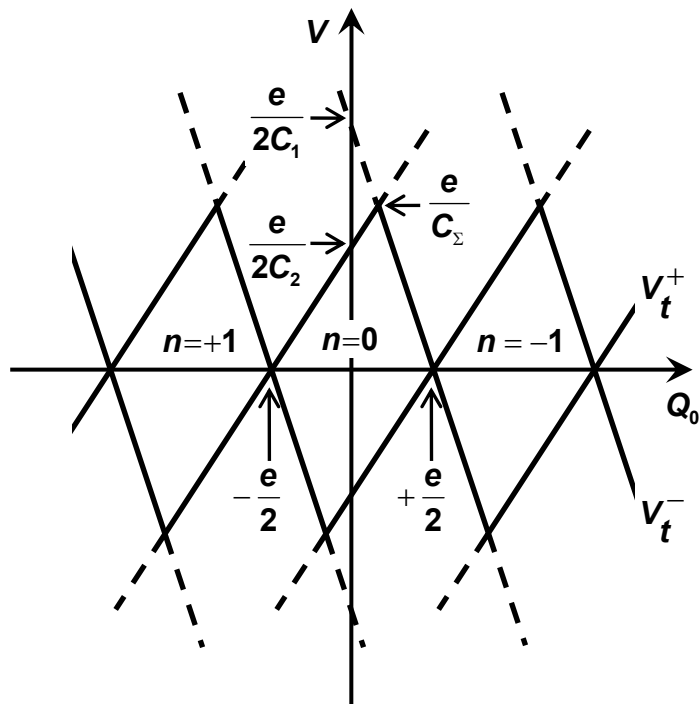


Fig. 2.4. Phase diagram of the double junction with the single-electron tunneling. The central rhombuses correspond to the Coulomb blockade of tunneling for various equilibrium values of  $n$ .

## 2.3 C-coupled FMSET with Multiple Tunnel Junctions

Figure 2.6 shows a ferromagnetic single-electron transistor with multiple tunnel junctions. Source, drain, and island electrodes are ferromagnetic metals. The magnetization of each electrode takes its ferromagnetic alignment for the applied magnetic field (parallel configuration). In zero magnetic field, the electrode magnetization usually shows the antiferromagnetic alignment (antiparallel configuration). The gate electrode is capacitively coupled on each island electrode. The tunnel resistance of each tunnel junction is determined by spin-dependent tunneling, which is  $R_p$  for the ferromagnetic alignment and  $R_{ap}$  for the antiferromagnetic alignment. In other words, the polarization of the source, drain, and islands can be taken into account by the difference between the tunnel resistances  $R_p$  (parallel) and  $R_{ap}$  (antiparallel) in each tunnel junction.

By assuming a Ni-NiO-Ni tunnel junction system with the spin polarization  $P_{\text{Ni}} = 0.23$ , and the tunnel resistance under the ferromagnetic alignment  $R_p = 100 \text{ k}\Omega$ , the tunnel resistance under the antiferromagnetic alignment is given by  $R_{ap} = R_p(1 + P_{\text{Ni}}^2)/(1 - P_{\text{Ni}}^2) = 111 \text{ k}\Omega$ . The capacitance of the tunnel junction  $C_j$  is also assumed to be 1 aF. The number of the junction  $N$  is changed from 2 to 5. For simplicity, all of the tunnel junctions have the same parameters. The gate capacitance  $C_g$  is also assumed to be 0.5 aF. Using these tunnel junction parameters, the charging energy  $E_C$  of a ferromagnetic single-electron transistor with a double tunnel junction ( $N = 2$ ) becomes 26.7 meV, suggesting that the operation temperature  $T$  should be below  $\sim 30 \text{ K}$  for the observation of the single-electron charging effects. All calculations in this study are done using the Monte Carlo method, which is suitable for the treatment of the stochastic tunneling process. The higher-order tunneling processes are also considered in the

calculation.

Figure 2.7 shows drain currents for parallel and antiparallel configurations and tunnel magnetoresistance (TMR) as a function of the drain voltage on a double junction ferromagnetic single-electron transistor. In this result, the temperature and the gate voltage are set at  $T = 1$  K and  $V_g = 0$  V, respectively. From the figure, the Coulomb blockade is seen around the drain voltage of  $\sim 0$  V. The TMR in which the Coulomb blockade is released shows 11 %, which is the same as the value expected from  $P_{Ni} = 0.23$ . However, the TMR is enhanced to 23 % under the Coulomb blockade regime. Drain currents and TMR as a function of the gate voltage are shown in Fig. 2.8. Here the drain currents oscillate with the gate voltage, since the Coulomb blockade periodically repeats ON and OFF by sweeping the gate voltage. The drain current still shows few nA when the Coulomb blockade is ON, which is caused by the inelastic  $q$ -MQT process, i.e., cotunneling. The TMR is enhanced from 11 % to 23 % as the Coulomb blockade state is changed from OFF to ON. Therefore the TMR also has the oscillation characteristics on the gate voltage.

Figure 2.9 shows the TMR as a function of the gate voltage for different drain voltages on the double junction ferromagnetic single-electron transistor. From this, the TMR in each drain voltage is well-modulated by the gate voltage. In addition, the gate voltage width showing the enhanced TMR is decreased with increasing the drain voltage. This is due to the fact that the drain current under the OFF state of the Coulomb blockade becomes broad with increasing the drain voltage. It should be noted that by using a ferromagnetic single-electron transistor structure, the TMR could be modulated by the gate voltage, and, the phase of the modulated TMR could also be controlled by the drain voltage.



Figure 2.10 shows the TMR as a function of the gate voltage for different numbers of the junctions. Although the TMR is 11 % when the Coulomb blockade is OFF, the TMR is clearly enhanced under the Coulomb blockade On and is further increased with increasing the number of the junctions  $N$ ; 23 % ( $N = 2$ ), 37 % ( $N = 3$ ), 52 % ( $N = 4$ ), and 70 % ( $N = 5$ ). This means that in addition to the tuneability of the TMR on the gate and drain voltages, the enhancement of the TMR may be adjusted by varying the number of the junctions.

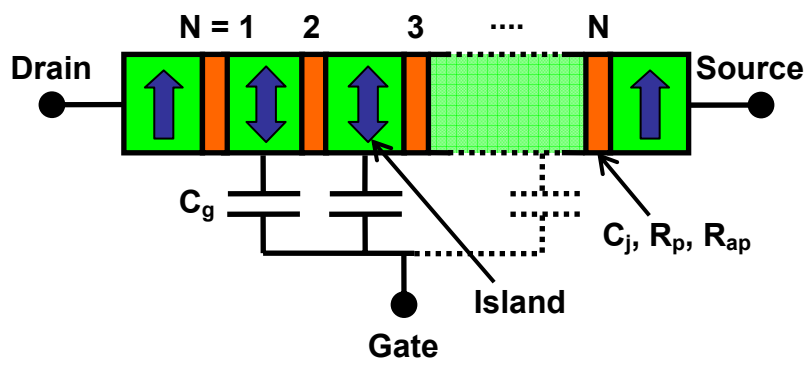


Fig. 2.6. Schematic of a ferromagnetic single-electron transistor with multiple tunnel junctions.

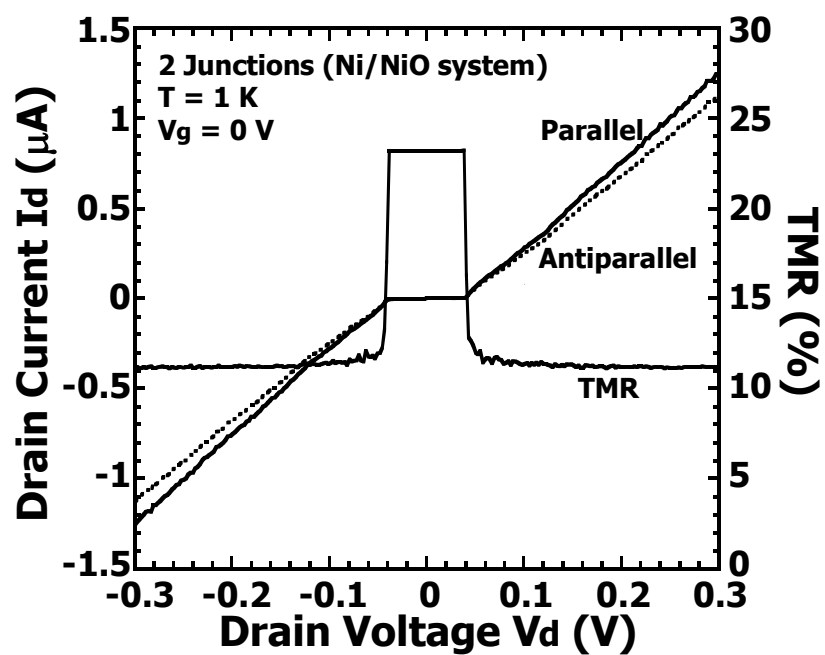


Fig. 2.7. Drain currents and TMR as a function of drain voltage on a double junction ferromagnetic single-electron transistor.

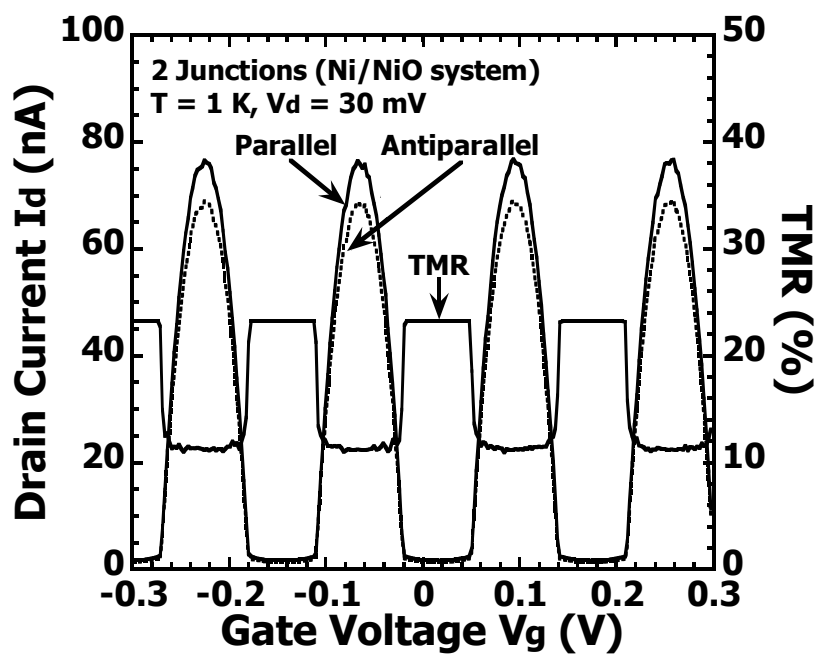


Fig. 2.8. Drain currents and TMR as a function of gate voltage on a double junction ferromagnetic single-electron transistor.

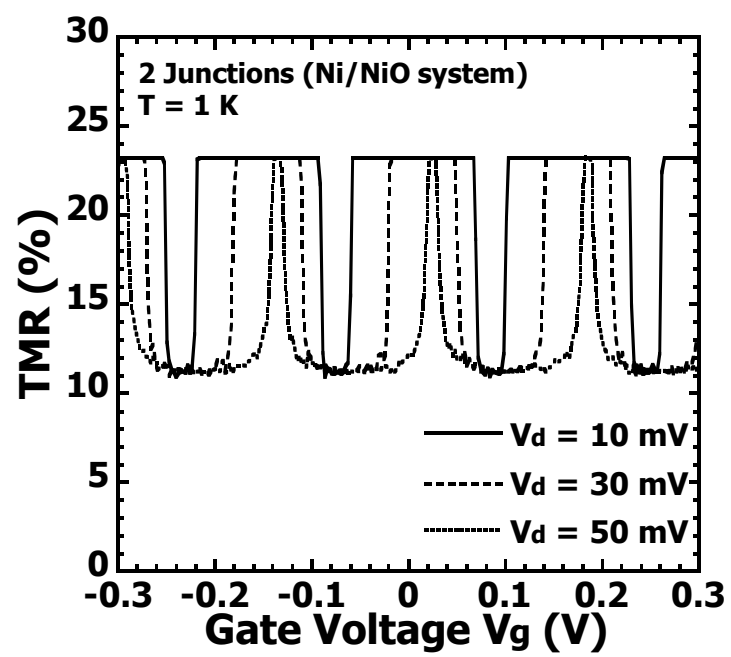


Fig. 2.9. TMR as a function of gate voltage for different drain voltages.

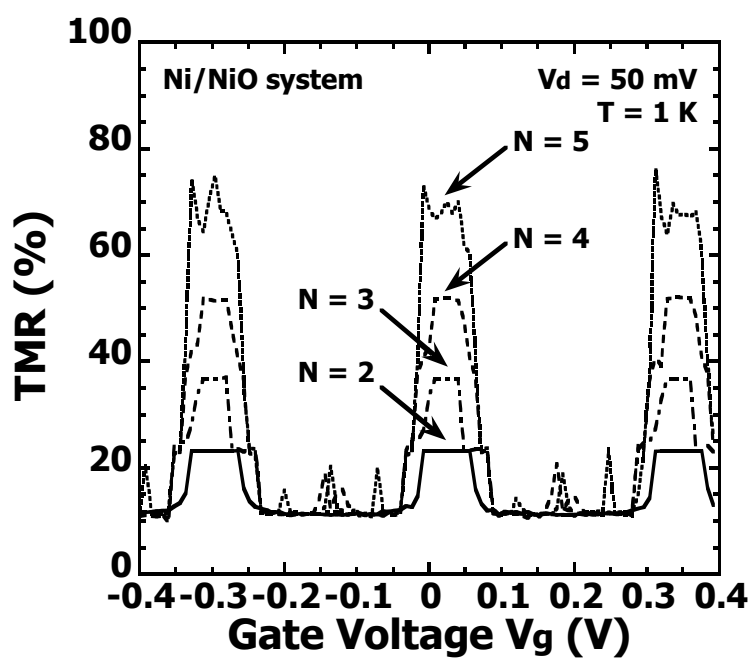


Fig. 2.10. TMR as a function of gate voltage for different numbers of tunnel junctions.

## 2.4 $R$ -coupled FMSET

Figure 2.11 shows a resistively coupled ferromagnetic single-electron transistor with double tunnel junction. The source, drain and island electrodes are ferromagnetic metals. We assume that electrode magnetization usually shows antiferromagnetic alignment in zero magnetic field (antiparallel configuration) and takes ferromagnetic alignment with the application of a magnetic field (parallel configuration). The gate electrode is resistively coupled to the island electrode. The tunnel resistance of each ferromagnetic tunnel junction is determined by spin-dependent tunneling, which is  $R_p$  (parallel) for ferromagnetic alignment and  $R_{ap}$  (antiparallel) for antiferromagnetic alignment. In other words, polarization of the source, drain and island can be taken into account by the difference between tunnel resistances  $R_p$  and  $R_{ap}$  in each ferromagnetic tunnel junction.

We consider a Ni-NiO-Ni ferromagnetic tunnel junction system with spin polarization  $P_{\text{Ni}} = 0.23$ , suggesting  $\text{TMR} = 11\%$  in the sequential tunneling regime. Since the tunnel resistance under ferromagnetic alignment is assumed to be  $R_p = 100\text{ k}\Omega$ , the tunnel resistance in the antiparallel configuration is given by  $R_{ap} = R_p(1 + P_{\text{Ni}}^2)/(1 - P_{\text{Ni}}^2) = 111\text{ k}\Omega$ . The capacitance of the junction is also assumed to be  $C = 1\text{ aF}$ . For simplicity, all ferromagnetic tunnel junctions are made the same. The gate resistance  $R_g$  must be greater than the quantum resistance  $R_Q = h/e^2$  and is set to  $1\text{ M}\Omega (= 10R_p)$ . The charging energy of the  $R$ -FMSET becomes  $E_C = 40\text{ meV}$  from these tunnel junction parameters, suggesting that the operating temperature should be below  $T = \sim 100\text{ K}$  for observation of single-electron charging effects. Within the framework of the semiclassical model [13], the Monte Carlo procedure is used for calculations. In addition to the rate of single-electron tunneling, the rate of second order inelastic  $q$ -

MQT is naturally considered in the calculation. Moreover, Nyquist noise from the gate resistance at operating temperature  $T$  is also taken into consideration.

Drain currents for parallel and antiparallel configurations and TMR as a function of the drain voltage on an  $R$ -FMSET are shown in Fig. 2.12 where the temperature and the gate voltage are set at  $T = 1$  K and  $V_g = 0$  V, respectively. From Fig. 2.12, a Coulomb blockade region corresponding to charging energy of  $\sim 40$  meV is seen around drain voltage of  $\sim 0$  V. Although the TMR shows  $\sim 11$  % when the Coulomb blockade is released, as expected, the TMR increased to  $\sim 23$  % in the Coulomb blockade regime. This can be explained by the difference in the rate of single-electron tunneling and inelastic  $q$ -MQT (cotunneling).

Figure 2.13 illustrates the drain currents and the TMR as a function of the gate voltage. The temperature and the drain voltage are set at  $T = 1$  K and  $V_d = 30$  mV, respectively. One can see that, in contrast to the  $C$ -FMSET, the drain currents are not periodic to the gate voltage because the  $R$ -FMSET structure is not influenced by the background charges described above. Within the Coulomb blockade range, enhancement of the TMR up to  $\sim 23$  % can be seen too. Outside the blockade range the drain current  $I_d$  and the source current  $I_s$  may be different because of the finite gate current  $I_g$ . Therefore, the TMR depends complicatedly on the gate voltage.

The relationship between the TMR and the gate voltage is shown in Fig. 2.14. The curves are shifted vertically 10 % for clarity. The TMR outside the blockade is  $\sim 0$  % and is not uniformly defined. In contrast, the TMR is enhanced and defined to  $\sim 23$  % inside the Coulomb blockade. It should be noted that, by using a resistively coupled ferromagnetic single-electron transistor structure, the TMR can be modulated and controlled by the drain and gate voltages.



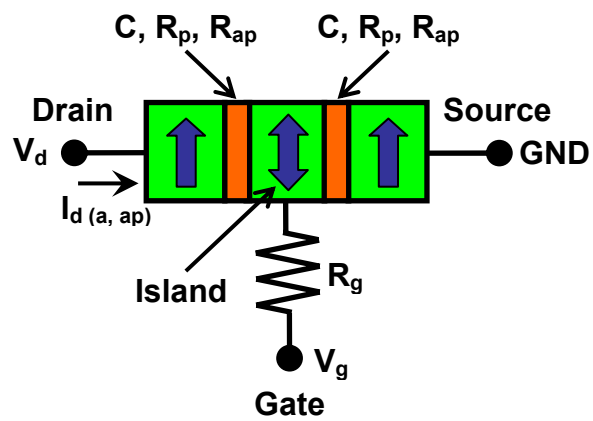


Fig. 2.11. Schematic of a resistively coupled ferromagnetic single-electron transistor.

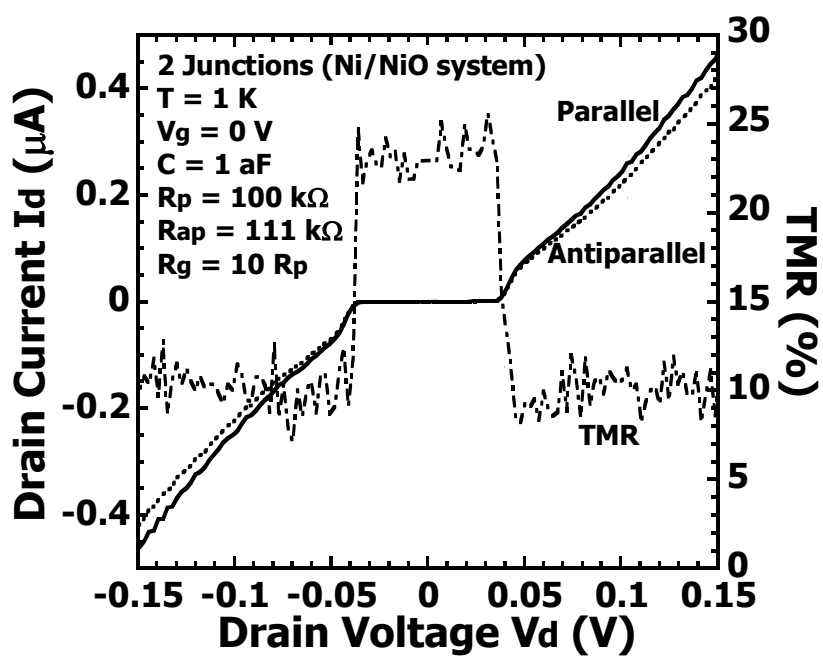


Fig. 2.12. Drain currents and TMR ratio as a function of the drain voltage on a resistively coupled ferromagnetic single-electron transistor.

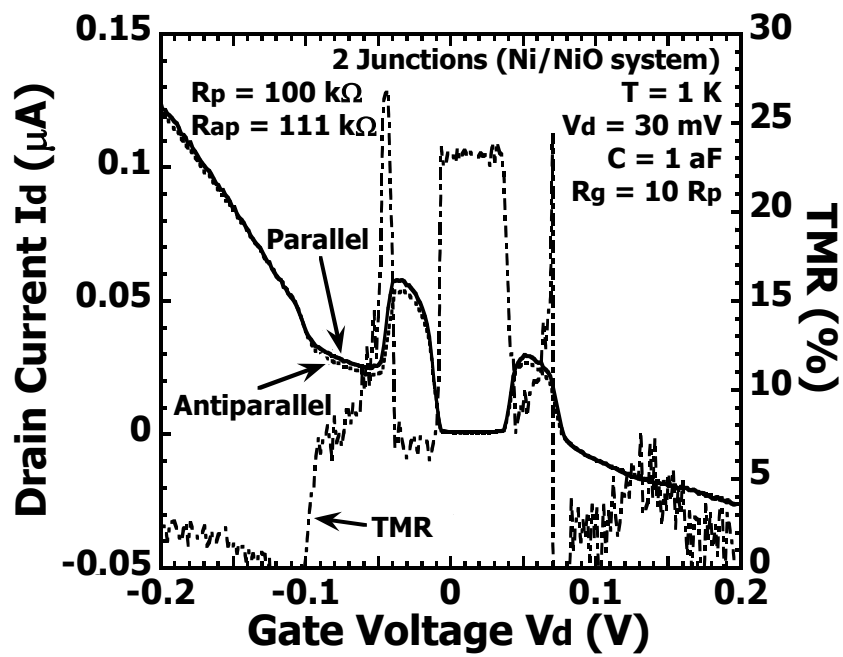


Fig. 2.13. Drain currents and TMR ratio as a function of the gate voltage on a resistively coupled ferromagnetic single-electron transistor.

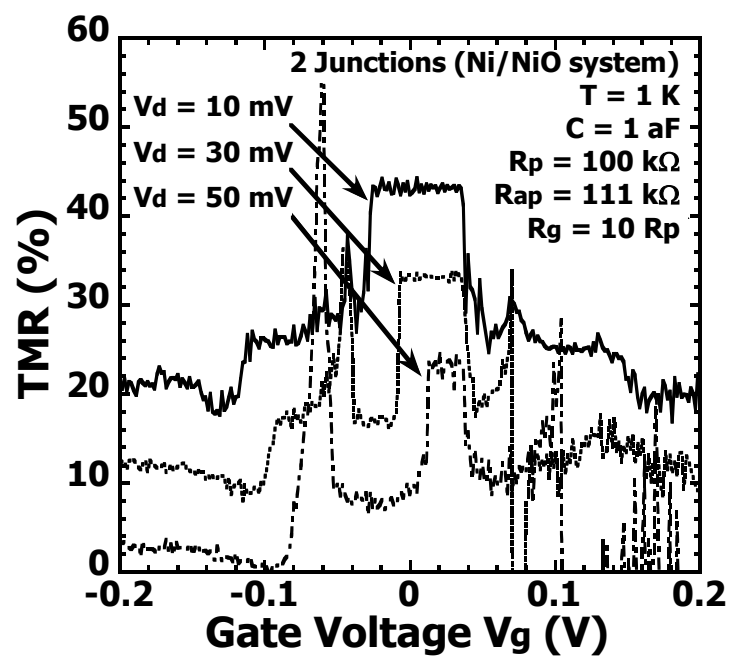


Fig. 2.14. TMR ratios as a function of the gate voltage at different drain voltages. The curves are shifted 10 % for clarity.

## 2.5 *RC*-coupled FMSET

An *RC*-coupled ferromagnetic single-electron transistor with double tunnel junction is shown in Fig. 2.15. The gate electrode consists of an *RC* circuit and it connects an island electrode with the controlling gate potential. The source, drain, and island electrodes are ferromagnetic metals. We assume that the magnetization in the electrodes usually shows antiferromagnetic alignment in a zero magnetic field (antiparallel configuration) and takes ferromagnetic alignment upon application of the magnetic field (parallel configuration). The polarization of the source, drain, and island electrodes can be taken into account by determining the difference between the tunnel resistance  $R_p$  (parallel) and  $R_{ap}$  (antiparallel) in each ferromagnetic tunnel junction. In other words, the tunnel resistance of each ferromagnetic tunnel junction is determined by spin-dependent tunneling, which is  $R_p$  for ferromagnetic alignment and  $R_{ap}$  for antiferromagnetic alignment, and is treated as junction resistance.

As mentioned above, the *RC*-FMSET has an  $R_g C_g$  coupling circuit between the island and the gate potential. Hence, the relaxation time of the coupling circuit affects the background charge of the double junction system due to variation of the charge at the coupling capacitance  $C_g$ . As a result, the charge state of spin accumulation in the island may be influenced and released by finite current that goes through the coupling circuit. In addition, the spin-flip relaxation time, which is crucial for the observation of spin accumulation, strongly depends on the quality of the material of the island [14-17]. Therefore, we assume that the spin in the island is equilibrated [18-20].

We consider a ferromagnetic tunnel junction system with  $\text{TMR} = 20\%$  under the sequential tunneling regime, which corresponds to spin polarization  $P = 0.3$ . So, if the tunnel resistance under ferromagnetic alignment is assumed to be  $R1_p = 100\text{ k}\Omega$  and  $R2_p$

$= 5 \times R1_p = 500 \text{ k}\Omega$ , the tunnel resistance under the antiparallel configuration is given by  $R1_{ap} = 1.2 \times R1_p = 120 \text{ k}\Omega$  and  $R2_{ap} = 1.2 \times R2_p = 600 \text{ k}\Omega$ . The capacitance of each ferromagnetic tunnel junction is also assumed to be  $C1 = C2 = 1 \text{ aF}$ . The gate resistance  $R_g$  should be greater than the quantum resistance  $R_Q = h/e^2$  and is set to  $10 \text{ M}\Omega$  ( $R_g \gg R1_{(p, ap)}, R2_{(p, ap)}$ ). The gate capacitance  $C_g$  is also given by  $C_g/(C1 + C2) = 3$ . These parameters lead to the fact that the energy scale of the quantum fluctuations of the  $R_g C_g$  coupling circuit  $\hbar / (R_g C_t)$  [where  $C_t = C_g(C1 + C2)/(C1 + C2 + C_g)$ ] is less than  $e^2/(C1 + C2)$ . This implies that for typical current  $I_{d(p, ap)} \sim e / [(R1_{(p, ap)} + R2_{(p, ap)})(C1 + C2)]$  the relaxation time of the  $R_g C_g$  coupling circuit is greater than the typical time interval of the tunneling events  $e / I_{d(p, ap)}$ . The dynamics of the  $RC$ -FMSET can be calculated within the framework of the semiclassical model [13]. In the calculation, a Monte Carlo procedure is used, and the rate of second order inelastic  $q$ -MQT (cotunneling) is also considered in addition to the rate of usual single-electron tunneling.

Figure 2.16 shows drain currents for parallel and antiparallel configurations as a function of the drain voltage of the  $RC$ -FMSET. Here, the temperature and the gate voltage are set at  $T = 1 \text{ K}$  and  $V_g = 0 \text{ V}$ , respectively. Due to the large difference between  $R1_{(a, ap)}$  and  $R2_{(a, ap)}$ , one can see Coulomb staircases. Furthermore, the drain currents clearly show the hysteresis as a function of the drain voltage. The relationship between the TMR and the drain voltage at  $V_g = 0 \text{ V}$  is illustrated in Fig. 2.16. Although the TMR shows 20 % when the Coulomb blockade is released as expected, the TMR increases up to 44 % in the Coulomb blockade regime. This is due to the difference in the rate of the single-electron tunneling and the inelastic  $q$ -MQT. Moreover, hysteresis of the TMR also occurs, which is due to hysteresis of the Coulomb blockade. This is a unique feature of the  $RC$ -FMSET and is in contrast to that in usual  $C$ - and  $R$ -FMSETs. From

the semiclassical model of the  $RC$ -FMSET, the charge injection from the  $R_g C_g$  coupling circuit to the island electrode is determined by the potential  $V_{RC} = V_g - V_d C1 / (C1 + C2)$ . Therefore, for a charge state with definite number  $n$  of excess electrons in the island electrode, charge  $Q_n$  on the equilibrium in the  $R_g C_g$  coupling circuit is expressed as  $Q_n = (ne + Q_0 + C_g V_{RC})(C1 + C2)/(C1 + C2 + C_g)$ , where  $Q_0$  is the background charge of the island electrode. Since the condition of the blockade for the definite charge state  $n$  is given by  $|Q_n| < e/2$ , the charge  $Q_n$  shows several metastable charge states that satisfy the condition  $|Q_n| < e/2$ . The charge  $Q_n$  of the  $RC$ -FMSET implies that the addition of the electron to the island electrode causes an increase of the effective charge  $Q_n$  by only  $e (C1 + C2)/(C1 + C2 + C_g)$ , leading to the fact that several stable states are possible within the blockade. This is the origin of the hysteresis on the drain currents and the TMR. In this system, the stability threshold voltage for a certain charge state  $n$  is given by  $V_{th}(n) = \min[(e/2 - Q_n)C1, (e/2 + Q_n)C2]$  [ $V_{th}(n) > 0$ ] and can be varied by changing the gate potential. The maximum value becomes  $V_{th, \max} = e / (C1 + C2)$  from the condition  $(e/2 - Q_n)C1 = (e/2 + Q_n)C2$ . Its minimum value corresponds to the condition  $V_{th}(n) = V_{th}(n + 1)$  which gives  $V_{th, \min} = eC_g / [(C1 + C2)(C1 + C2 + C_g)]$ . Hence, in the  $RC$ -FMSET one cannot suppress the threshold voltage to zero by varying the gate potential.

Drain currents for parallel and antiparallel configurations as a function of the gate voltage are shown in Fig. 2.17. The temperature and the drain voltage are set at  $T = 1$  K and  $V_d = 50$  mV, respectively. The charge state of the device moves to a neighboring stable state when the gate voltage is increased. Thus the drain currents for a fixed drain voltage show a periodic function of the gate voltage with a period of  $e/C_g$ , which is similar to that of the  $C$ -FMSET. Then, as the gate voltage is decreased, the drain

currents hardly show any current flow, which is due to the fact that the device is in the Coulomb blockade state. The behavior of the drain currents, depending on the direction of sweep of the gate voltage, causes hysteresis of the TMR as illustrated in Fig. 2.17. The TMR is increased up to 44 % within the range of Coulomb blockade and is modulated between 20 % and 44 % depending on the behavior of the drain currents.

Figure 2.18 shows the drain currents for parallel and antiparallel configurations at  $T = 1$  K and  $V_d = 50, 70,$  and  $90$  mV as a function of the gate voltage. The curves are shifted vertically 30 nA for clarity. As expected, the drain currents at the fixed gate voltage increase with an increase in the drain voltage. Since the maximum threshold voltage of the Coulomb blockade becomes  $V_{th, max} = e / (C1 + C2) = 80$  mV in this device, the hysteresis of the drain currents becomes clear when the drain voltage is greater than  $V_{th, max}$ . The potential of the island electrode  $V_{island}$  is defined as  $V_{island} = (Q_n + V_d C1) / (C1 + C2)$ , therefore  $V_{island}$  exhibits hysteresis due to several charge states by the variation of the gate voltage, resulting in hysteresis of the drain current on the gate voltage.



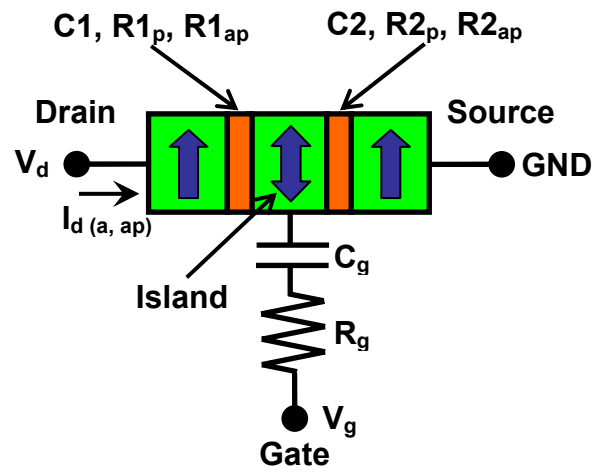


Fig. 2.15. Schematic of an RC-coupled ferromagnetic single-electron transistor.

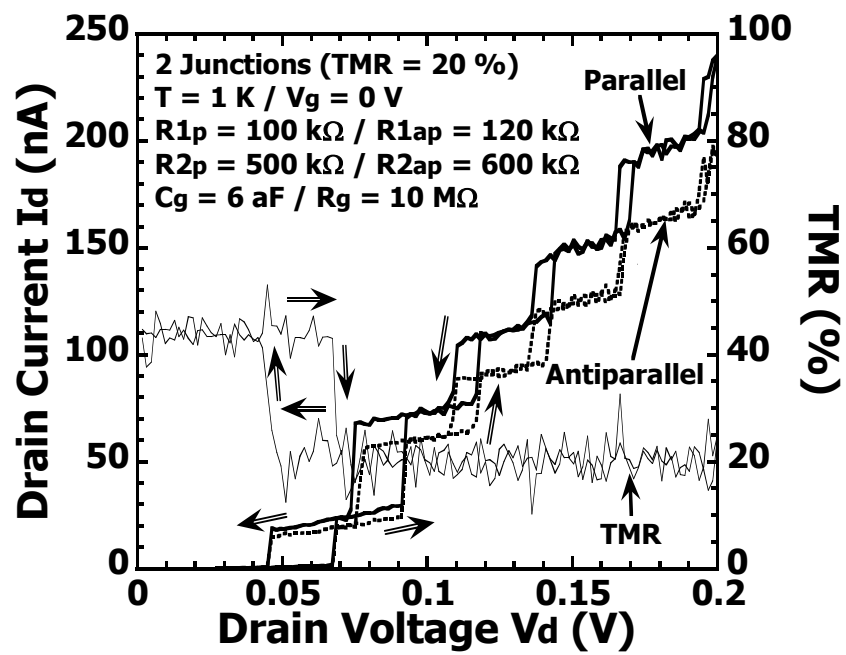


Fig. 2.16. Drain currents and TMR ratio as a function of the drain voltage on an  $RC$ -coupled ferromagnetic single-electron transistor.

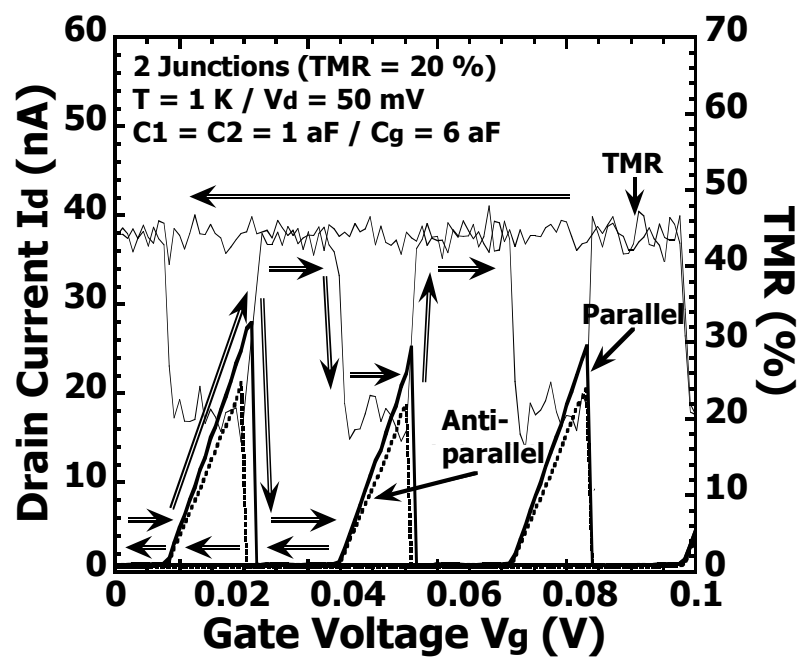


Fig. 2.17. Drain currents and TMR ratio as a function of the gate voltage on an *RC*-coupled ferromagnetic single-electron transistor.

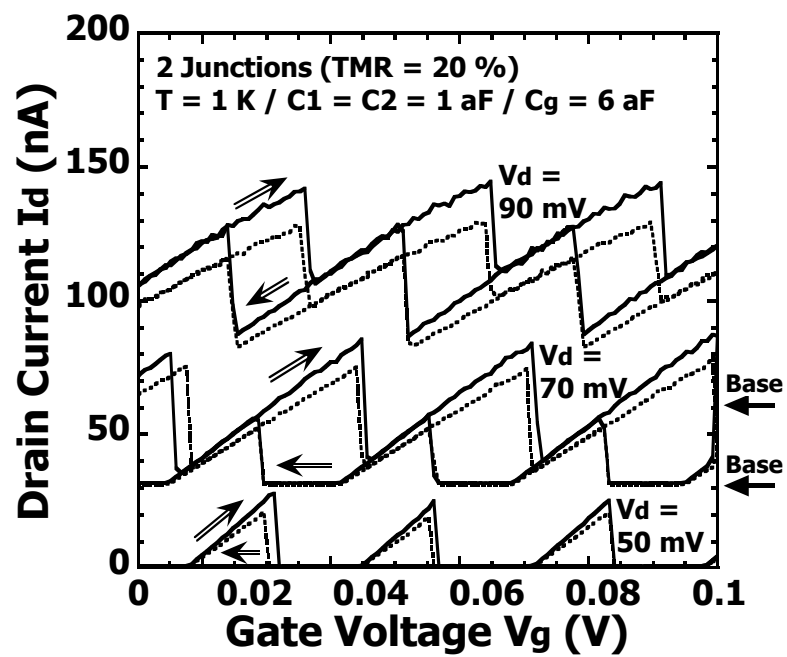


Fig. 2.18. Drain currents as a function of the gate voltage in different drain voltages. The curves of the drain currents are shifted 30 nA for clarity.

## 2.6 Summary

In conclusion, several single-electron transistors have been studied. In *C*-FMSET with multiple tunnel junctions, the inelastic *q*-MQT process under the Coulomb blockade regime leads to a considerable enhancement of TMR which has a specific dependence on the gate and drain voltages and on the number of the tunnel junctions. On the other hand, TMR of *R*-FMSET was also controlled by gate and drain voltages. Furthermore, we have proposed and studied ferromagnetic single-electron transistors controlled with an *RC* gate. Several metastable charge states within the range of Coulomb blockade cause clear hysteresis of the TMR. These features have a specific dependence on the gate and drain voltages. These results imply new functionality of the FMSET.

# Chapter 3

## Novel Nanofabrication Techniques for Nanoscale Tunnel Devices

### 3.1 Introduction

For the fabrication of the planar-type ferromagnetic tunnel devices, nanolithography techniques are required because of the nanometer-scale dimensions of the devices. Several techniques have been demonstrated to be able to produce nanoscale tunnel devices, which involve either highly elaborate electron-beam (EB) lithography or other special techniques and processes, such as shadow evaporation [1, 2], mechanical break junctions [3], metal deposition over suspended structures [4], electrochemical deposition [5, 6], and electromigration (EM)-induced breaking of thin metal wires [7]. However, these techniques involve a series of complicated processes that are not easy to control, generate and have low yields.

In order to simplify the fabrication process further, we have investigated simple and easy techniques. Therefore, we have reported the local oxidation nanolithography of ferromagnetic thin films using scanning probe microscopes [8] (SPMs) and fabrication of ultra small ferromagnetic tunnel junctions using SPM local oxidation technique [8-10]. On the other hand, we have also studied the novel EM techniques [11-14] and fabrication of ferromagnetic nanoscale devices with vacuum tunnel barriers using EM method [15-16].

### 3.2 Scanning Probe Microscopy Local Oxidation

Scanning probe Microscopy (SPM) can achieve atomic resolution on semiconductor and metallic surfaces. In particular, local oxidation nanolithography by SPM is a reliable method of producing ultra small patterns on material surfaces [17]. Figure 3.1 shows the schematic of SPM local oxidation. The reaction mechanism of the SPM local oxidation is considered to be anodic oxidation, and this oxidation process proceeds through an electrochemical reaction driven by a negative bias voltage applied to the SPM tip. The key factors for controlling the feature size of the oxide are the generation of space charges within the oxide [18], the formation of a water meniscus [19], the modulation of applied bias voltage [20]. In contact-mode SPM local oxidation, it has been reported that voltage modulation sweeps out space charges at the Si/SiO<sub>2</sub> interface during the reverse-bias cycle, allowing these charged ions to diffuse into the bulk, which cannot occur under a static electric field [18].

Table 3.1 shows SPM images of Ni oxide wires using contact mode SPM local oxidation at different voltage modes, voltages and scanning speeds. The applied bias voltage and scanning speed were varied from 15 to 25 V and from 5 to 15 nm/s, respectively. All SPM images in this study were of areas of  $1 \times 1 \mu\text{m}^2$ . A visual inspection reveals that the Ni oxide wires of the AC voltage mode oxidation are smaller than those of DC voltage mode oxidation. Furthermore, the size fluctuation of the Ni oxide wires is further suppressed in AC voltage mode experiments.

Figure 3.2 shows (a) average full width at half maximum (FWHM) and (b) height of Ni oxide wires as a function of the bias voltage. FWHM and height were calculated from cross-sectional profiles of Ni oxide wires. With increasing the applied bias voltage between the tip and sample surface, the FWHM and height of Ni oxide wires was

increased. This dependence may be due to the threshold electric field promoting the oxidation process and the curvature radius of SPM tip [21].

In Fig. 3.3(a), the standard deviations (STDs) of FWHM of the Ni oxide wires are plotted as a function of bias voltage. Moreover, the STDs of the height is shown in Fig. 3.3(b). All STDs of FWHM in AC voltage mode oxidation are around 10 nm, which are not dependence on scanning speed. Furthermore, STDs of height in AC voltage mode oxidation are below 2 nm, which are smaller than those obtained by DC voltage mode. Under the SPM local oxidation with static DC bias voltage, the oxide grows by the formation of oxyanions from water electrolysis in the meniscus. These ions migrate through the oxide by the electric field at the tip-sample junction. However, spatial variation of the ionic concentration may cause a rapid buildup of space charge within the oxide. Space charge effect reduces the growth rate of the oxide and interrupts the oxide growth. On the other hand, the space charge within the oxide may be neutralized and released by applying the AC voltage [18, 20].

Figure 3.4(a) shows the atomic force microscope (AFM) image of the fabricated Ni oxide wire. In order to evaluate the conductivity of the Ni oxide wire, the current mapping image was measured using the AFM under the constant voltage mode. The results imply that the insulating property of the wire due to oxidation was confirmed as indicated in Fig. 3.4(b).



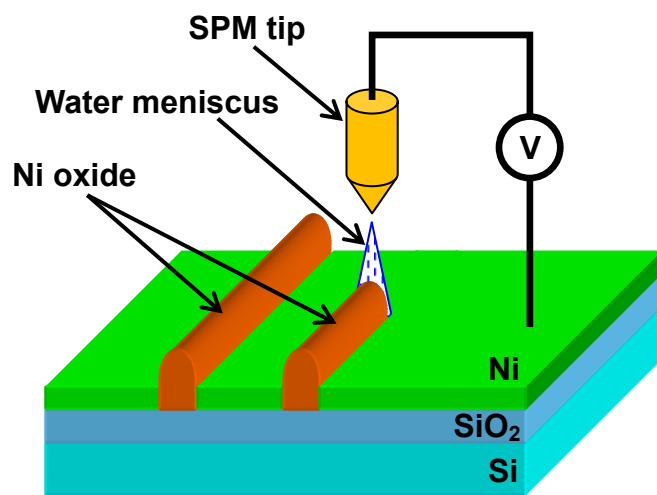
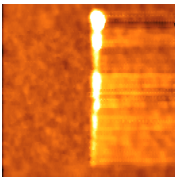
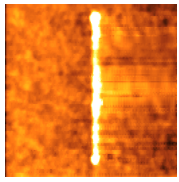
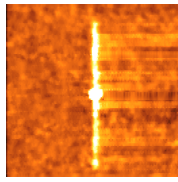
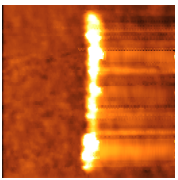
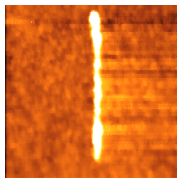
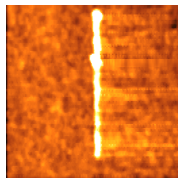
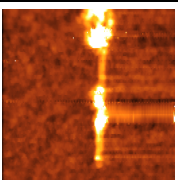
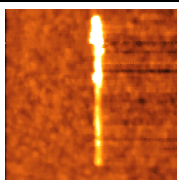
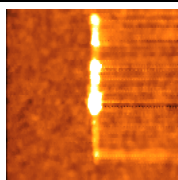
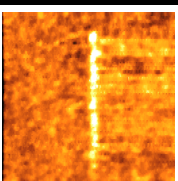
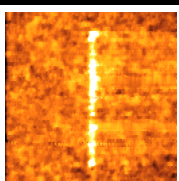
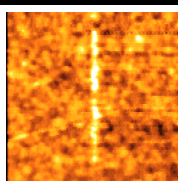
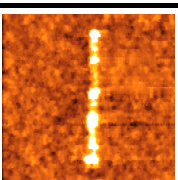
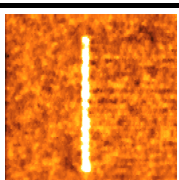
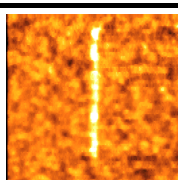
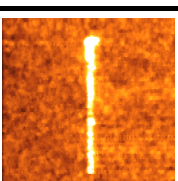
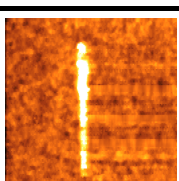
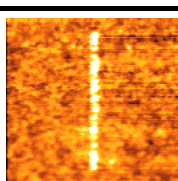


Fig. 3.1. Schematic of SPM local oxidation.

Table 3.1. AFM image of Ni oxide wire formed by contact mode SPM local oxidations under DC and AC bias voltage.

		Scanning Speed (nm/s) (Size: 1×1 μm <sup>2</sup> )		
		5	10	15
DC Voltage V (V)	15			
	20			
	25			
AC Voltage V (V)	15			
	20			
	25			

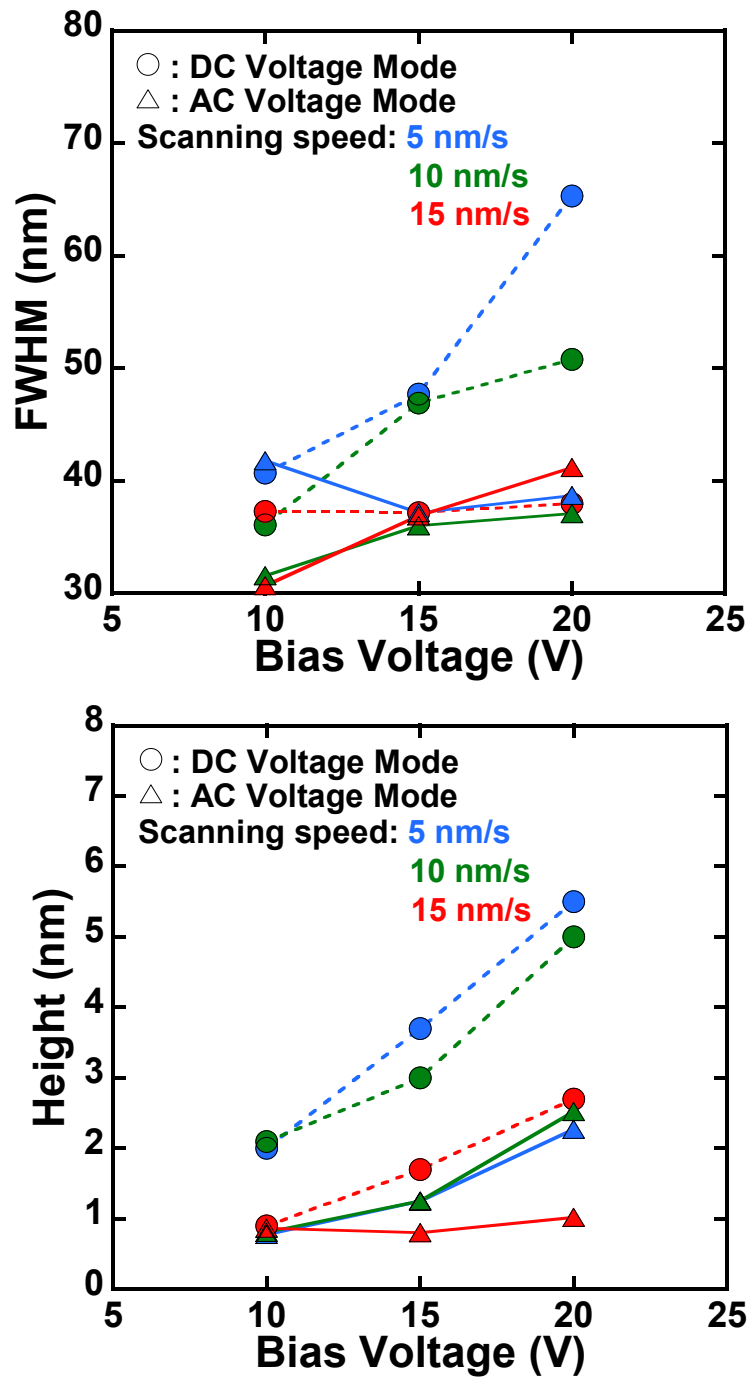


Fig. 3.2. Dependence of (a) FWHM and (b) height of Ni oxide wires fabricated by SPM local oxidation on the bias voltage of SPM tip.

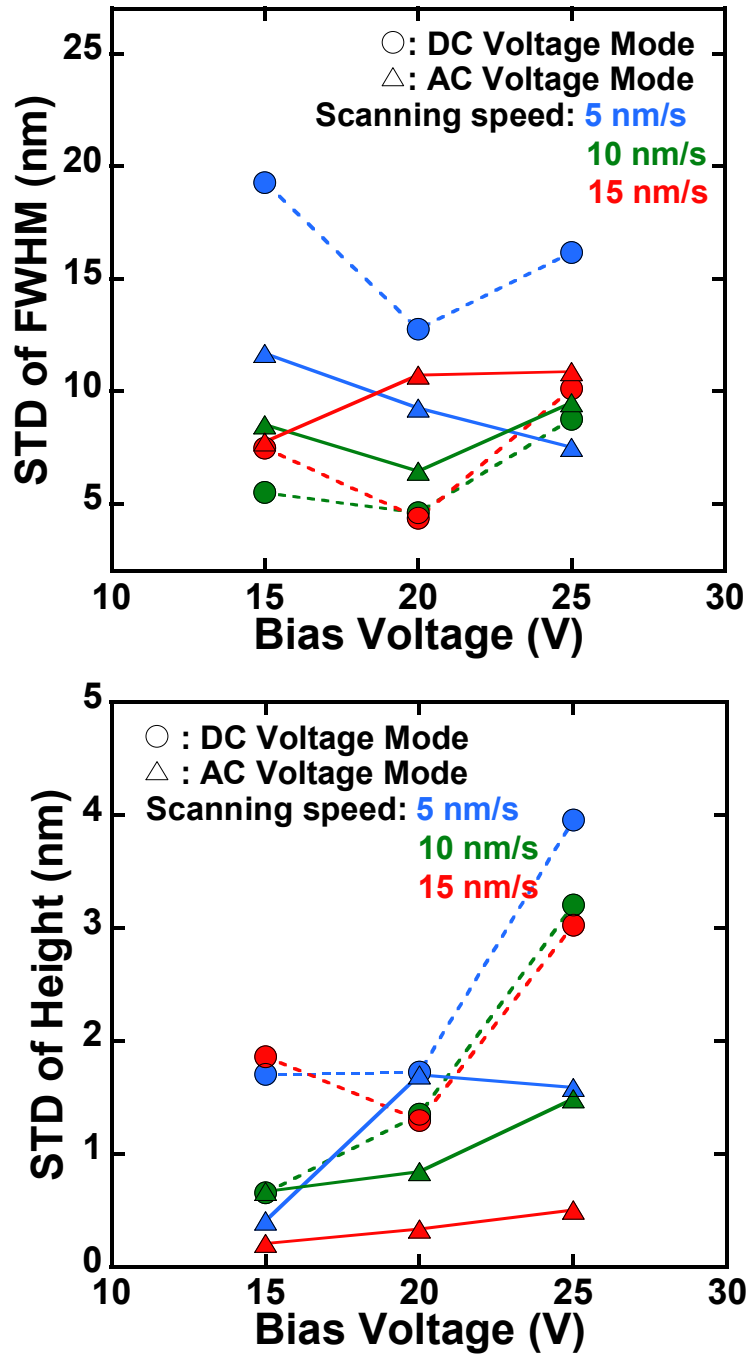


Fig. 3.3. Dependence of standard deviations of (a) FWHM and (b) height of Ni oxide wires on bias voltage of the SPM tip.

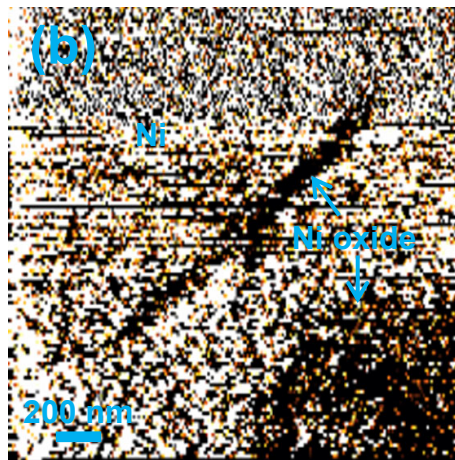
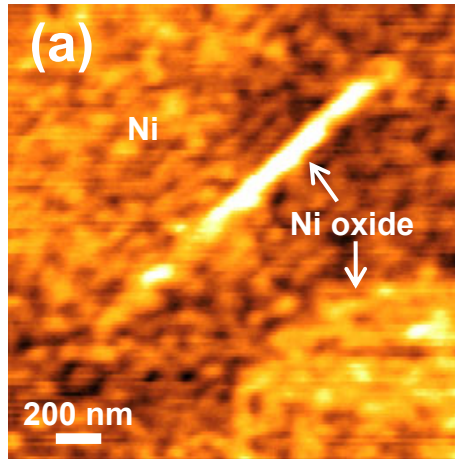


Fig. 3.4. (a) AFM image and (b) current image of Ni oxide wire formed by contact mode SPM local oxidations.

### 3.3 Stepwise Feedback-Controlled Electromigration

Breaking thin metal nanowires induced by electromigration of metal atoms has proven to be a useful technique for making nanoscale gaps between metal electrodes [7]. This method is particularly simple as compared with other methods because it is achieved by only passing a current through a metal nanowire. In typical electromigration experiments for nanogap formation, a bias voltage through a metal nanowire is ramped up to the point in which it breaks due to the electromigration. This approach is particularly simple because it is achieved by only passing a current through a metal nanowire, the typical procedure induces an abrupt break that yields a nanogap with uncontrollable high tunnel resistance [7, 22-24]. It is considered that the fabrication of highly reproducible nanogaps using a single voltage ramp is difficult because the current temperature (Joule heating) during the formation of nanogap junctions are both changing rapidly [7]. Hence, several approaches have work on feedback-controlled electromigration (FCE) mechanisms, based on resistance monitoring of nanowires, in order to control rapid electromigration and fabricate smaller nanogaps. The FCE process can be used to fabricate devices with resistance ranging from a metallic regime through a few-atom regime characterized by quantum of conductance plateaus into a tunneling regime once the gap is formed. The FCE mechanisms have been used to control electromigration and fabricate smaller nanogaps [25-29]. It is considered that the thermal instability due to a large current passing through a metal nanowire seriously degrades the reproducibility of the procedure and often results in catastrophic break with nanogaps greater than 10 nm. In order to avoid such thermal effects, we investigated a stepwise approach, based on FCE scheme, for the control of the channel resistance of metal nanowires and called this procedure

“stepwise feedback-controlled electromigration (SFCE)”.

Figure 3.5 shows the flowchart of SFCE method. First, we performed the FCE scheme which dynamically adjusts the applied voltage to the Ni nanoconstriction in response to the changing resistance. Then, we stopped the FCE process when the resistance of the devices reached the desired value. In order to estimate the resistance, the electrical characteristics of the devices were measured. Subsequently, we updated the desired resistance value and then we repeated this procedure to accurately control the resistance and to slowly form the nanogaps.

A scanning electron microscopy (SEM) image of a representative initial Ni electrode is exhibited in Fig. 3.6(a). The initial resistance of our devices was approximately 200-300  $\Omega$ . Figure 3.6(b) shows a SEM image of Ni electrode after performing the SFCE procedure. This demonstrates that a gap has been clearly formed at the nanoconstriction area of the Ni electrode.

Figure 3.7(a) shows a representative current versus voltage curve during the SFCE process, with 4 FCE steps, at room temperature. Within each FCE step, the FCE process was performed to the desired resistance  $R_D$  and was reset back to zero after the FCE process. This characteristic clearly exhibits that the conductance of the nanowire decreases smoothly by suppressing the rapid electromigration of Ni atoms. Here, the influence of SFCE parameters such as threshold differential conductance  $G_{TH}$ , feedback voltage  $V_{FB}$ , and voltage step  $V_{STEP}$  is investigated on both the resistance control of the nanowire and the process time of the procedure. Furthermore, we study the conductance variation of the nanowires in quantum point contact (QPC) regime using SFCE procedure with optimized feedback parameters. Figure 3.7(b) is the fit of Joule-heating model [25] to the data of Fig. 3.7(a). The power generated in the nanoconstriction is

estimated between 166  $\mu\text{W}$  and 834  $\mu\text{W}$ .

The current-voltage ( $I$ - $V$ ) characteristics of the nanoconstriction after performing each FCE procedure at room temperature are shown in Fig. 3.8. The number and color of current curves match with the respective number and color of current curves from Fig. 3.7(a). The current decreased gradually with increasing the desired resistance  $R_D$  from 600  $\Omega$  to 45 k $\Omega$ . Although the nanoconstriction before performing the SFCE process indicated the linear  $I$ - $V$  properties, the nonlinear  $I$ - $V$  characteristics were observed after the SFCE with  $R_D$  of 15-20 k $\Omega$ . The results suggest that the current is due to electron tunneling between Ni electrodes through the vacuum barrier. By performing the SFCE process, the resistance of the nanoconstriction can be controlled widely, ranging from a bulk-neck regime to a tunneling regime.

To investigate the control range of the resistance of Ni nanoconstrictions, we performed the SFCE scheme with optimized feedback parameters. Figure 3.9(a) shows the relationship between the desired resistance  $R_D$  and the measured resistance  $R_M$ . The measured resistance  $R_M$ , which is defined as the resistance of the nanowire in low voltage regime, was obtained after performing the SFCE cycle at room temperature. The broken lines in Fig. 3.9(a) are drawn as references, i.e.,  $R_M = R_D$  and  $R_M = 2R_D$ . In the desired resistance  $R_D = 500 \Omega$ , the measured resistance  $R_M$  is in good agreement with the  $R_D$ . As the desired resistance is increased further into the 1 k $\Omega$  range, the  $R_M$  does not correspond to the  $R_D$ . In this region, it is suggested that QPC is formed into the channel of the nanowire because nonlinear  $I$ - $V$  curves at high bias voltage regime (0.1-1 V) are obtained during the SFCE cycles [30, 31]. In Fig. 3.9(b),  $R_M$  is plotted in wider range than that of Fig. 3.9(a), as a function of  $R_D$  ranging from 0.5 to 60 k $\Omega$ .  $R_M$  was precisely controlled from 0.2 to 600 k $\Omega$  for 20 min, which is 3000 times larger than the



initial resistance of the channel. Discrete change of the channel conductance below  $1 G_0$  ( $G_0 = 2e^2/h$ ) reported in Ref. 25 was not observed during the SFCE. The results imply that thermal instability was successfully removed during SFCE procedure. In the desired resistance  $R_D$  ranging from 25 to 60 k $\Omega$ , the measured resistance  $R_M$  remains almost constant. In this region, it is considered that the tunnel gap is formed in the channel. It has been reported that electromigration successfully creates smaller nanogaps when the power dissipated in the junction is minimized [12, 24]. We estimated the power dissipated at the contact with  $R_D$  ranging from 0.5 to 4 k $\Omega$  using Joule-heating model [25]. Critical powers were obtained to be 390  $\mu$ W at  $V_{STEP} = 0.5$  mV and 830  $\mu$ W at  $V_{STEP} = 1.0$  and 1.5 mV. Hence, thermal heating can be well controlled using optimized feedback parameters without series resistance. The results indicate that we can control the channel resistance of metal nanowires ranging from metallic regime to tunneling regime through QPC regime without catastrophic breaks.

Conductance traces from  $5 G_0$  to  $3 G_0$  recorded during the SFCE with several voltage steps are shown in Fig. 3.10(a), (b), and (c). These traces correspond to the data obtained at  $R_D = 4$  k $\Omega$  in Fig. 3.9(a). Conductance plateaus and steps at and near the integer multiples of  $0.5 G_0$  are observed. These discontinuities and corresponding conductance plateaus demonstrate that the nanowire likely consists of a few atoms at its narrowest point. These conductance plateaus (in units of  $0.5 G_0$ ) indicate that the spin degeneracy of the Ni nanoconstriction has been removed, even without the application of external magnetic fields [32]. These results imply that the conductance of Ni electrodes was stably controlled with  $V_{STEP}$ . Furthermore, the control time to adjust the conductance from  $5 G_0$  to  $3 G_0$  is successfully decreased from 270 to 35 sec as  $V_{STEP}$  is increased from 0.5 to 1.5 mV. In the SFCE cycles, the applied voltage to the Ni

electrodes during the SFCE was gradually increased from 1.1 to 1.4 V at  $V_{STEP} = 0.5$  mV and from 1.3 to 1.8 V at  $V_{STEP} = 1.0$  and 1.5 mV, but the conductance variation was not affected by the applied voltage. These results suggest that process time of SFCE procedure in QPC regime can be considerably shortened by optimizing  $V_{STEP}$ , without degradation of the controllability of the resistance of Ni nanoconstrictions.

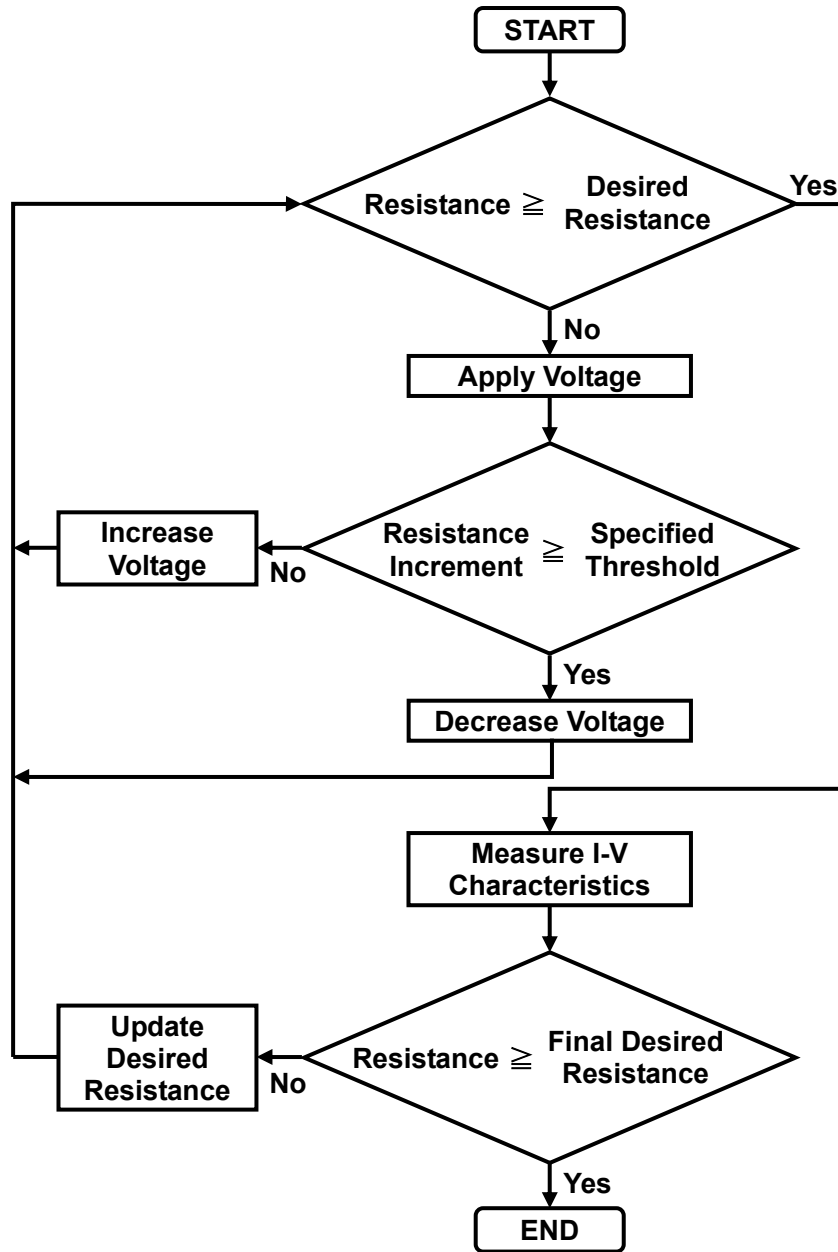


Fig. 3.5. Flowchart of stepwise feedback-controlled electromigration (SFCE).

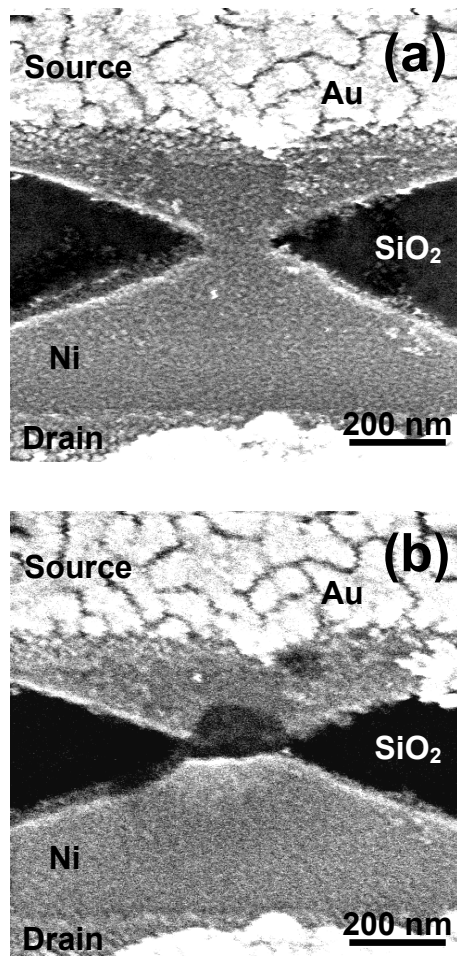


Fig. 3.6. SEM images of a Ni electrode (a) before and (b) after SFCE procedure.

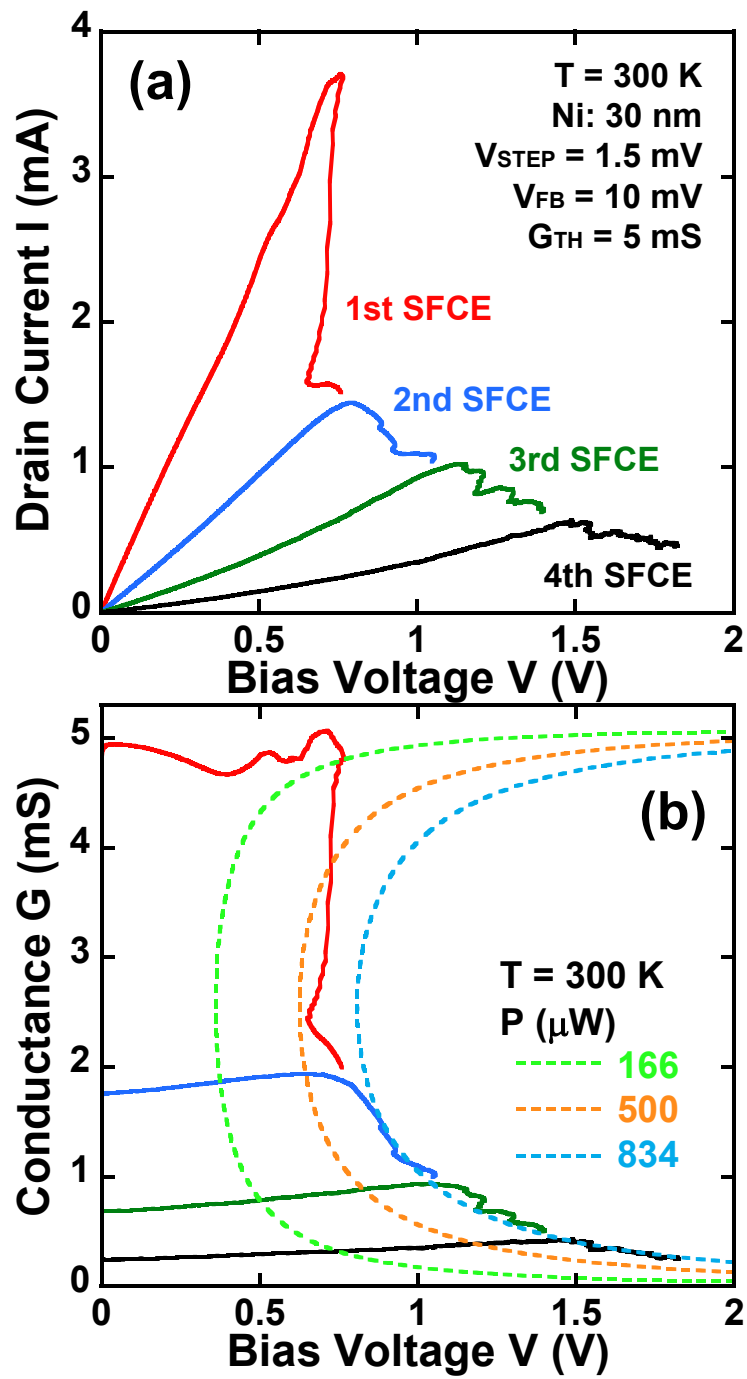


Fig. 3.7. (a) Drain current versus bias voltage characteristics obtained during the SFCE. (b) Fit of Joule-heating model to the data of Fig. 3.7 (a).

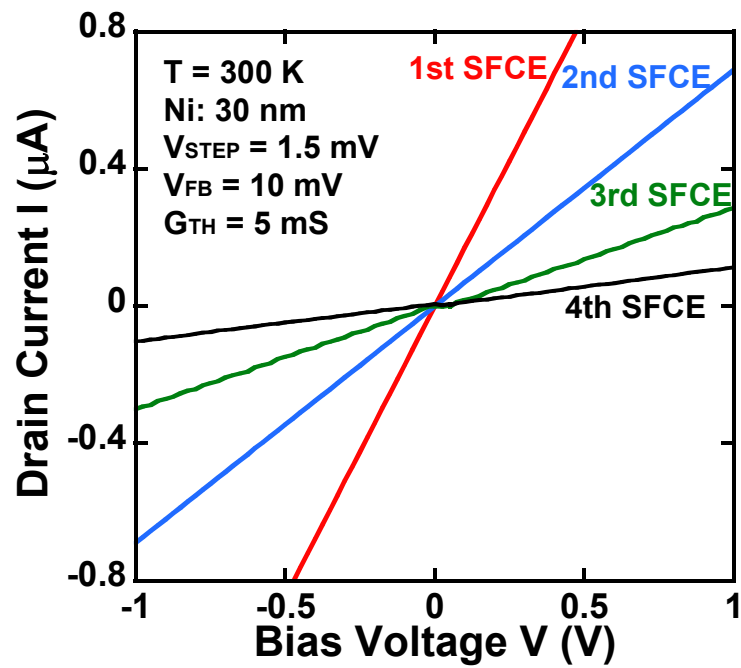


Fig. 3.8.  $I$ - $V$  characteristics measured after the nanogap formation procedure. The number and color of current curves matches with the respective number and color of current curves from Fig. 3.7(a).

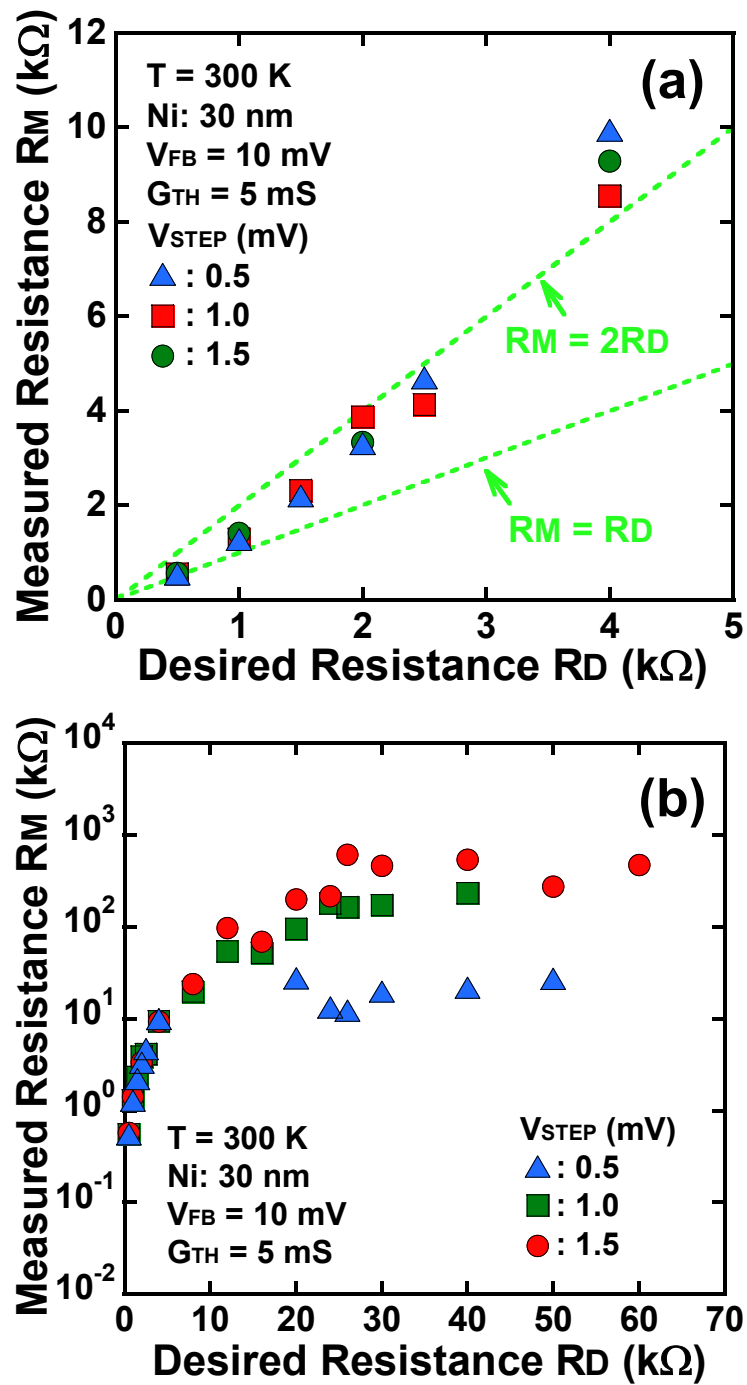


Fig. 3.9. Measured resistance  $R_M$  as a function of desired resistance  $R_D$  ranging from (a) 0.5 to 4  $\text{k}\Omega$  and (b) 0.5 to 60  $\text{k}\Omega$ .

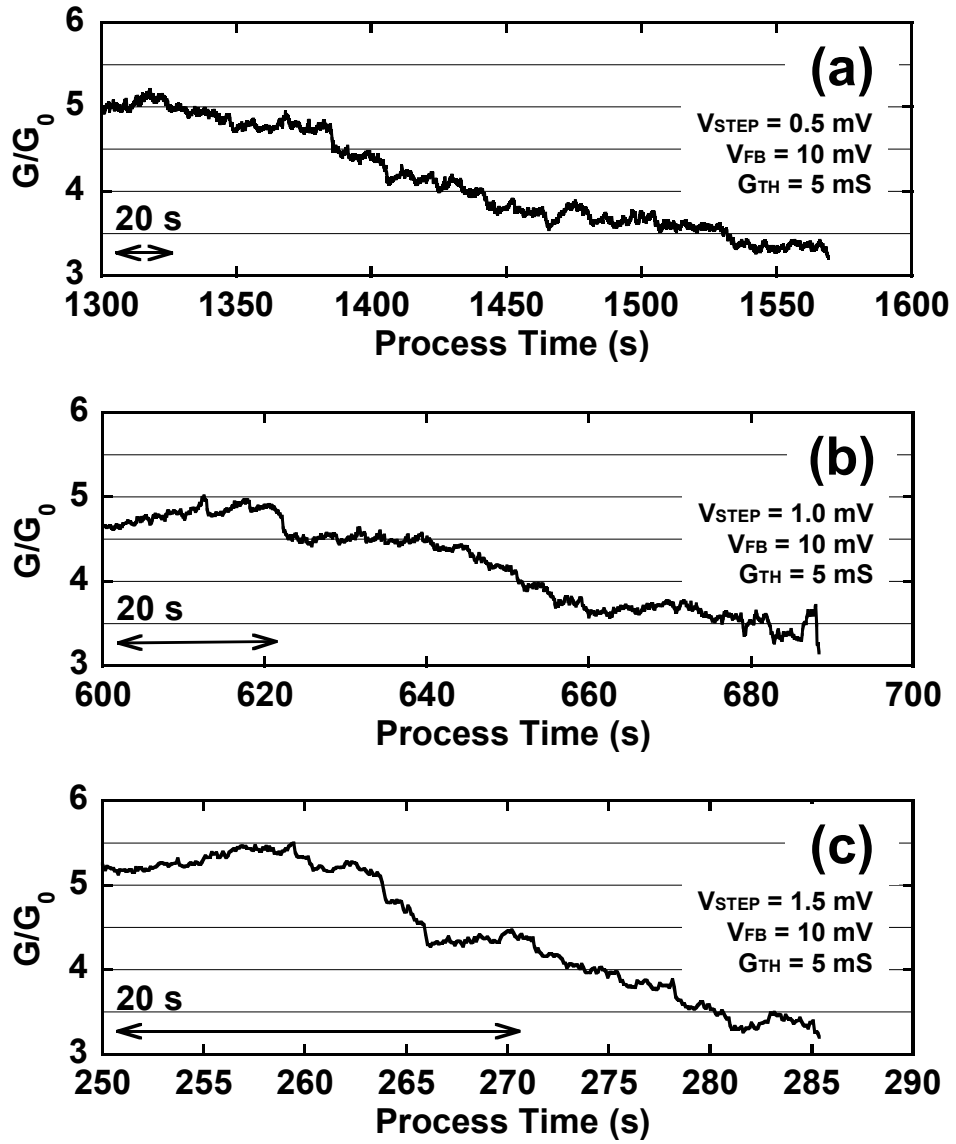


Fig. 3.10. Conductance traces recorded during SFCE with parameters of  $G_{TH} = 5 \text{ mS}$ ,  $V_{FB} = 10 \text{ mV}$ , and  $V_{STEP} =$  (a)  $0.5 \text{ mV}$ , (b)  $1 \text{ mV}$ , and (c)  $1.5 \text{ mV}$ .



### 3.4 Field-Emission-Induced Electromigration

A number of techniques for the fabrication of nanogap electrodes using electromigration (EM) have already been investigated. However, for the fabrication of tunnel junction devices, a novel method for controlling the tunnel resistance is required. We have investigated that the control of the tunnel resistance of the nanogaps is performed by field-emission-induced EM [12-14], which is the so called “activation”. The tunnel resistance of the nanogaps was controlled by only the magnitude of the preset current during the activation.

Activation scheme is based on the motion of atoms induced by Fowler-Nordheim (F-N) field emission current at nanogaps [12-14]. Figure 3.11(a) shows the schematic of an initial nanogap. By applying bias voltages, a field emission current flows through the initial nanogap. The metal atoms at the tip of the source electrode are activated by the field emission current, as shown in Fig. 3.11(b). Then, activated atoms move from source to drain electrode by electron wind force, which is always caused along the direction of electron flow (figure 3.11(c)). Finally, hillock is formed by accumulated atoms at the tip of drain electrode, resulting in a decrease of the separation of the initial nanogap, as shown in Fig. 3.11(d). Consequently, the tunnel resistance of the nanogaps after performing the activation becomes smaller than that before the activation.

As shown in Fig. 3.12, the detailed experimental steps of the activation process are as follows. First, we set the magnitude of the preset current  $I_s$ . Then, we applied the bias voltage  $V$  to the initial nanogap electrodes and ramped up the voltage while monitoring the current  $I$  passing through the gap. When the field emission current  $I$  reached the preset current  $I_s$ , we stopped the application of the voltage  $V$  to the gap. Here, the voltage  $V_s$  is defined as the voltage  $V$  at which the current  $I$  is the same as the

preset current  $I_s$ . Figure 3.13(a) shows representative current-voltage ( $I$ - $V$ ) characteristics during the activation with the preset current  $I_s = 1 \mu\text{A}$ . From this figure, a resistance  $R_s$  and a differential resistance during the activation are given by  $V_s/I_s$  and  $dV_s/dI_s$ , respectively. After that, hillock is formed by accumulation of atoms at the tip of the drain electrode, resulting in a decrease of the separation of the nanogap electrodes. Finally, the tunnel resistance of the nanogaps was measured from electrical properties after performing the activation. Figure 3.13(b) shows  $I$ - $V$  property of the nanogap after performing the activation with the preset current  $I_s = 1 \mu\text{A}$ . We define the resistance at low bias voltage regime as the tunnel resistance  $R$ . By monitoring the current  $I$  passing through the gap, we are easily and simply able to control the resistance of nanogap electrodes. The activation and measurement of the tunnel resistance were continuously repeated to the same nanogap with increasing the preset current  $I_s$  from 1 nA to 150  $\mu\text{A}$ .

Figure 3.14(a) shows a scanning electron microscopy (SEM) image of representative nanogap electrodes with asymmetrical shape before performing the activation. In this figure, the gap separation is approximately 60 nm, which is completely defined by electron-beam lithography. On the other hand, an SEM image of the nanogap electrodes after performing the activation with the preset current  $I_s$  of 150  $\mu\text{A}$  is shown in Fig. 3.14(b). The figure clearly indicates that the separation of the gap reduces from about 60 nm before the activation to less than 10 nm after the activation, which is due to accumulation of metal atoms at the tip of the drain electrode. The SEM images before and after the activation suggest that the initial gap separation is obviously reduced by performing the activation.

Figure 3.15 shows the  $I$ - $V$  characteristics of the nanogaps after the activation with the preset current  $I_s$  from 300 nA to 2  $\mu\text{A}$ . When the preset current  $I_s$  is set to 300 nA,

the  $I$ - $V$  shows the high resistive property. On the other hand, the nonlinear  $I$ - $V$  characteristics are obtained in  $I_s$  of 400 nA and 1  $\mu$ A, suggesting the tunneling properties of the nanogaps. In addition, the linear property is obtained when the preset current  $I_s$  is set to 2  $\mu$ A, which shows almost metallic behavior. The  $I$ - $V$  properties plotted on semi-log scale are shown in the inset of Fig. 3.15. The current through the nanogaps increases from the order of 10 fA to 1 nA with increasing the preset current  $I_s$  from 300 nA to 2  $\mu$ A. These results imply that the wide range control of electrical properties of the nanogaps is achieved by performing the activation.

Figure 3.16(a) shows the relation between the resistances and the preset current  $I_s$  during the activation of nanogaps with asymmetrical shape. In this figure, three kinds of resistances are shown, such as tunnel resistance  $R$  of the nanogaps, resistance  $R_s$  when the bias voltage is stopped in the activation, and differential resistance  $dV_s/dI_s$  during the activation. The tunnel resistance  $R$  decreases from the order of 100 T $\Omega$  to 100 k $\Omega$  with increasing the preset current  $I_s$  from 1 nA to 150  $\mu$ A. As the preset current  $I_s$  is smaller than 100 nA, the nanogaps still show the high resistive properties. On the other hand,  $I$ - $V$  shows the metallic properties as the preset currents  $I_s$  becomes larger than 10  $\mu$ A. In the preset current  $I_s$  from 100 nA to 10  $\mu$ A, the nanogaps show the tunneling properties, which is the transition of electrical properties from insulating regime to metallic regime. This result implies that the tunnel resistance of the nanogap is controlled and adjusted by the magnitude of the preset current  $I_s$  in the activation. From this figure,  $R_s$  and  $dV_s/dI_s$  decrease with increasing the preset current  $I_s$  and show a linear relation with a slope of -1, suggesting that the current passing through the gap is based on F-N field emission [12-14]. It is noted that the tunnel resistance  $R$  could be predicted from the relation between  $R$  and  $R_s$  or  $R$  and  $dV_s/dI_s$ . Figure 3.16(a), obtained from the nanogaps

having asymmetrical shape, is quite similar to the results of nanogaps with symmetrical shape shown in Fig. 3.16(b), which are our previous results [12-14]. Hence, the control of the tunnel resistance of the nanogaps using activation process strongly depends on the preset current  $I_s$  but is hardly affected with the shape of the nanogap electrodes.

The tunnel resistance  $R$  versus initial gap separation with several preset currents  $I_s$  is shown in Fig. 3.17. In a fixed preset current  $I_s$ , the tunnel resistance  $R$  does not depend on the initial gap separation. In particular, if the preset current  $I_s$  is set to 3  $\mu\text{A}$ , one can obtain the tunnel resistance  $R$  of 100  $\text{M}\Omega$  in spite of the variation of the initial gap separation. From this figure, it is found that the tunnel resistance  $R$  is independent on the initial gap separation and well controlled by only the preset current  $I_s$ .

Figure 3.18(a) shows Fowler-Nordheim (F-N) plots of the nanogap during activation with the preset current of 500 nA, 1  $\mu\text{A}$ , and 5  $\mu\text{A}$ . The width of the nanogap was calculated from Fig. 3.18(a). The equation of F-N is given by [33]

$$J = \frac{e^3}{8\pi h} \left( \frac{m_0}{m^*} \right) \frac{1}{\phi} E^2 \exp \left\{ - \frac{8\pi}{3he} \sqrt{2 \frac{m^*}{m_0}} \phi^{1.5} \frac{1}{E} \right\}, \quad (3.1)$$

where  $e$  is the electron charge,  $h$  is the Planck Constant,  $m_0$  is the free electron mass,  $m^*$  is the effective mass of electron,  $\phi$  is the potential barrier, and  $E$  is the electric field.

This equation is also expressed by

$$\ln \frac{I}{V^2} = -6.828 \times 10^7 \sqrt{\frac{m^*}{m_0}} \phi^{1.5} w \frac{1}{V} + \ln \left( 1.5413 \times 10^{-6} \left( \frac{m_0}{m^*} \right) \frac{S}{\phi} \frac{1}{w^2} \right), \quad (3.2)$$

where  $S$  is the cross section of the gap and  $w$  is the gap separation between source and drain electrode. Equation (3.2) exhibits the dependence between  $\ln(I/V^2)$  and  $1/V$ . Here, the slope of Eq. (3.2) is defined as  $A$ , gap separation  $w$  is described by

$$W = - \frac{A}{\phi^{1.5} \times 6.828 \times 10^7} \sqrt{\frac{m_0}{m^*}}, \quad (3.3)$$

where  $\varphi$  is 4 eV, which is work function of Ni [12]. Figure 3.18(b) shows dependence of tunnel resistance and gap separation of nanogap on the preset current  $I_s$ . Gap width of the nanogap decreases from with increasing the preset current, which is similar to the tunnel resistance. These results imply that the width of the nanogap can be controlled by adjusting the preset current  $I_s$ .

Number of metal atoms moving from source to drain electrode can be estimated using the atom drift velocity in a metal due to electric currents. The atom drift velocity  $v$  is given by [34]

$$v = \frac{D_0}{kT} eZ^* \rho j \exp\left(-\frac{\Delta H}{kT}\right), \quad (3.4)$$

where  $k$  is the Boltzmann's constant,  $T$  is the absolute temperature,  $eZ^*$  is the effective charge of the metal ions,  $\rho$  is the metal resistivity,  $j$  is the electric current density,  $\Delta H$  is the activation energy for diffusion of the moving defects, and  $D_0$  is the diffusion constant. If the moving atoms are assumed to be one atomic layer of the surface of the source electrode, the number of moving atoms  $n$  is approximated by

$$n = V \cdot N = w \cdot a \cdot v \cdot t \cdot N = 4.9 \times 10^{-6} \times \left(w \cdot a \cdot \frac{N}{S}\right) \int i(t) dt, \quad (3.5)$$

where  $V$  is the volume of moving atoms,  $N$  is the atomic density,  $w$  is the width of source electrode,  $a$  is the one atomic layer thickness,  $t$  is the activation time,  $S$  is the cross section at the tip of source electrode, and  $i$  is the current during activation. From this assumption, the number of moving atoms  $n$  is estimated to be  $10^5$  atoms by applying the preset current  $I_s$  of 150  $\mu$ A. On the other hand, accumulated metal atoms at the tip of the drain electrode could also be determined from the area of the hillock shown in the SEM image of Fig. 3.14(b) and is obtained to be  $10^6$  atoms. Thus, the number of moving atoms estimated from the SEM image is similar to that from the

assumption based on equation (3.5). On the other hand, fabrication procedure of nanogaps using activation is similar to field evaporation using the scanning tunneling microscope (STM). Number of atoms moving from STM tip to sample surface is  $10^4$ - $10^6$  [35-38], which is roughly corresponding to our activation system. These results suggest that the moving atoms in STM and activation system are induced by field-emission-current. Furthermore, this estimation implies that  $10^{11}$  electrons are required for the motion of an atom during the activation with the preset current  $I_s$  of  $150 \mu\text{A}$ . This result suggests that field emission current causes the electromigration and is significant for the activation procedure.

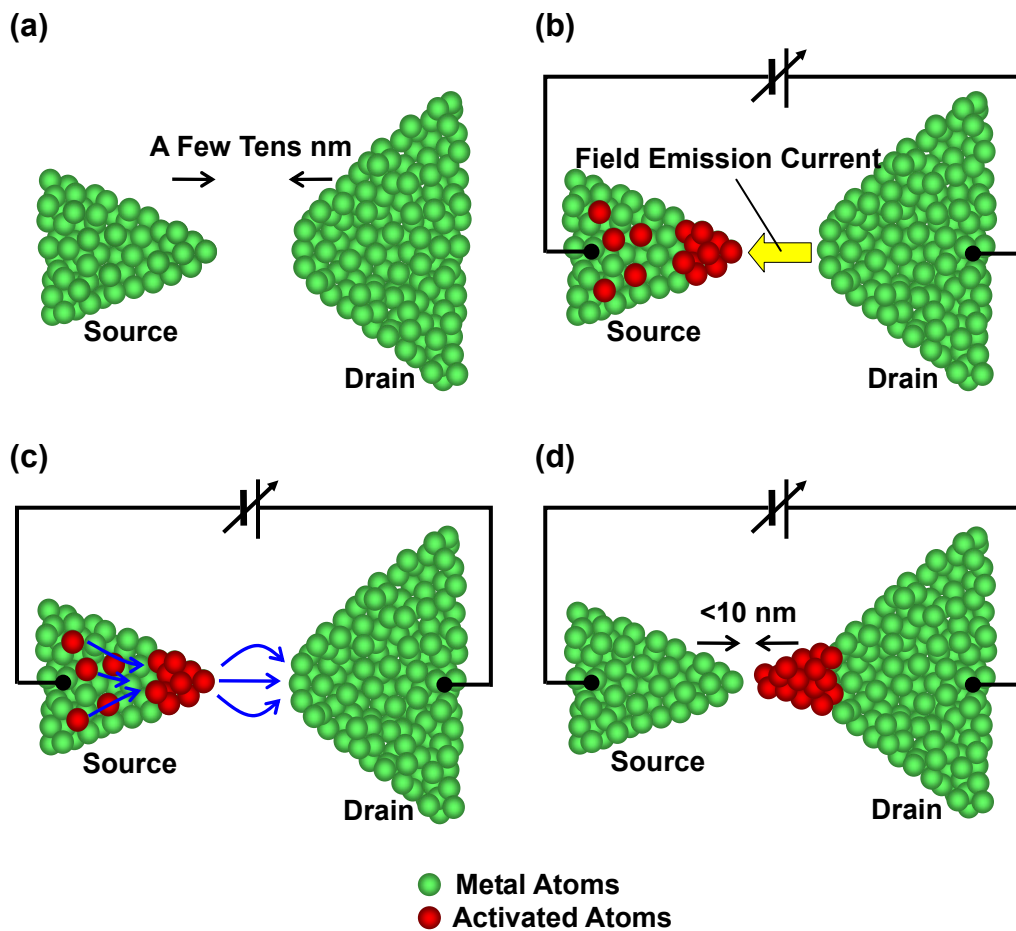


Fig. 3.11. Schematic of the activation procedure. (a) Initial nanogap before performing the activation. (b) Filed emission current passes through the initial nanogap by applying bias voltage. (c) Metal atoms at the source electrode are activated by field emission current. (d) Hillock is formed by accumulation of activated atoms at the tip of the drain electrode.

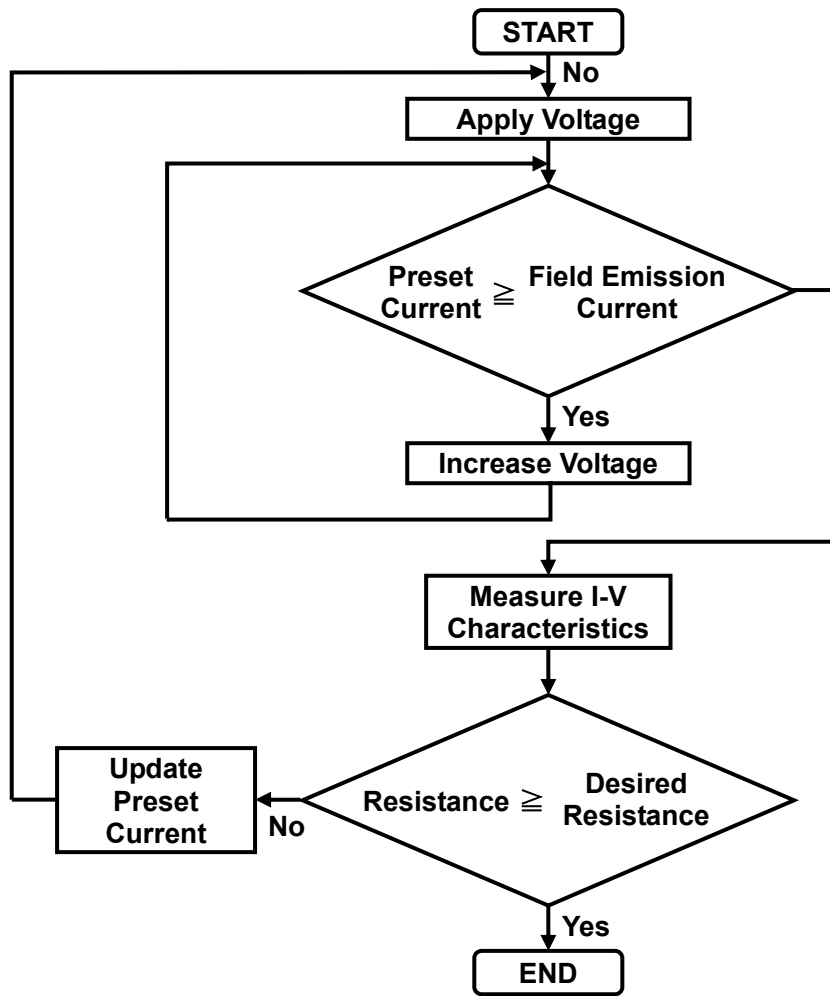


Fig. 3.12. Flowchart of activation procedure.



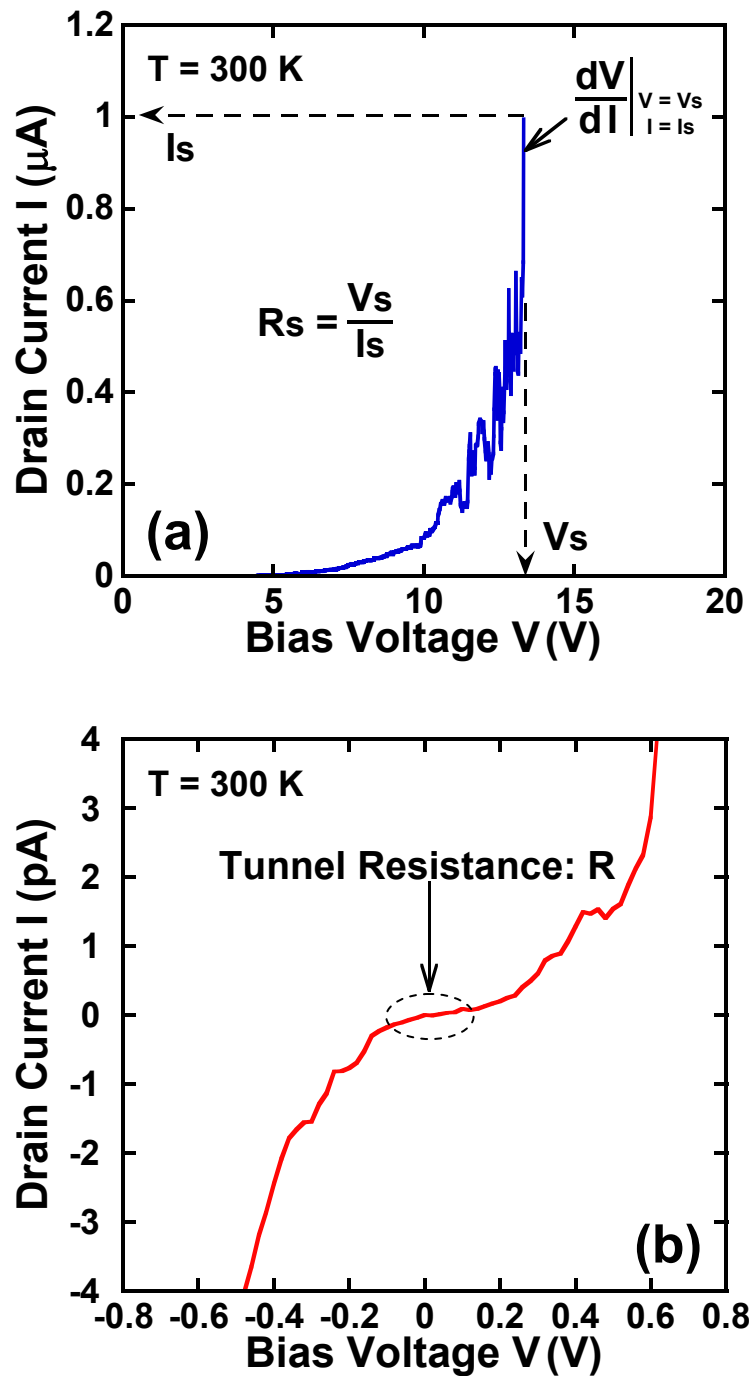


Fig. 3.13. Representative  $I$ - $V$  characteristics of the nanogap (a) during and (b) after the activation with the preset current  $I_s$  of  $1\ \mu\text{A}$  at room temperature.

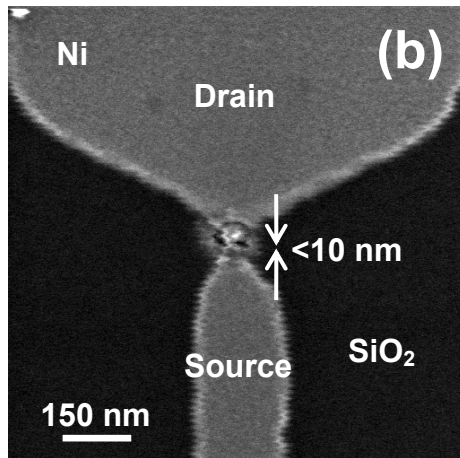
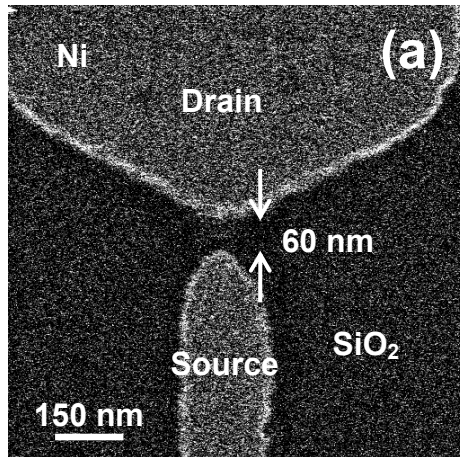


Fig. 3.14. SEM images of a representative Ni nanogap (a) before and (b) after performing the activation.

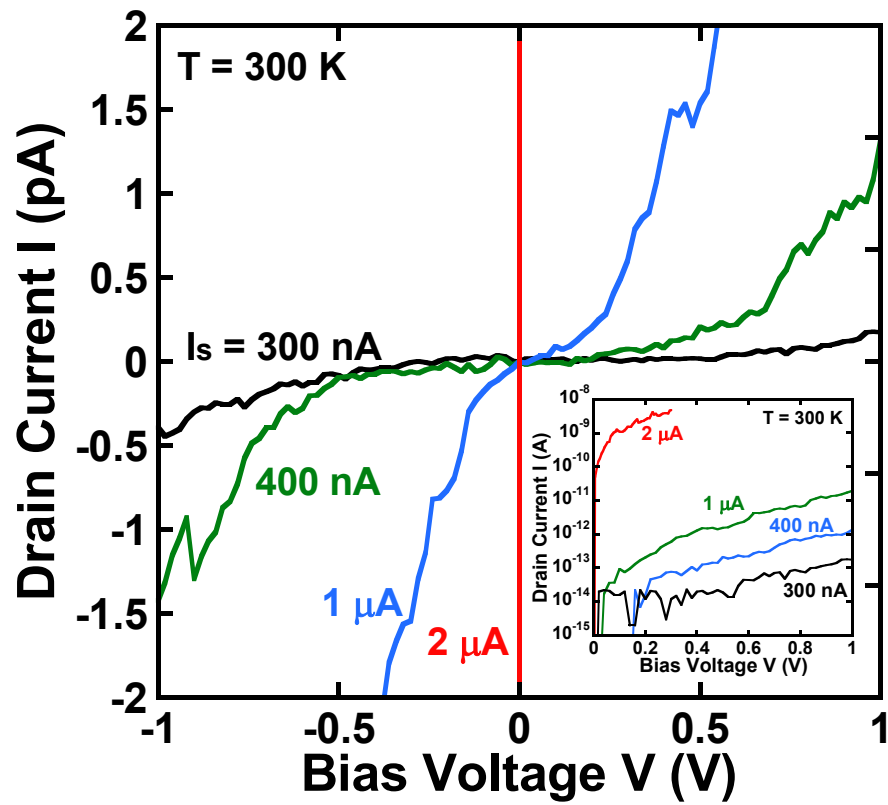


Fig. 3.15.  $I$ - $V$  characteristics of the nanogap with the preset current  $I_s = 300$  nA, 400 nA, 1  $\mu$ A, and 2  $\mu$ A at room temperature. The inset shows the  $I$ - $V$  curves plotted on a semilogarithmic scale.

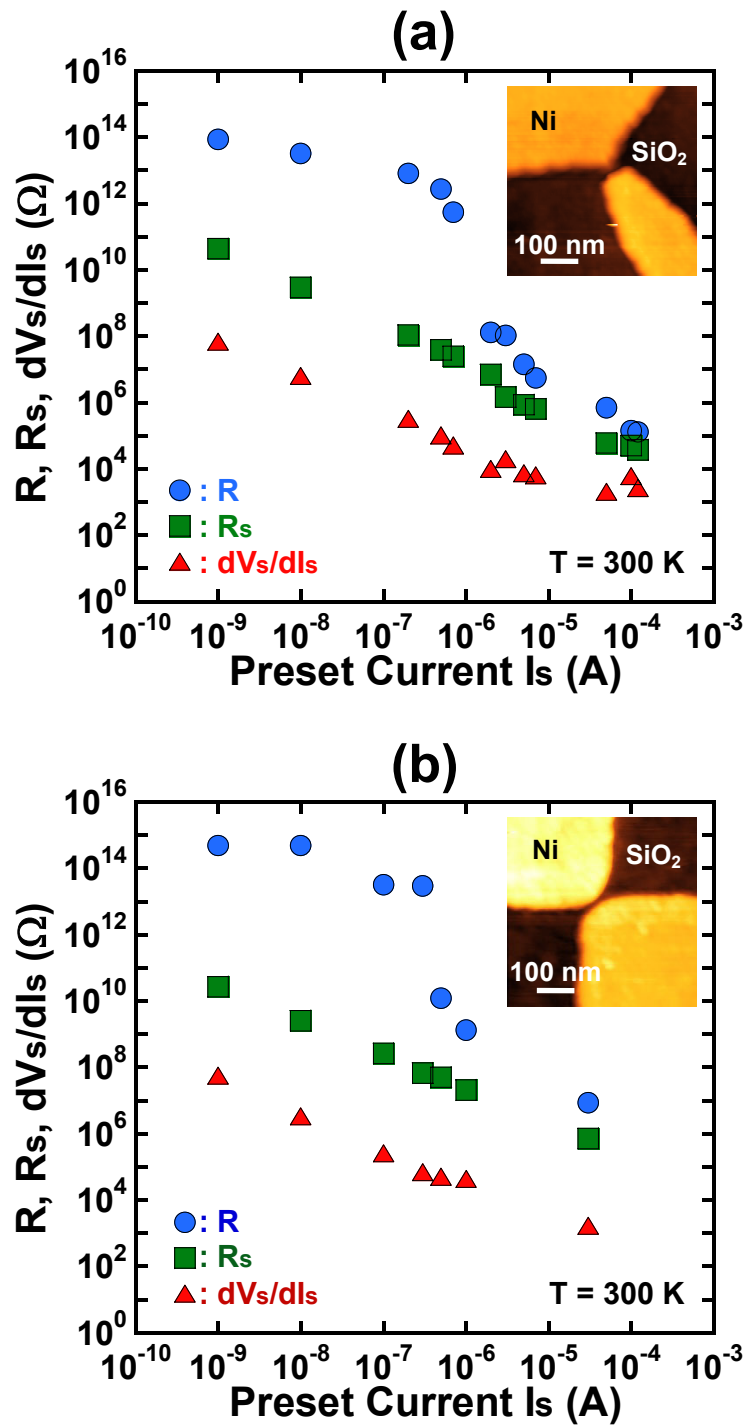


Fig. 3.16. Dependence of resistance of the nanogaps with (a) asymmetrical and (b) symmetrical shape on the preset current  $I_s$ .

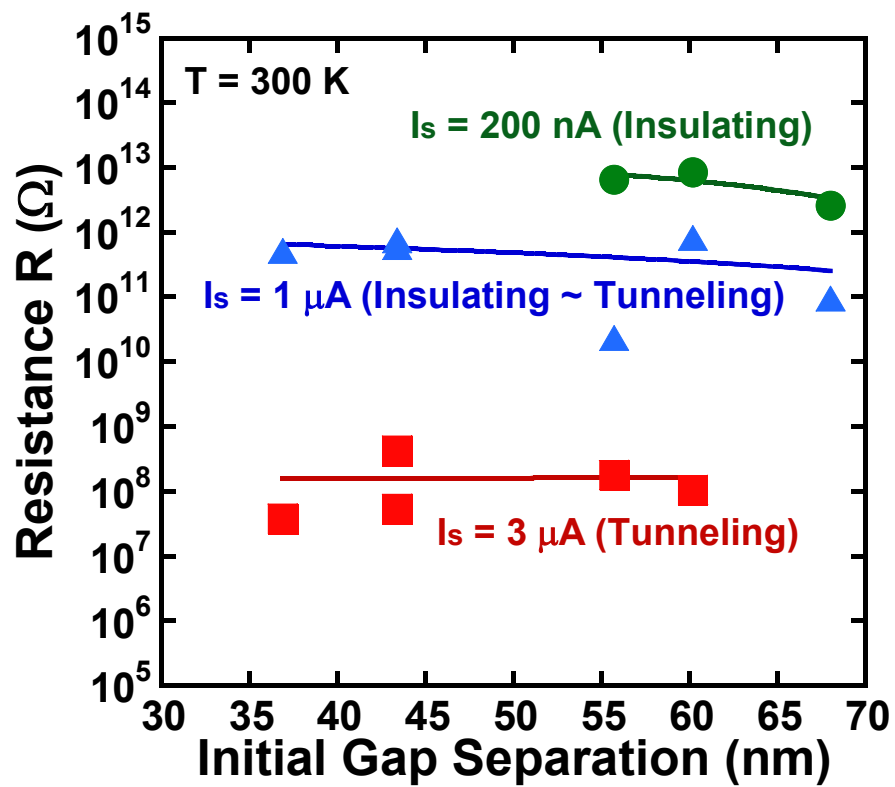


Fig. 3.17. Dependence of the tunnel resistance  $R$  of the nanogaps on the initial gap separation with the preset current  $I_s = 200$  nA,  $1$   $\mu$ A, and  $3$   $\mu$ A.

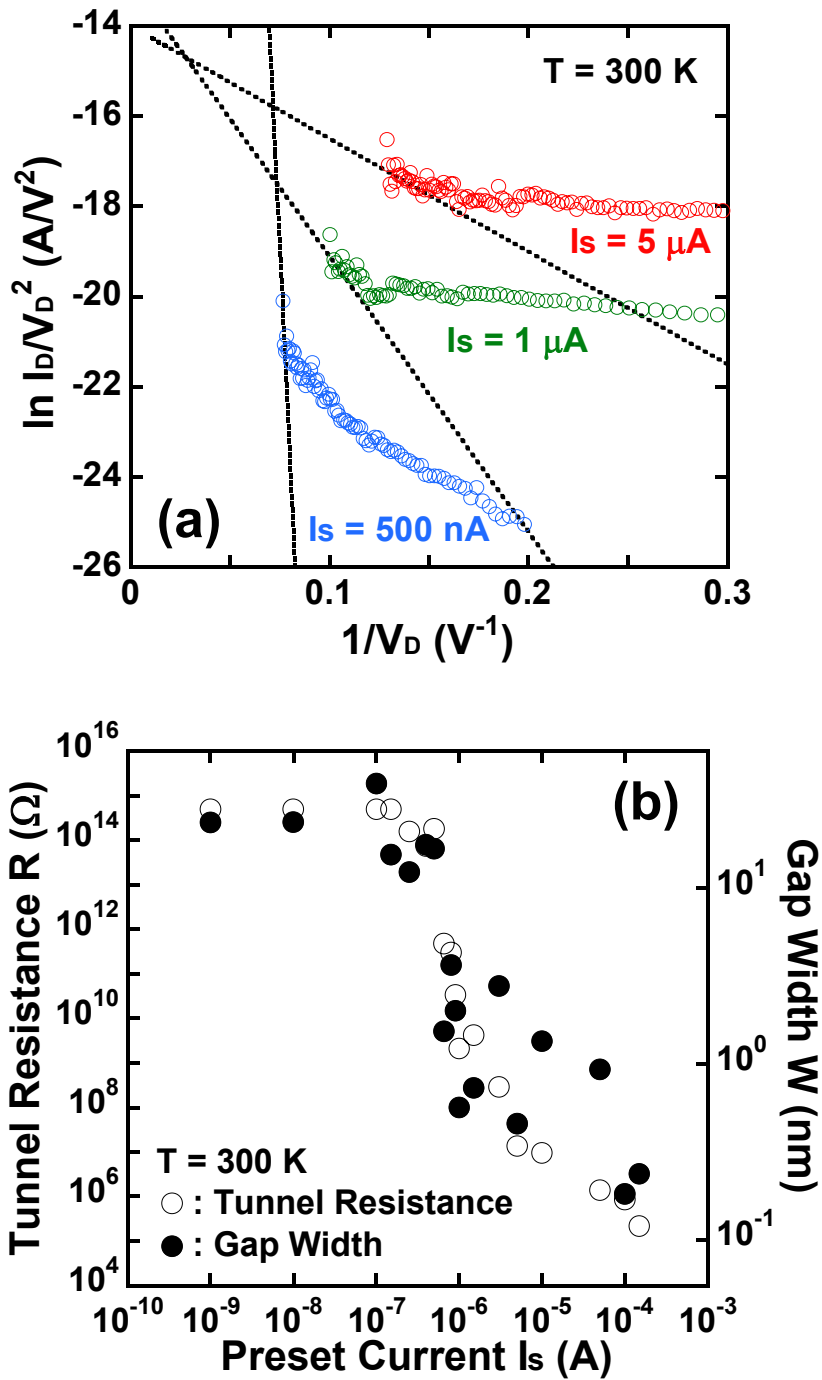


Fig. 3.18. (a) F-N plot of the nanogap with the preset current of 500 nA, 1  $\mu\text{A}$ , and 5  $\mu\text{A}$ . (b) Dependence of tunnel resistance and gap width of the nanogaps on the preset current  $I_s$ .

### 3.5 Summary

We have investigated simple and easy techniques for the fabrication of planar-type ferromagnetic tunnel junctions. Scanning probe microscopy (SPM) local oxidation was applied for the Ni thin films. The size of the Ni oxide wires was controlled by changing the applied bias voltages and scanning speed. Ultra-fine Ni oxide wires were obtained by SPM local oxidation method under the applied AC bias voltage. These results imply that the SPM local oxidation using AC bias voltage produces higher controllability for the local oxidation nanolithography of ferromagnetic thin films.

On the other hand, nanometer gaps were fabricated by novel techniques based on electromigration (EM). In order to remove thermal effects based on feedback-controlled EM (FCE) mechanisms, for the control of the resistance of nanoconstrictions. Using stepwise feedback-controlled EM (SFCE) method, the resistance of nanoconstrictions was adjusted from insulating regime to tunneling regime. These results suggest that the resistance of nanoconstrictions can be easily controlled by SFCE procedure.

Furthermore, field-emission-induced EM (activation) method was investigated for the formation of nanogap, which is based on field emission current. The resistance of the nanogaps was controlled from 100 T $\Omega$  to 100 k $\Omega$  by the preset current during activation procedure. The current-voltage characteristics of the nanogaps measured after the activation exhibited insulating, tunneling, and metallic properties, depending on the magnitude of the preset current. This implies that activation technique can easily control and adjust the tunnel resistance of the nanogap.

## **Chapter 4**

# **Planar-Type Ni-Ni oxide-Ni Ferromagnetic Tunnel Junctions Obtained by Scanning Probe Microscopy Local Oxidation**

### **4.1 Introduction**

Scanning probe microscopes (SPMs) are focused on not only observation tools but also nanolithography tools. Local oxidation nanolithography using SPM is able to oxidize materials surfaces on the nanometer scale [1]. This oxidation process is considered to be anodic oxidation, which is driven by the applied voltage between SPM tip and sample surface. The size of oxide wires can be controlled by bias voltage, scanning speed, scanning mode and humidity. We have reported SPM local oxidation nanolithography of ferromagnetic thin films and planar-type ferromagnetic tunnel junctions [2–4]. In this chapter, planar-type Ni-Ni oxide-Ni ferromagnetic tunnel junctions with asymmetrical channel structure are fabricated by SPM local oxidation nanolithography. Magnetoresistance (MR) characteristics are also investigated in the devices with various sizes of the junctions.



## 4.2 Planar-Type Ni-Ni oxide-Ni ferromagnetic Tunnel Junctions

Figure 4.1 shows the schematic of planar-type Ni-Ni oxide-Ni ferromagnetic tunnel junction fabricated by scanning probe microscopy (SPM) local oxidation technique. Ni thin films were deposited on SiO<sub>2</sub>/Si substrates by EB evaporation. The thickness of the Ni thin films is 5-10 nm. Then, constricted channel structures were patterned on the Ni by conventional optical lithography and etching processes. Each Ni pattern consists of channel with width of typically 1-4 μm connected to large contact pads with an area of 200×200 μm<sup>2</sup>. Furthermore, focused ion beam (FIB) lithography was applied to the channels, in order to induce magnetic shape anisotropy. The accelerating voltage of Ga ion beam, emission current and etching rate were 30 kV, 2 μA and ~0.5 nm/sec, respectively. Finally, for the observation of magnetoresistance (MR) difference across the planar-type ferromagnetic tunnel junctions, insulating Ni oxide barriers were formed by the SPM local oxidation at the center of the asymmetrical constricted channels. The typical oxidation parameters were the static voltage of 6 V and scanning speed of 5 nm/sec. The area of the junction is around 5×500 nm<sup>2</sup>.

Representative current-voltage (*I-V*) characteristics of a planar-type Ni-Ni oxide-Ni ferromagnetic tunnel junction at 17 K are shown in Fig. 4.2. As shown in Fig. 4.2, nonlinear *I-V* characteristics are clearly observed. This result suggests that Ni oxide wires formed by SPM local oxidation technique act as an insulating barrier material for the electron. The *I-V* properties at 17 K were fitted by Simmons theory [5], and the effective barrier height and effective barrier thickness were obtained as shown in Table 4.1. The effective barrier width are narrower than the width of Ni oxide wires.

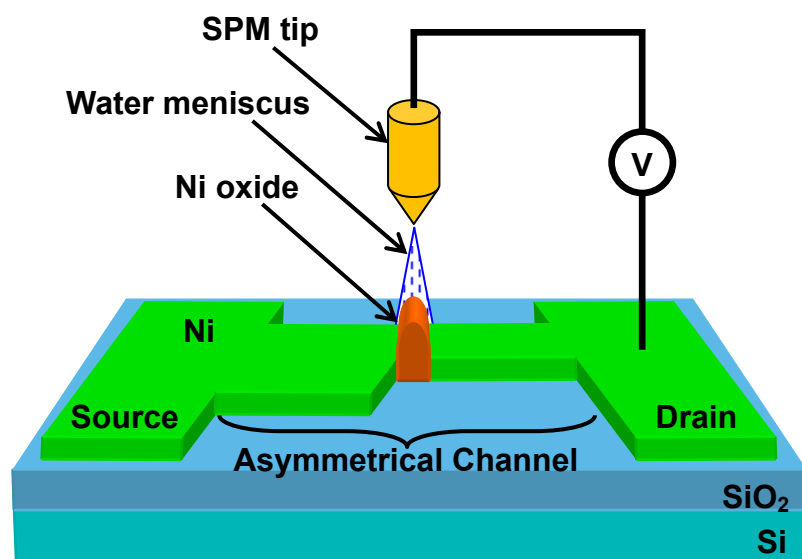


Fig. 4.1. Fabrication step of planar-type Ni-Ni oxide-Ni ferromagnetic tunnel junction fabricated by SPM local oxidation. Ni oxide barrier is formed at the center of the asymmetrical constricted channel.

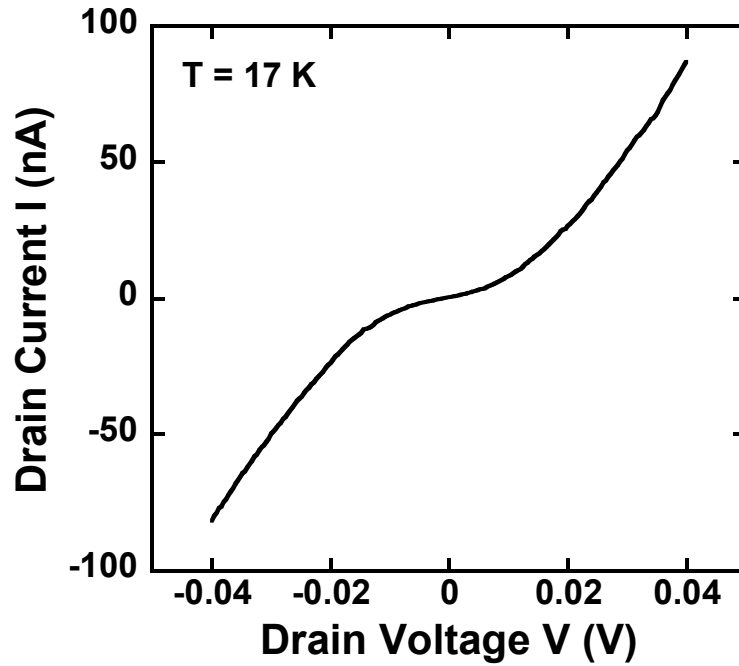


Fig. 4.2. Representative  $I$ - $V$  properties of planar-type Ni-Ni oxide-Ni ferromagnetic tunnel junction fabricated by SPM local oxidation.

Table 4.1. The width of Ni oxide barrier formed by SPM local oxidation and the effective barrier width and height.

Oxide Width (nm)	Effective Barrier Width (nm)	Effective Barrier Height (eV)
29-65	2.063	0.444
34-67	2.370	0.330
36-54	1.995	0.615
29-35	1.970	0.550

## 4.3 Magnetoresistance Properties

### 4.3.1 Channel Constriction Using Focused Ion Beam

#### 4.3.1.1 Devices with Constricted Channel Width of 1.5 $\mu\text{m}$

Figure 4.3 shows scanning electron microscopy (SEM) and atomic force microscopy (AFM) images of planar-type ferromagnetic Ni-Ni oxide-Ni tunnel junction fabricated by scanning probe microscopy (SPM) local oxidation technique. In this device, Ni channel was constricted by focused ion beam (FIB) before fabrication of Ni oxide wire. Figure 4.4(a) shows the magnetoresistance (MR) curves at 16 K. The applied bias voltage is changed ranging from 0.15 to 0.4 mV. The MR curves with higher bias voltages are shown in Fig. 4.4(b). The MR behavior of the planar-type Ni-Ni oxide-Ni ferromagnetic tunnel junction was clearly observed and increased on decreasing the applied bias voltage.

Figure 4.5 exhibits MR ratio as a function of the bias voltage. The MR ratio of above 100 % was obtained at 0.15 mV. With increasing the bias voltage, the MR ratio quickly decreases from 103 % to 5 %, and shows strong dependence on the bias voltage. Since the spin polarization of Ni is  $P_{\text{Ni}} = 0.23$ , the MR ratio of planar-type Ni-Ni oxide-Ni ferromagnetic tunnel junctions is simply predicted to be  $\text{MR} = 11.2 \%$  by Julliere formula [6]. However, the maximum MR ratio of above 100 % was obtained in smaller junction devices at 16 K. Furthermore, the MR ratio strongly depends on the applied bias voltage with the range of 0.2 mV. Since phonon energies for Ni (25 and 33 mV) and NiO (48 and 68 mV) and magnon energy for NiO (107 mV) were reported [7-12], magnon and phonon excitations through Ni/NiO junction are not the origin of the MR voltage dependence. Strong dependence of MR on the bias voltage in Fig. 4.6 may be caused by the localized trap states [13] in SPM-oxidized NiO barriers, which suffer

from imperfections of the oxide. In addition, these high MR ratios may be due to the single-electron charging effect in the junctions [14] and/or the ballistic magnetoresistance effect from strongly constricted channels [15].

Figure 4.6(a) shows the MR curves at several temperatures. In this figure, the applied bias voltage was fixed at 0.5 mV, and the measurement temperature was varied from 16 to 200 K. The MR behavior of the planar-type Ni-Ni oxide-Ni ferromagnetic tunnel junction was clearly decreased on increasing the measurement temperature. The temperature dependence of the MR curves in the planar-type Ni-Ni oxide-Ni ferromagnetic tunnel junction is also shown in Fig. 4.6(b). The MR ratio decreases from 8.5 to 0.2 % with increasing the measurement temperature. The dependence of the MR ratio on the measurement temperature is generally similar to that of the conventional perpendicular magnetic tunnel junction (MTJ) stack and may be explained by increasing the influence of the thermal excitation electrons.

The shape of the hysteresis loop in the planar-type Ni-Ni oxide-Ni ferromagnetic tunnel junctions is different from that of the conventional MTJ stack and shows the minor loop behavior. In measurement of this device, the maximum field is limited to  $\pm 1200$  Oe. Therefore, the magnetic moment of the drain-side channel with higher coercive field is still pinned and hardly changes the direction following the field. The increase of coercive field in the drain-side channel may be due to the existence of the anisotropic exchange interaction between Ni channel and Ni oxide barrier [16, 17]. Since the switching behavior of the resistance at  $\pm 200$ -300 Oe also indicates a more complex magnetization reversal process, edge domain structure of the junction may play an important role for the switching process.

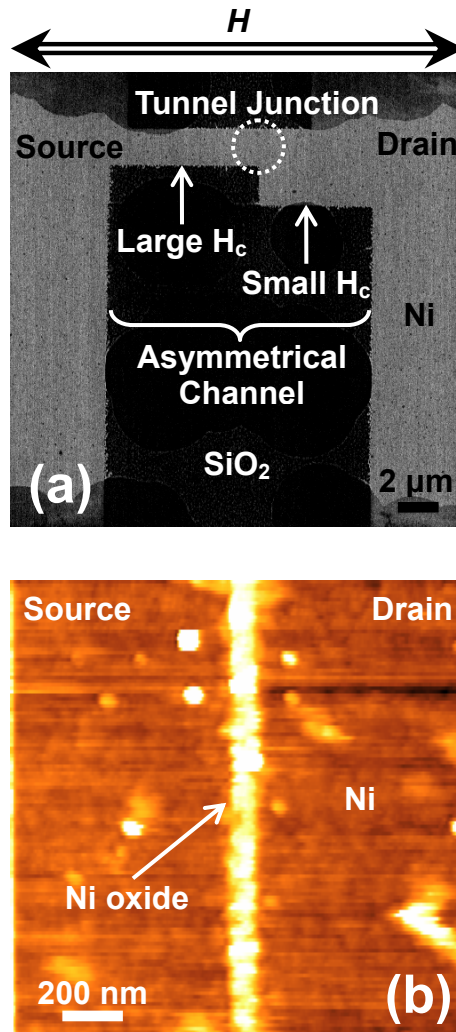


Fig. 4.3. (a) The SEM image of Ni channel constricted using FIB. (b) The AFM image of planar-type Ni-Ni oxide-Ni ferromagnetic tunnel junction fabricated by SPM local oxidation technique.

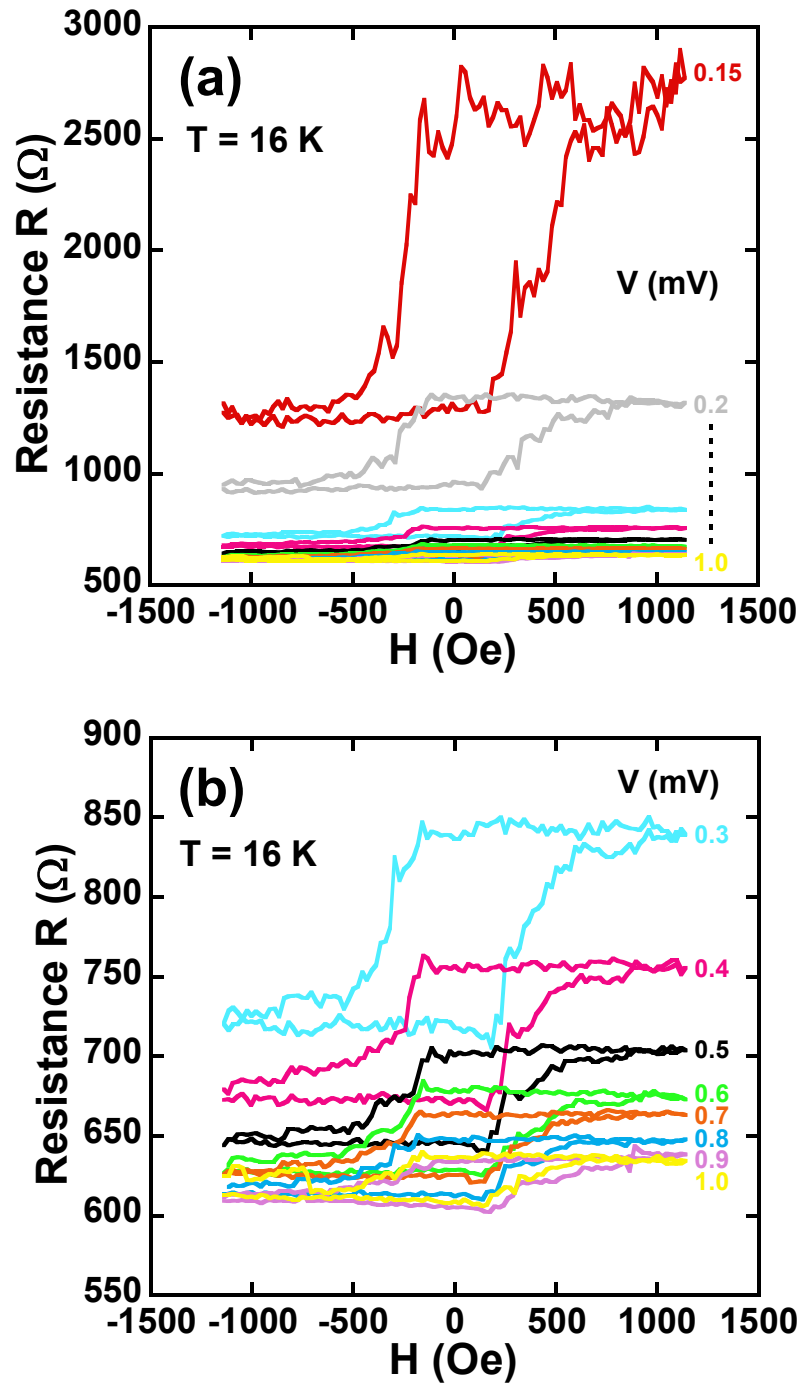


Fig. 4.4. Magnetoresistance characteristics of planar-type Ni-Ni oxide-Ni ferromagnetic tunnel junction at 16 K. Magnetoresistance curves with (a) lower bias voltages and (b) higher bias voltages.

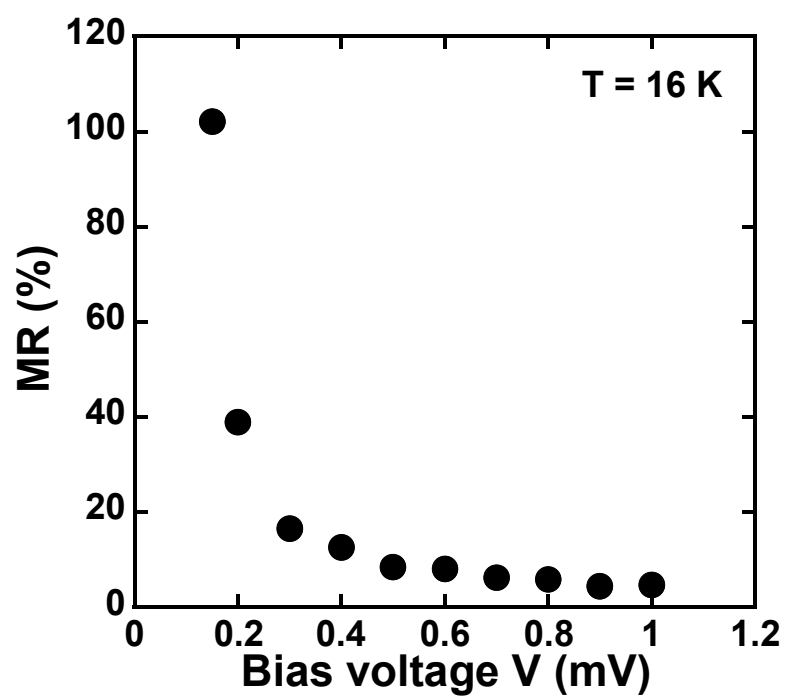


Fig. 4.5. Dependence of MR ratio on applied bias voltage in the planar-type Ni-Ni oxide-Ni ferromagnetic tunnel junction at 16 K.



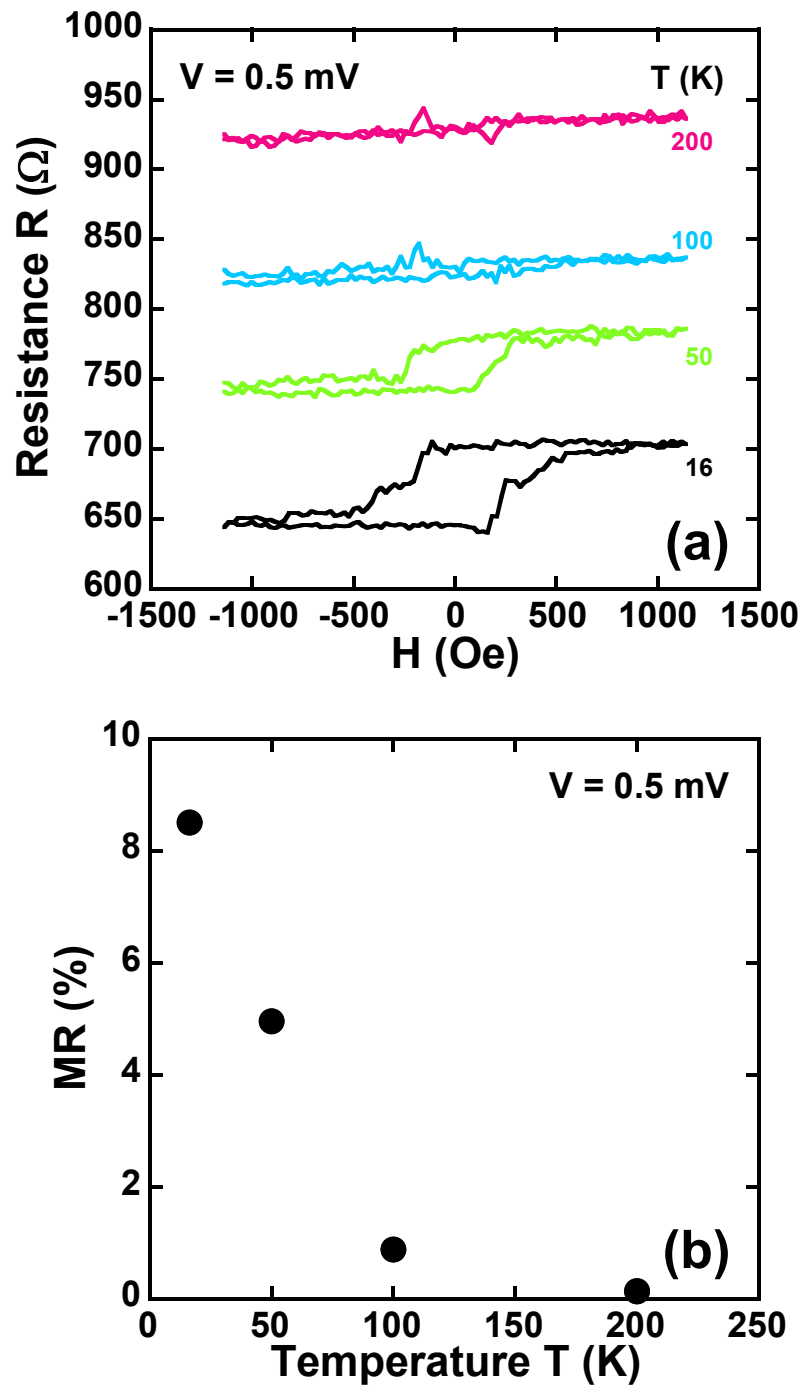


Fig. 4.6. (a) Magnetoresistance curves of planar-type Ni-Ni oxide-Ni ferromagnetic tunnel junction with measurement temperatures. (b) MR ratio as a function of measurement temperature at 0.5 mV.

#### ***4.3.1.2 Devices with Constricted Channel Width of 800 nm***

Figure 4.7(a) shows the scanning electron microscopy (SEM) of Ni channel constricted by focused ion beam (FIB) before fabrication of Ni oxide wire. Figure 4.7(b) exhibits the atomic force microscopy (AFM) image of planar-type Ni-Ni oxide-Ni ferromagnetic tunnel junction. The applied bias voltage was varied from 0.2 to 1 mV at 17 K. In this case, external magnetic field was applied parallel to the channel. Figure 4.8(a) shows the magnetoresistance (MR) curves at 16 K. The applied bias voltage is changed ranging from 0.2 to 1 mV. The MR curves with higher bias voltages are shown in Fig. 4.8(b). The MR ratio decreases from 21 % to 1.1 % with increasing the applied bias voltage from 0.2 mV to 1 mV, as shown in Fig. 4.9. Since the switching process is so complex, the resistance changes with spike-like reaction around 300 Oe. In addition, the MR curves have the typical shape of minor loop behavior as shown in Fig. 4.9, in which the drain-side (broad) channel is reversing its magnetization.

Figure 4.10(a) exhibits the MR curves at  $V = 0.5$  mV at each temperature. The MR behavior of the planar-type Ni-Ni oxide-Ni ferromagnetic tunnel junction was increased on decreasing the measurement temperature. Figure 4.10(b) shows the temperature dependence of the MR ratio in the planar-type Ni-Ni oxide-Ni ferromagnetic tunnel junction. In this figure, the MR ratio increases from 0.2 to 3.5 % with decreasing the measurement temperature from 200 to 17 K. This result implies that influence of the thermal excitation electrons decreases at low temperature. Moreover, since the Ni oxide was formed by SPM local oxidation, the barrier may be considered to be the NiO. NiO is well known not only as insulator but also as antiferromagnetic materials. Thus, the magnetization of source-side (narrow) channel may be strongly pinned by Ni oxide barrier [16, 17].

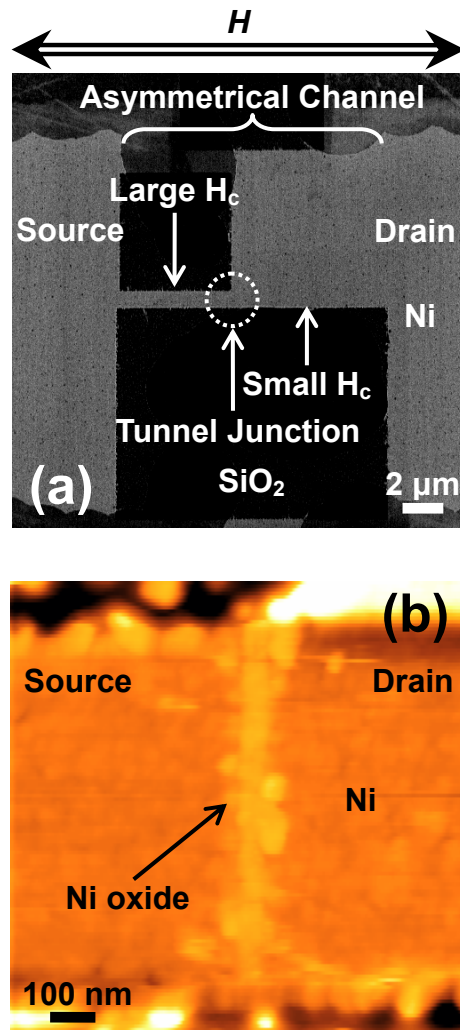


Fig. 4.7. (a) The SEM image of Ni channel constricted using FIB. (b) The AFM image of planar-type Ni-Ni oxide-Ni ferromagnetic tunnel junction fabricated by SPM local oxidation technique.

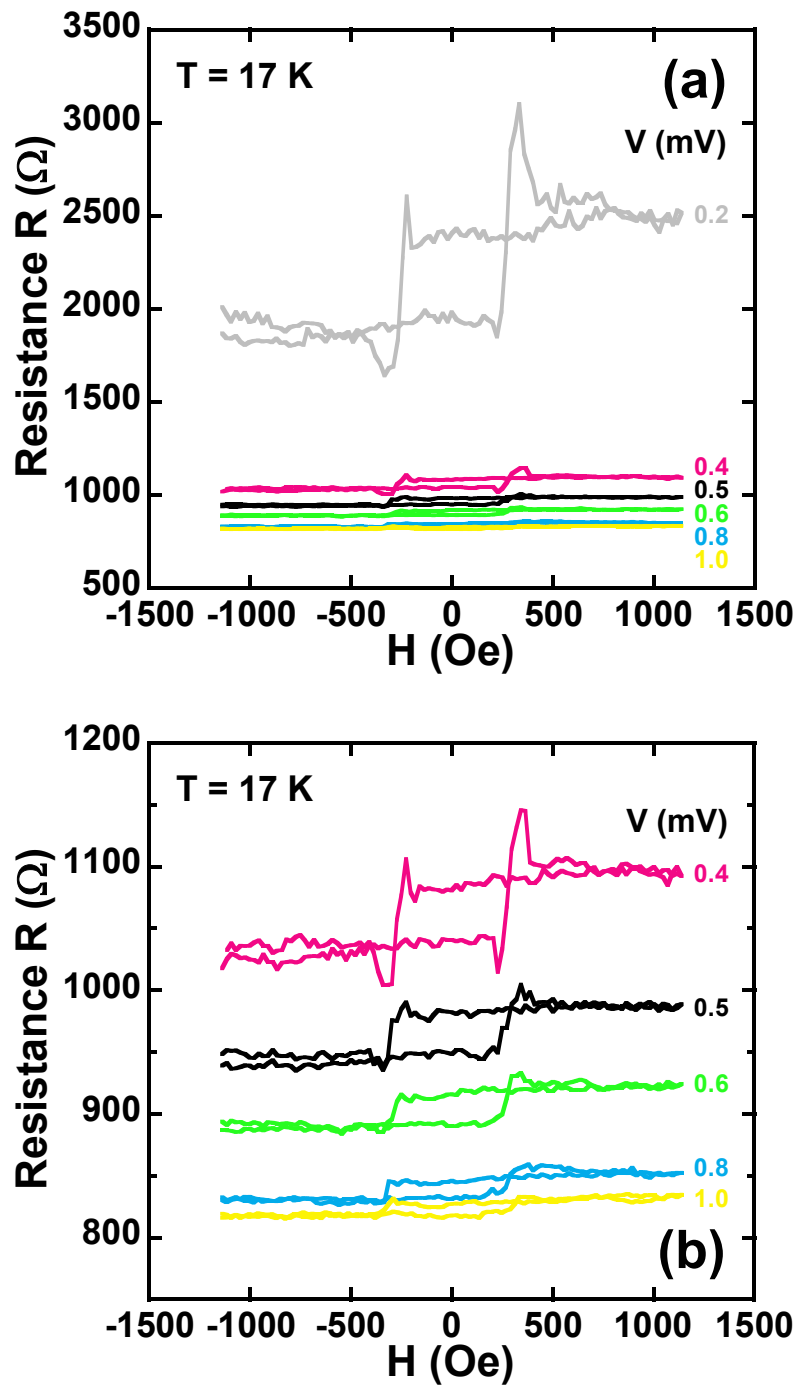


Fig. 4.8. Magnetoresistance characteristics of planar-type Ni-Ni oxide-Ni ferromagnetic tunnel junction at 16 K. Magnetoresistance curves with (a) lower bias voltages and (b) higher bias voltages.

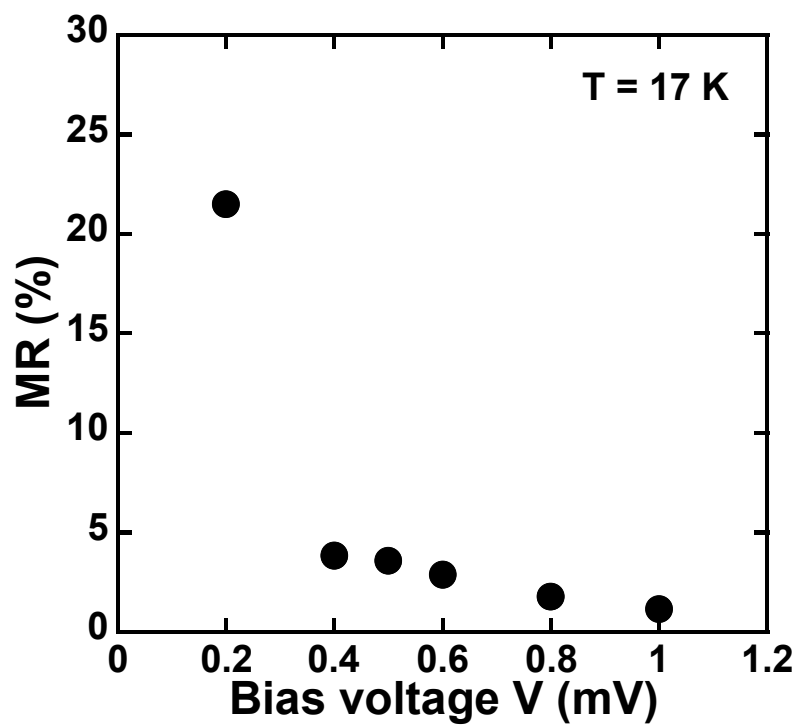


Fig. 4.9. MR ratio as a function of applied bias voltage in the planar-type Ni-Ni oxide-Ni ferromagnetic tunnel junction at 16 K.

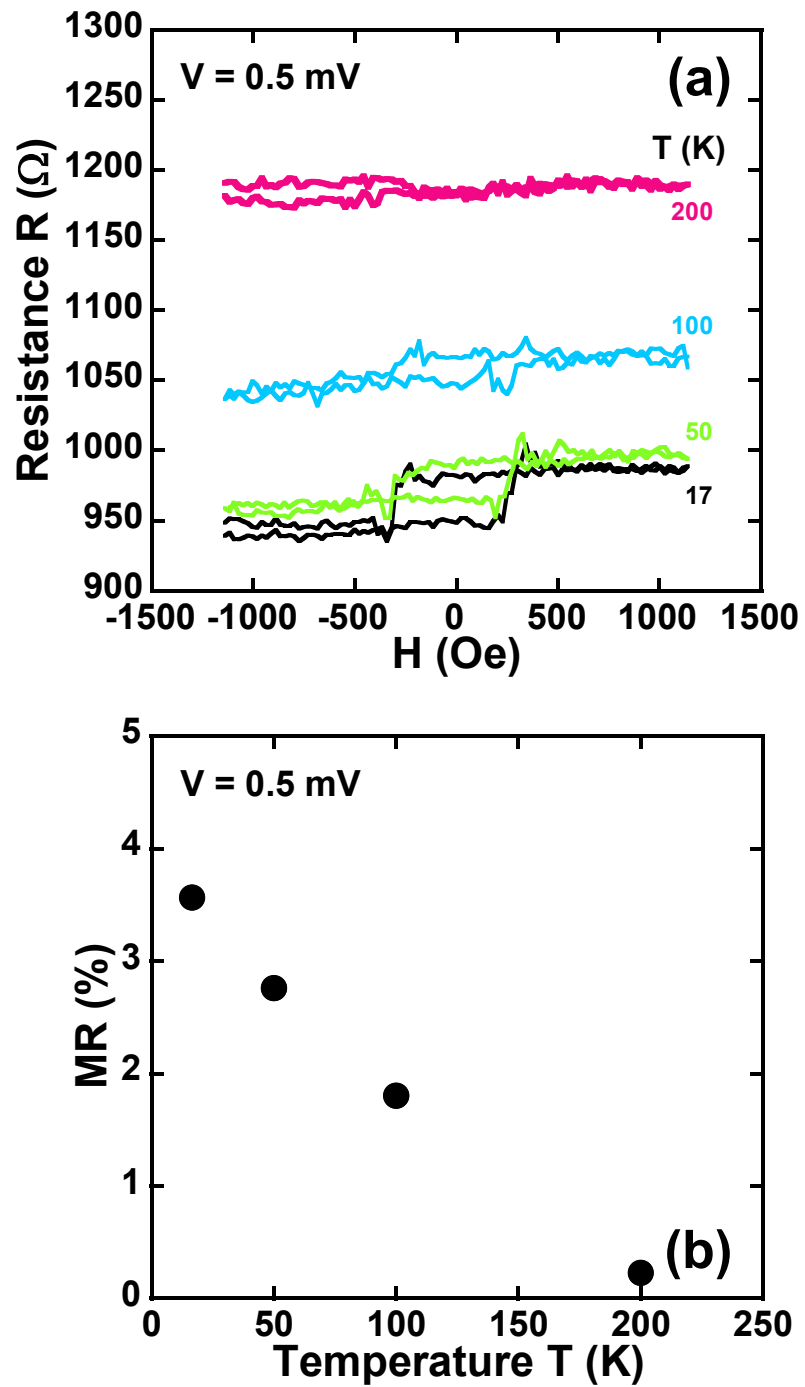


Fig. 4.10. Magneto-resistance characteristics of planar-type Ni-Ni oxide-Ni ferromagnetic tunnel junction at 0.5 mV. Temperature dependence on (a) MR curves and (b) MR ratio.

## **4.3.2 Channel Constriction Using Photolithography**

### ***4.3.2.1 Devices with Constricted Channel Width of 500 nm***

Figure 4.11(a) shows a scanning electron microscopy (SEM) of Ni asymmetrical channel patterned by photolithography. Figure 4.11(b) exhibits an atomic force microscopy (AFM) image of planar-type Ni-Ni oxide-Ni ferromagnetic tunnel junction fabricated by SPM local oxidation technique. Figure 4.12(a) shows the magnetoresistance (MR) curves at 17 K. Magnetic field is applied parallel to the channel, as shown in Fig. 4.11(a). The applied bias voltage is changed ranging from 0.17 to 0.4 mV. The MR curves with higher bias voltages are shown in Fig. 4.12(b). The MR characteristics of the planar-type Ni-Ni oxide-Ni ferromagnetic tunnel junction were decreased with increasing the applied bias voltage.

Figure 4.13 exhibits MR ratio as a function of the bias voltage. With decreasing the bias voltage from 0.4 to 0.17 mV, the MR ratio increases from 6 % to 29 %. The MR ratio of 29 % was obtained at 0.17 mV. Moreover, the MR curves of this device also show the minor loop behavior, which may be due to higher coercive field is larger than applied magnetic field or the existence of the anisotropic exchange interaction between Ni channel and Ni oxide barrier formed by SPM local oxidation [16, 17].

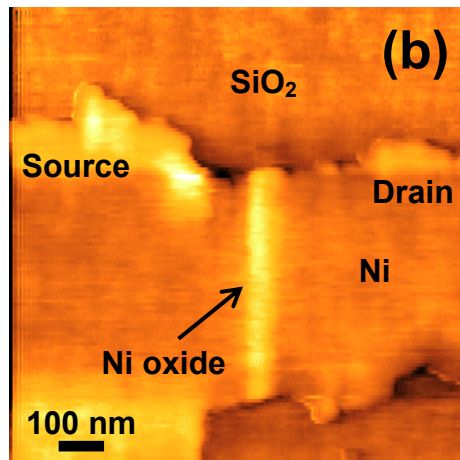
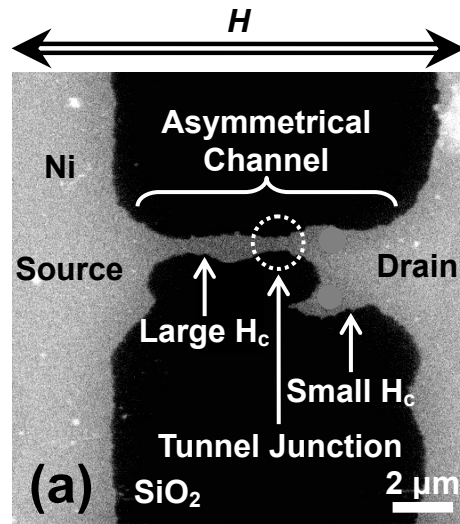


Fig. 4.11. (a) The SEM image of Ni asymmetrical channel patterned by photolithography. (b) The AFM image of planar-type Ni-Ni oxide-Ni ferromagnetic tunnel junction fabricated by SPM local oxidation technique.



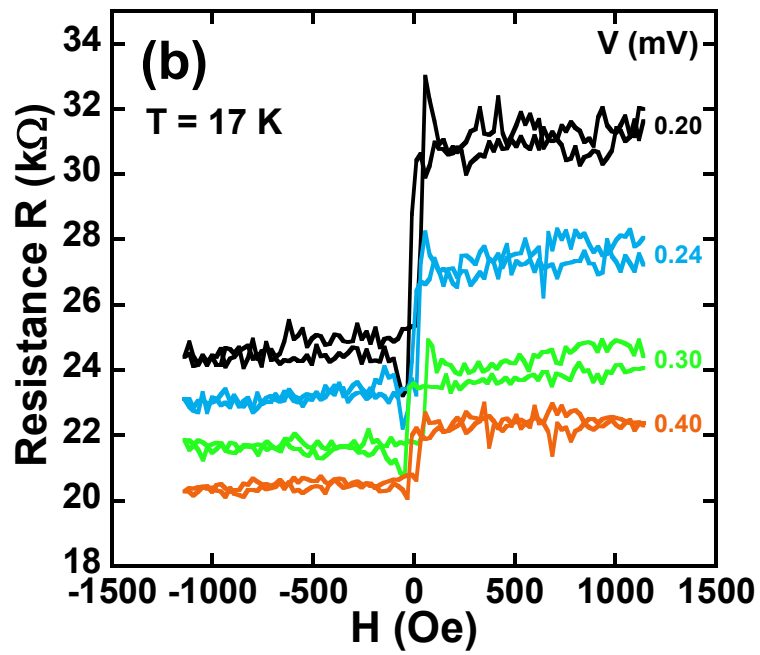
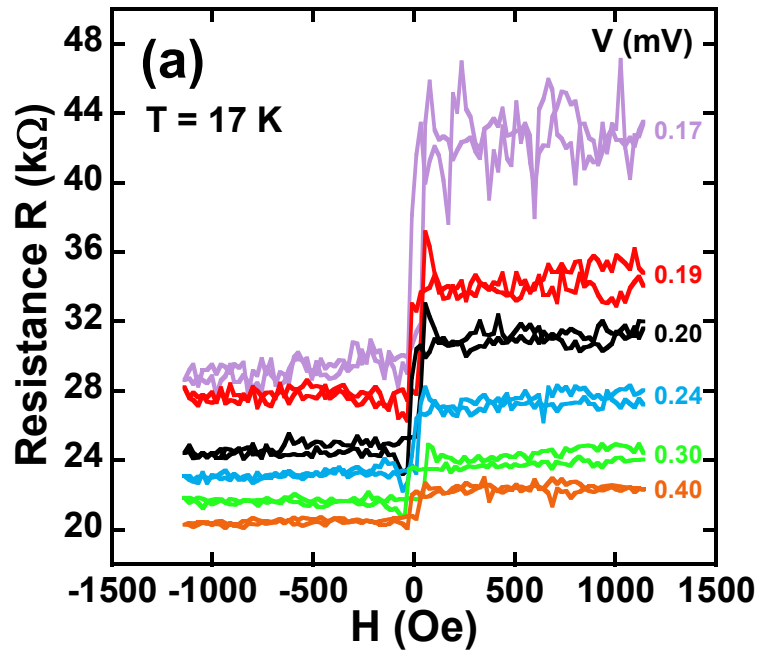


Fig. 4.12. Magnetoresistance characteristics of planar-type Ni-Ni oxide-Ni ferromagnetic tunnel junction at 17 K. Magnetoresistance curves with (a) lower bias voltages and (b) higher bias voltages.

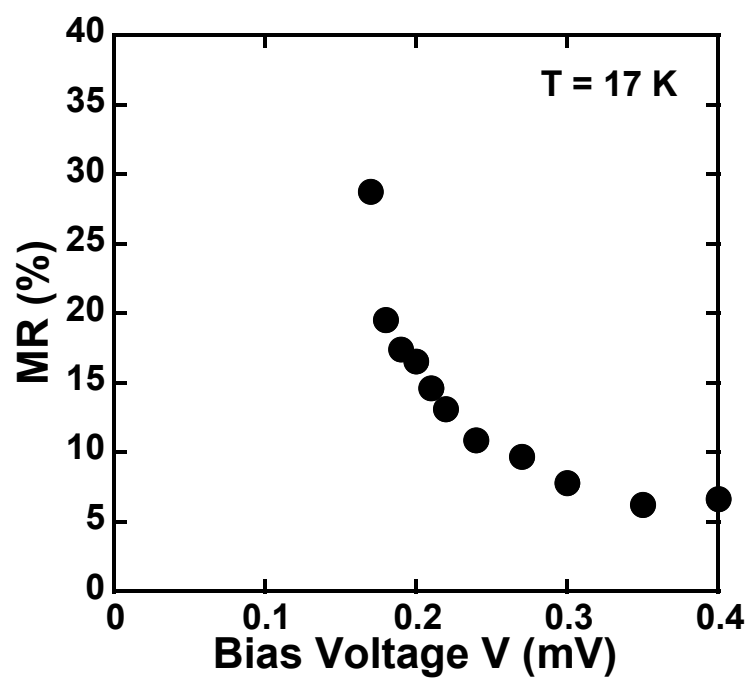


Fig. 4.13. MR ratio as a function of applied bias voltage in the planar-type Ni-Ni oxide-Ni ferromagnetic tunnel junction at 17 K.

#### ***4.3.2.2 Devices with Constricted Channel Width of 120 nm***

Figure 4.14(a) shows scanning electron microscopy (SEM) image of asymmetrical Ni channel. An atomic force microscopy (AFM) image of planar-type Ni-Ni oxide-Ni ferromagnetic tunnel junction is shown in Fig. 4.14(b). In this device, width of Ni channel of 120 nm is narrowest in planar-type Ni-Ni oxide-Ni ferromagnetic tunnel junctions.

Figure 4.15(a) exhibits the magnetoresistance (MR) curves with the bias voltage from 0.1 mV to 0.29 mV at 17 K. The MR curves with higher bias voltages are also shown in Fig. 4.15(b). The MR curves also show the typical shape of minor loop behavior. Figure 4.16 shows the MR ratio versus applied bias voltage at 17 K. The MR ratio of approximately 180 % was obtained at 0.1 mV. With increasing the bias voltage, the MR ratio quickly decreases from 180 % to 6.8 %, and shows strong dependence on the bias voltage. As mentioned above, the maximum MR ratio of 180 % at 17 K is larger than the predicted value of Ni-Ni oxide-Ni ferromagnetic tunnel junction by Julliere equation [6]. Furthermore, the MR ratio strongly depends on the applied bias voltage with the range of 0.1 mV is enough smaller than magnon and phonon excitations. Therefore, strong dependence of MR on the bias voltage in Fig. 4.16 may be caused by the localized trap states [13] in NiO barriers formed by SPM local oxidation, which suffer from imperfections of the oxide. As seen in Fig. 4.15(a), resistance fluctuations at lower bias voltage suggest the barrier imperfections such as nonstoichiometric phases and defects of the oxide. In addition, these high MR ratios may be due to the single-electron charging effect in the junctions [14] and/or the ballistic magnetoresistance effect from strongly constricted channels [15].

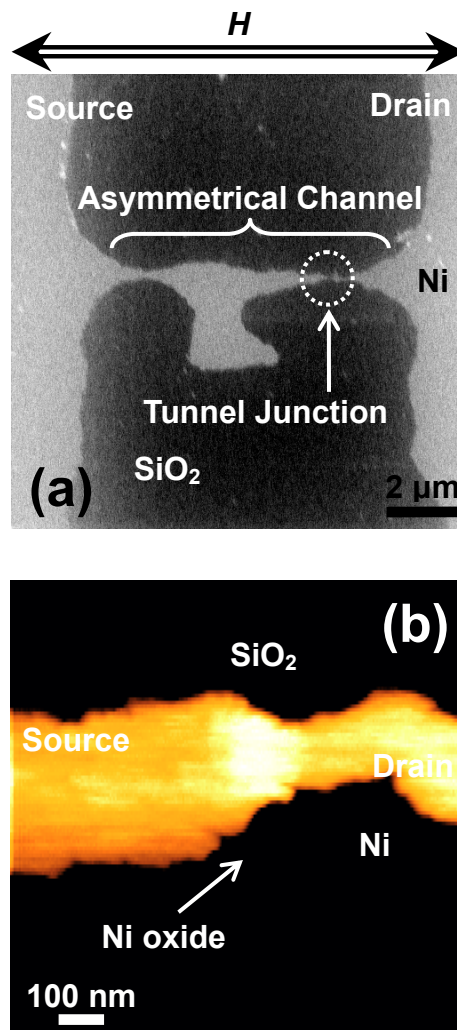


Fig. 4.14. MR ratio as a function of applied bias voltage in the planar-type Ni-Ni oxide-Ni ferromagnetic tunnel junction at 16 K.

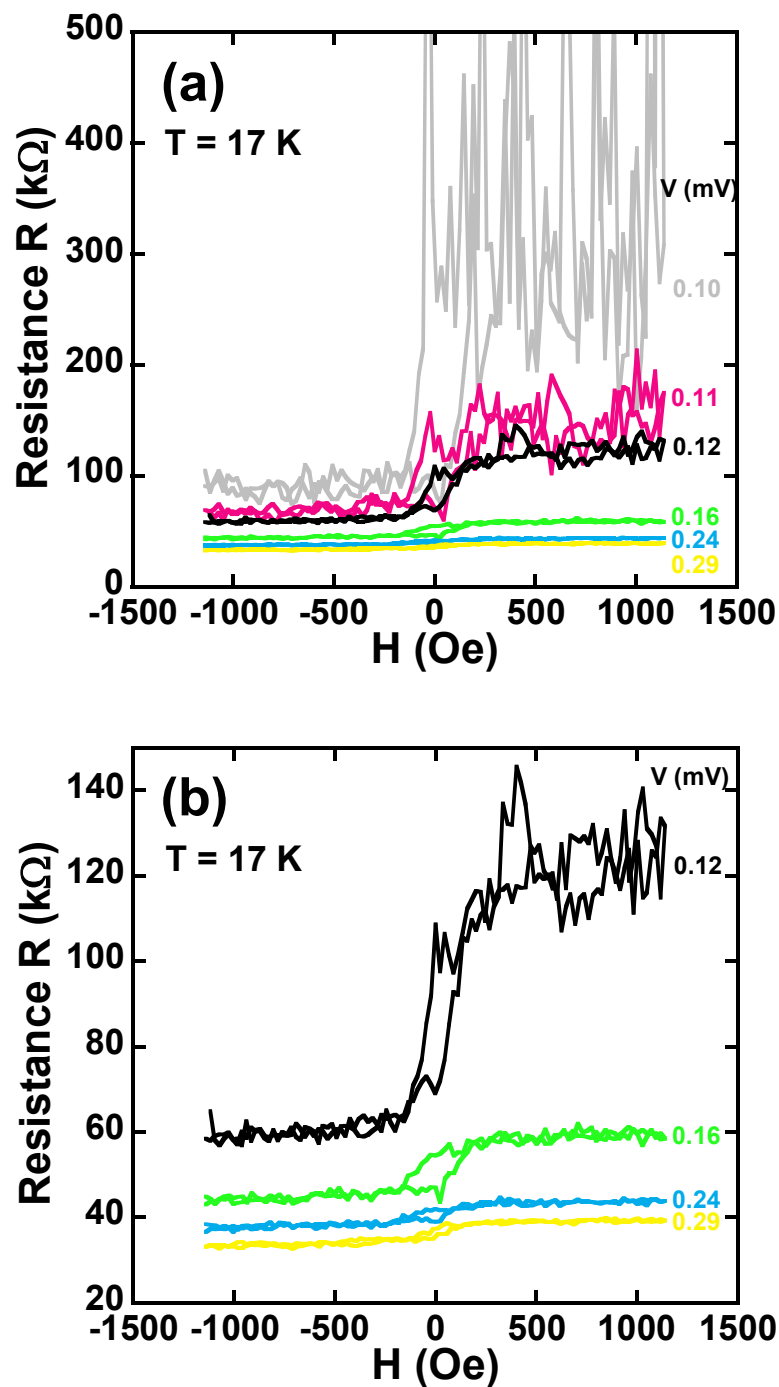


Fig. 4.15. Magnetoresistance characteristics of planar-type Ni-Ni oxide-Ni ferromagnetic tunnel junction at 17 K. Magnetoresistance curves with (a) lower bias voltages and (b) higher bias voltages.

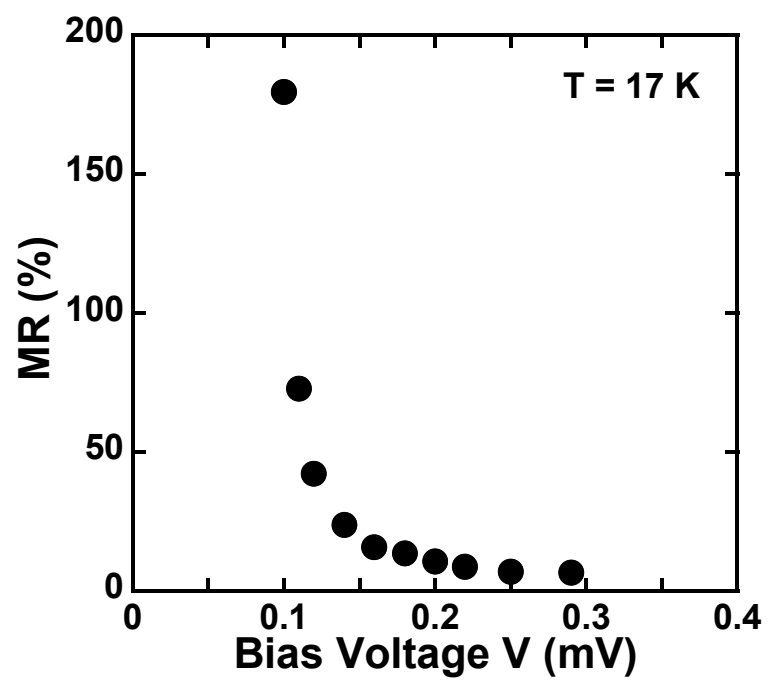


Fig. 4.16. MR ratio as a function of applied bias voltage in the planar-type Ni-Ni oxide-Ni ferromagnetic tunnel junction at 17 K.

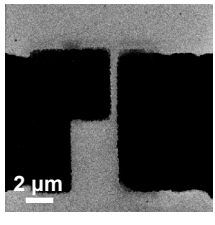
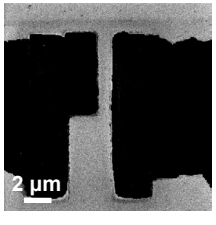
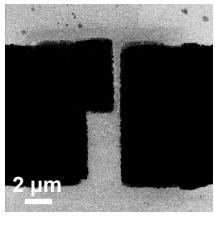
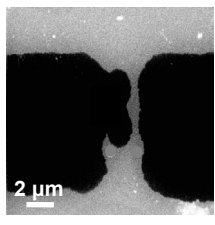
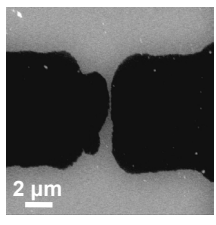
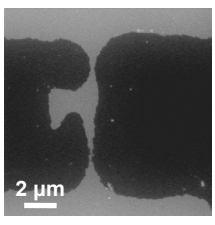
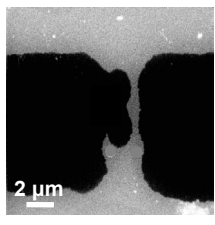
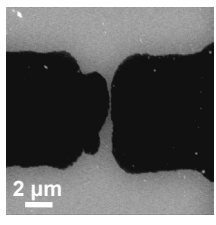
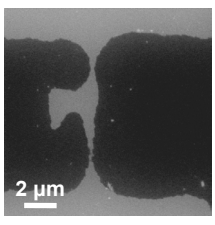
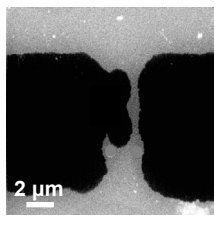
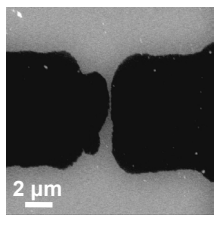
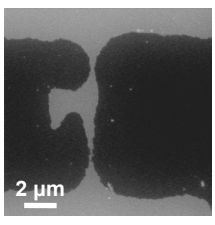
## 4.4 Comparison of Constriction Methods

Table 4.2 shows the scanning electron microscopy (SEM) images of the Ni channel patterned by focused ion beam (FIB) and photolithography and aspect ratio of drain side channel. Figure 4.17 shows comparison of typical magnetoresistance (MR) curves with various planar-type Ni-Ni oxide-Ni ferromagnetic tunnel junctions at 17 K. In the range of aspect ratio of 2, switching field of the devices constricted by FIB is larger than that of the devices constricted by photolithography.

The switching fields as a function of the aspect ratio are shown in Fig. 4.18(a). With increasing the aspect ratio of drain side channel, switching field increases in the devices constricted by photolithography. On the other hand, the switching field of the devices constricted by FIB is less dependent on the aspect ratio of drain side channel. These results suggest that increasing of damage and roughness of Ni channel may be induced by FIB process.

Figure 4.18(b) exhibits the MR ratio versus applied bias voltage in the devices constricted by FIB and photolithography. The high MR ratio and strongly dependence are obtained from both of the devices constricted by FIB and photolithography. This result implies that these MR characteristics are less dependent on constriction method, which is caused by fabrication of Ni oxide barriers formed by SPM local oxidation. As mentioned above, strong dependence of MR on the bias voltage may be caused by the localized trap states [13] in NiO barriers formed by SPM local oxidation, which suffer from imperfections of the oxide. In addition, these high MR ratios may be due to the single-electron charging in the junctions [14] and/or the ballistic MR effects from strongly constricted channels [15].

Table 4.2. SEM images and aspect ratio of Ni constricted channels.

Constriction Method	FIB	SEM Image			
		Aspect Ratio	1.6	1.9	2.1
		SEM Image			
	Photolithography	SEM Image			
		Aspect Ratio	1.3	3.5	12
		SEM Image			

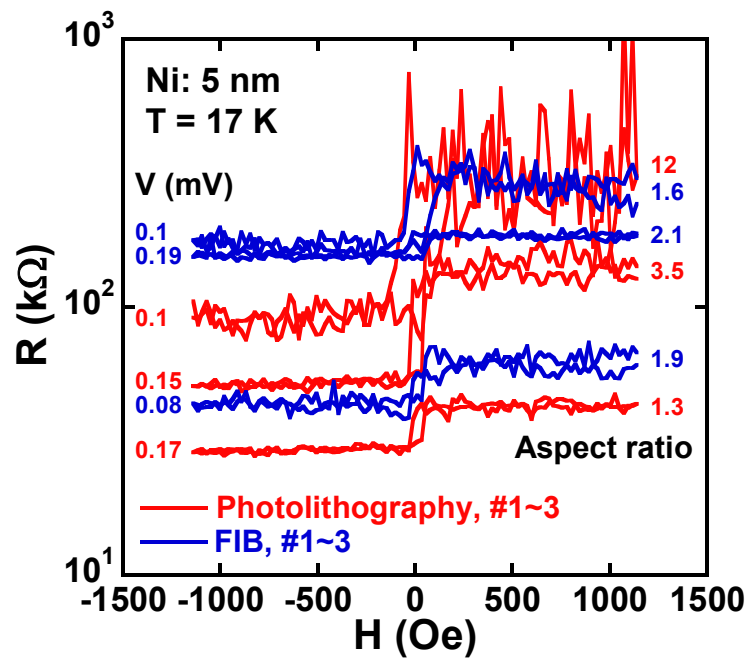


Fig. 4.17. Comparison of MR curves with various planar-type Ni-Ni oxide-Ni ferromagnetic tunnel junctions.



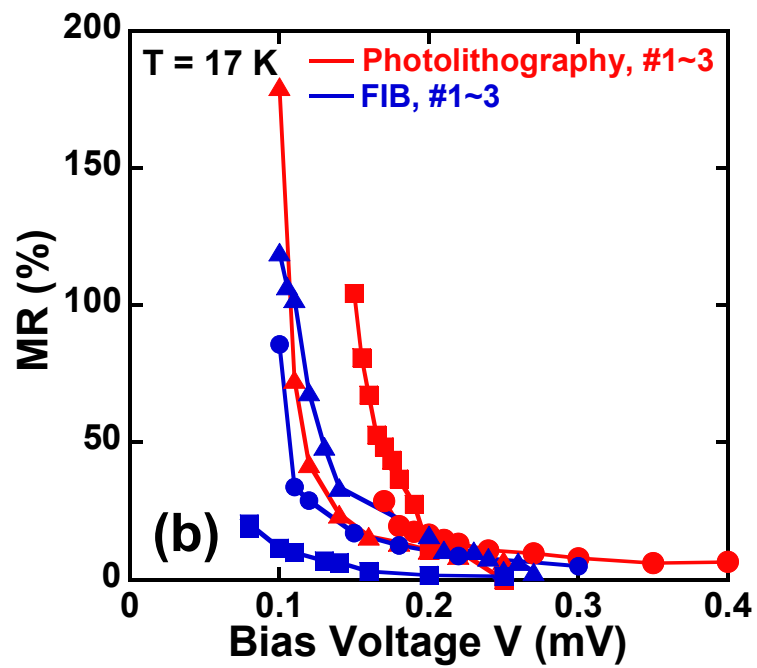
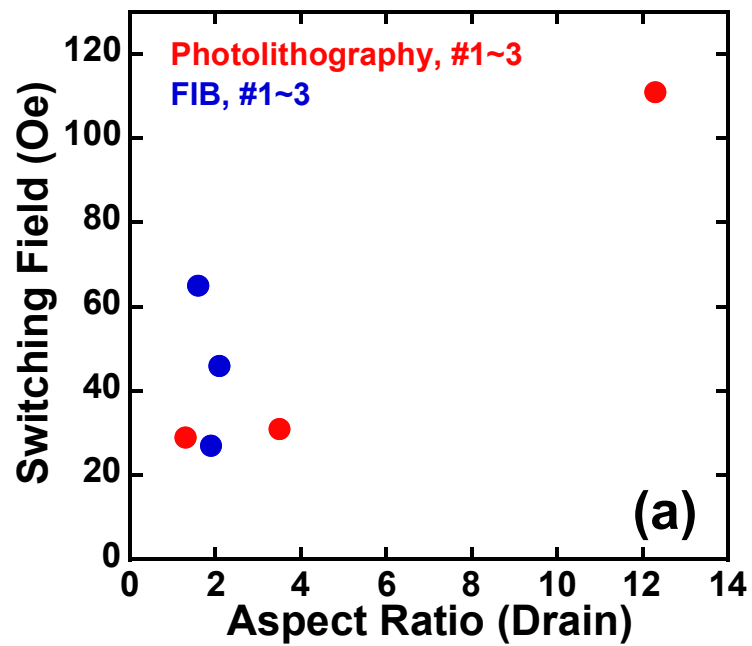


Fig. 4.18. (a) Relation between switching field and aspect ratio of drain side channel. (b) Dependence of MR ratio on applied bias voltage in the planar-type Ni-Ni oxide-Ni ferromagnetic tunnel junctions at 17 K.

## 4.5 Summary

We have investigated simple and easy techniques for the fabrication of planar-type ferromagnetic tunnel junctions. Planar-type Ni-Ni oxide-Ni ferromagnetic tunnel junctions were fabricated by scanning probe microscopy (SPM) local oxidation technique. For the fabrication of magnetoresistance (MR) difference across the junction, the Ni channel was asymmetrically patterned by focused ion beam (FIB) lithography or photolithography, in order to induce magnetic shape anisotropy.

The magnetoresistance (MR) properties of planar-type Ni-Ni oxide-Ni ferromagnetic tunnel junctions constricted by FIB lithography were clearly observed by applying a magnetic field. MR ratio exhibited above 100 % at 16 K and decreased with increasing the bias voltage and measurement temperature. Planar-type Ni-Ni oxide-Ni ferromagnetic tunnel junctions patterned by photolithography also shows high MR ratio of 180 % at 17 K. These high MR ratios may due to the single-electron charging effects in the junctions and/or the ballistic magnetoresistance effects from strongly constricted channels. The results strongly suggest that planar-type ferromagnetic tunnel junctions show the possibilities for nanoscale magnetoresistive devices.

## **Chapter 5**

# **Stepwise Feedback-Controlled Electromigration for Fabrication of Planar-Type Ni-Vacuum-Ni Ferromagnetic Tunnel Junctions**

### **5.1 Introduction**

Magnetoresistive effects in nanometer-scale ferromagnetic tunnel junctions are of considerable technological and scientific interest. For the fabrication of these nanostructures, electrodes are needed with a separation of typically 1 nm. In recent years, although some creative methods have been developed to fabricate such structures, electromigration (EM) scheme has been used as a simple fabrication technique for closely spaced electrodes [1-4]. EM in metal nanowires is considered to be the directed migration of metal atoms caused by a large current density. At high current densities, momentum transfer from the electrons to the metal atoms leads to drifts of the atoms, in the direction of the electron flow. Finally, the metal nanowires fail as a result of a gap formation. Although this approach is particularly simple because it is achieved by only passing a current through a metal nanowire, the typical procedure induces an abrupt break that yields a nanogap with uncontrollably high tunnel resistance [1, 5-7]. It is considered that the fabrication of highly reproducible nanogaps using a single voltage ramp is difficult because the current and temperature (Joule heating) during the formation of nanogap junctions are both changing rapidly [1]. Hence, several studies have worked on feedback-controlled electromigration (FCE) mechanisms, based on resistance monitoring of nanowires, in order to control rapid electromigration and create smaller nanogaps. The FCE process can be used to fabricate devices with resistance

ranging from a metallic regime through a few-atom regime characterized by quantum of conductance plateaus into a tunneling regime once the gap is formed [8-10]. Researchers have also inspected using transmission electron microscopy (TEM) to study the dynamic of the nanogap formation during the electromigration [11-13].

In order to realize the stable EM, we employ a stepwise approach, based on FCE mechanisms, for the control of the resistance of metal nanowires and call this procedure “stepwise feedback-controlled electromigration (SFCE)”. This technique is able to avoid the thermal instability due to a large current passing through the metal nanowire seriously degrades the reproducibility of the procedure and often results in catastrophic breaks with nanogaps greater than 10 nm. In this chapter, we report the planar-type ferromagnetic tunnel junctions with vacuum tunnel barrier formed by the SFCE technique. Electrical and magnetoresistive properties of planar-type Ni-Vacuum-Ni ferromagnetic tunnel junctions are also investigated.

## 5.2 Micromagnetic Simulation

The goal of the OOMMF project in ITL/NIST is to develop a portable, extensible public domain micromagnetic program and associated tools. This code will form a completely functional micromagnetics package, but will also have a well documented, flexible programmer's interface so that people developing new code can swap their own code in and out as desired.

In order to allow a programmer not familiar with the code as a whole to add modifications and new functionality, we feel that an object oriented approach is critical, and have settled on C++ as a good compromise with respect to availability, functionality, and portability. In order to allow the code to run on a wide variety of systems, we are writing the interface and glue code in Tcl/Tk. This enables our code to operate across a wide range of Unix platforms, Windows NT, and Windows 95/98.

The code may be modified at 3 distinct levels. At the top level, individual programs interact via well defined protocols across network sockets. One may connect these modules together in various ways from the user interface, and new modules speaking the same protocol can be transparently added. The second level of modification is at the Tcl/Tk script level. Some modules allow Tcl/Tk script to be imported and executed at run time, and the top level scripts are relatively easy to modify or replace. At the lowest level, the C++ source is provided.

We designed an asymmetrical-butterfly shape with nanogap as schematically illustrated in Fig. 5.1. In order to induce magnetic shape anisotropy, asymmetrical geometry structure is employed to the devices. The width and length of source and drain electrode is 400 nm×1300 nm and 600 nm×1440 nm, respectively. Table 5.1 exhibits parameters of the micro magnetic simulations. The saturated magnetization used in the

calculation  $M_s$  is  $480 \times 10^3$  A/m, the exchange couplings  $A_x$  and damping coefficient  $\alpha$  are  $9 \times 10^{-11}$  J/m and 0.5, respectively. We have assumed the anisotropy energy  $K$  to be zero as most of the patterned samples made by lift-off technique are polycrystalline with a very small crystalline anisotropy; we can see more clearly the effect of shape anisotropy. The cell size of the simulations has chosen to be 5 nm.

The magnetic calculations were carried out using Object Oriented MicroMagnetic Framework (OOMMF) software [14] based on the Landau-Lifschitz-Gilbert equation as follows:

$$\frac{\partial M}{\partial t} = \gamma \left( M \times H_{eff} \right) + \frac{\alpha}{M_s} M \times \frac{\partial M}{\partial t}, \quad (5.1)$$

where  $\gamma$  is gyromagnetic constant,  $\alpha$  is damping constant,  $H_{eff}$  is effective field, and  $M_s$  is saturation magnetization. Effective field  $H_{eff}$  is total energy including exchange interaction energy, anisotropy energy, demagnetizing energy and external magnetic field energy in the cell. OOMMF software has been useful to predict and verify experimental results of some of these nanomagnets. In order to investigate the influence of the shape of nanoelements and the magnetic material employed on the magnetization reversal process, here using OOMMF code we present the micromagnetic simulation of a new geometrical structure: asymmetrical butterfly shape with 10 nm gap. The calculation procedure was as follows. First, a magnetic field of 1000 Oe was applied to  $y$  axis from demagnetization state. Then, the magnetic field is varied from 1000 to -1000 Oe and reverse.

Figure 5.2 shows the  $H$ - $M$  hysteresis loop obtained by the simulation and the magnetization configurations for Ni nanogap with 30 nm thickness. Stable anti-parallel configuration between source and drain electrode can be observed from -140 to -340 Oe and 140 to 340 Oe. Spin configurations of Ni nanogap also exhibit sharp reverse of spin

configuration, as shown in Table 5.2. This result implies that the asymmetrical butterfly shape can be applied to planar-type ferromagnetic tunnel junctions.

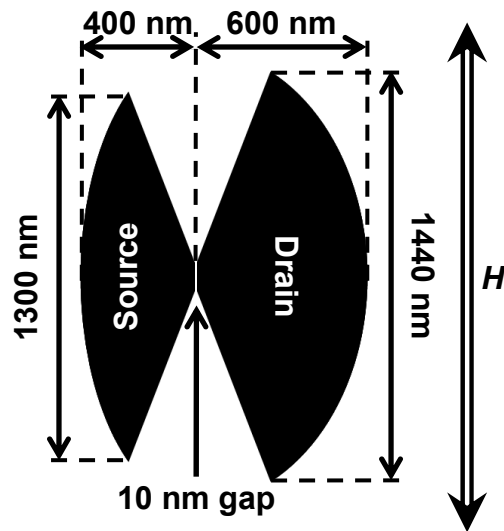


Fig. 5.1. The schematic of Ni nanogap for simulation.

Table 5.1. The basic parameters used for the simulations.

Material Name	Nickel
Saturation Magnetization (Ms)	$480 \times 10^3$ A/m
Exchange Stiffness constant (A)	$9 \times 10^{-12}$ J/m
Anisotropic Constant (Ku)	0 J/m <sup>3</sup>
Damping Constant ( $\alpha$ )	0.5
Cell Size	5 nm
Initial Magnetization	random
Sweep step of Field (H)	20 Oe
Thickness	30 nm



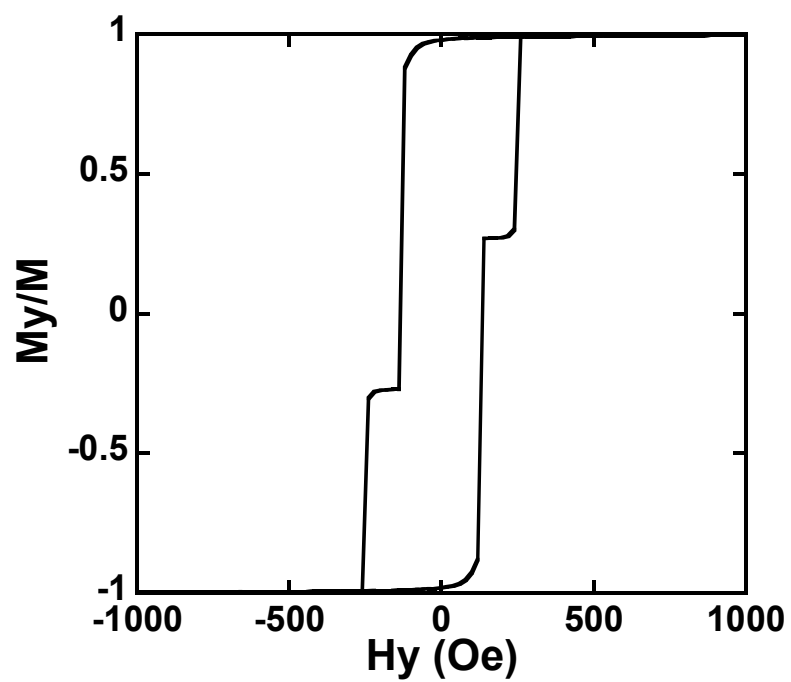
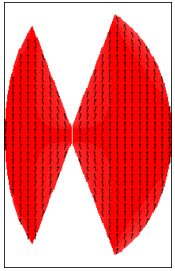
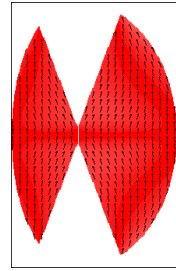
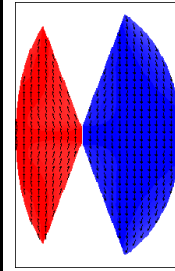
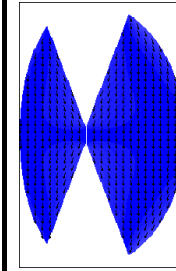
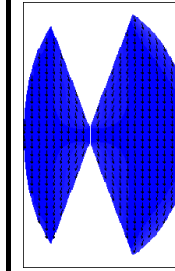


Fig. 5.2. The schematic of Ni nanogap for simulation.

Table 5.2. Spin configuration for Ni nanogap.

H	500 Oe	0 Oe	-140 Oe	-360 Oe	-500 Oe
Spin Configuration					

## 5.3 Planar-Type Ni-Vacuum-Ni Ferromagnetic Tunnel Junctions Fabricated by SFCE Technique

### 5.3.1 Asymmetrical Butterfly-Shape Electrodes

Figure 5.3 shows the schematic of nanogap formation using stepwise feedback-controlled electromigration (SFCE). The SFCE experiments were performed on 100 nm thick, thermally grown SiO<sub>2</sub> surface on Si substrates. First, 25 nm thick Au contact pads were fabricated upon 5 nm Ti layer by electron-beam (EB) lithography and EB evaporation. Then, 15 nm thick, Ni nanoconstrictions connected asymmetrical butterfly-shape electrode with the width of ~100 nm were formed by the same procedure in the gap between the Au contact pads. The asymmetrical butterfly shape source-drain electrodes cause the stable orientation of magnetization at parallel and anti-parallel states. The scanning electron microscopy (SEM) images of the nanoconstriction before and after performing the SFCE process are shown in Table 5.3. This observation clearly suggests that nanogap was formed at nanoconstriction by electromigration, which is induced by SFCE technique.

Current-voltage ( $I$ - $V$ ) characteristics measured after each SFCE step are shown in Fig. 5.4(a). The current decreases with progression the SFCE steps. In this device, the resistance of Ni nanoconstriction was initially 350  $\Omega$  and increased up to 183 k $\Omega$  by performing the SFCE method. Figure 5.4(b) shows the bias voltage dependence of the current and the derivative of the conductance after performing 3rd SFCE at 16 K. Since a peak in the inelastic electron tunneling spectrum (IETS) can be observed, the current is due to the electron tunneling between Ni electrodes through the nanogap. The  $I$ - $V$  characteristics at 16 K were fitted by Simmons model [15], and barrier height and thickness were estimated to be approximately 4 eV and <1 nm, respectively. Therefore,

this implies that the nanogap formed by SFCE technique act as vacuum tunnel barrier of planar-type ferromagnetic tunnel junctions.

Figure 5.5(a) shows low temperature magnetoresistance (MR) properties of the planar-type ferromagnetic tunnel junctions fabricated by SFCE method. In order to eliminate the thermal excitation electrons, we measured the MR characteristics at 16 K. The vacuum barrier of the devices was formed by SFCE method as shown in Table 5.3, and the MR ratio of approximately 4 % was obtained at 16 K. The resistance increases gradually at about 500 Oe, and then sharply decreases to its initial value at  $\sim 1000$  Oe. Figure 5.5(b) exhibits MR ratio as a function of the bias voltage. The applied bias voltage is changed from 2 to 20 mV. With increasing the bias voltage, the MR ratio decreases from 4.5 % to 2 %.

The magnetization switching process was also studied by micromagnetic simulations using Object Oriented MicroMagnetic Framework (OOMMF) package on the geometry of the Ni electrodes placed in the gap between the Au contact pads (Fig. 5.6(a)). Figure 5.6(b) shows  $M-H$  properties of the geometry. The switching fields obtained from the theoretical results are 150 and 750 Oe. The difference of the calculated coercive fields is in good agreement with those of the experimental values. This implies that the coercivity of the Ni drain electrode is smaller than that of the Ni source electrode, because of magnetic shape anisotropy induce by the asymmetrical shape of the electrodes. Thus, the SFCE technique can easily fabricate planar-type ferromagnetic tunnel junctions with Ni-Vacuum-Ni nanogap system.

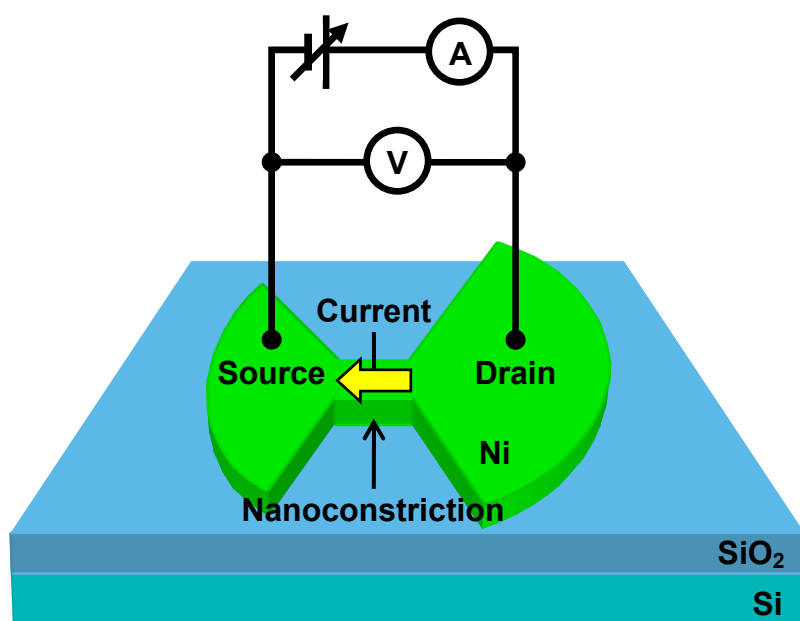
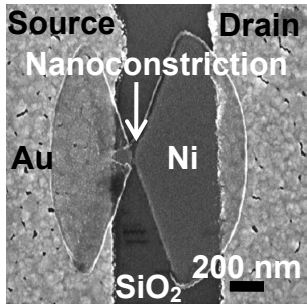
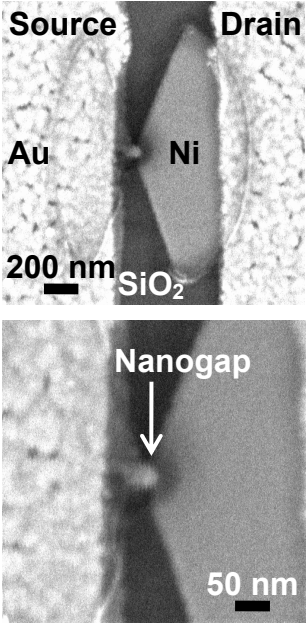


Fig. 5.3. Schematic of SFCE procedure. Nanoconstrictions with asymmetrical butterfly shape of Ni are fabricated on SiO<sub>2</sub>/Si substrates.

Table 5.3. The SEM images of Ni nanoconstriction connected asymmetrical butterfly-shape electrode before and after the SFCE procedure.

	Before Activation	After Activation
SEM Image		

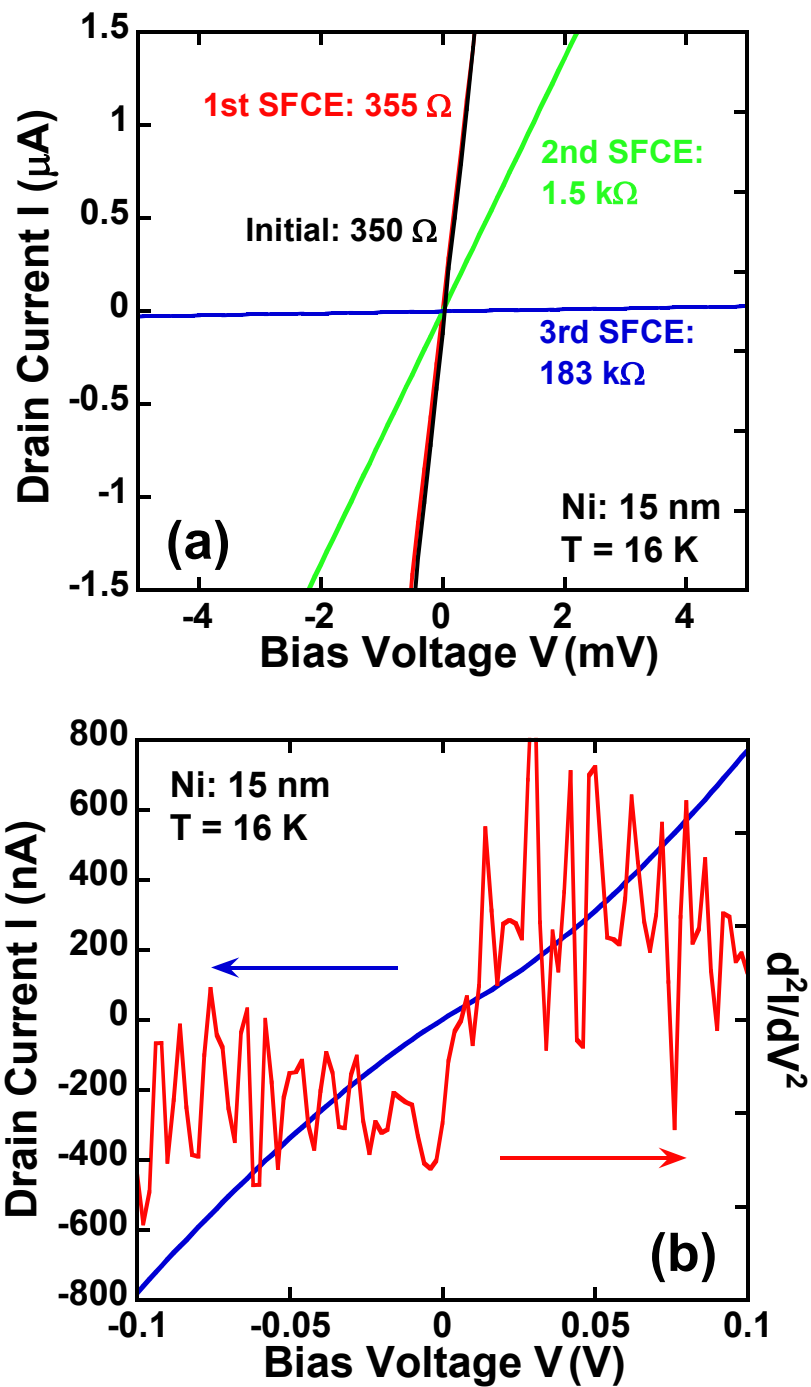


Fig. 5.4. (a) *I-V* characteristics of the nanogap during SFCE procedure. (b) Electrical properties after formation of the nanogap using SFCE method.

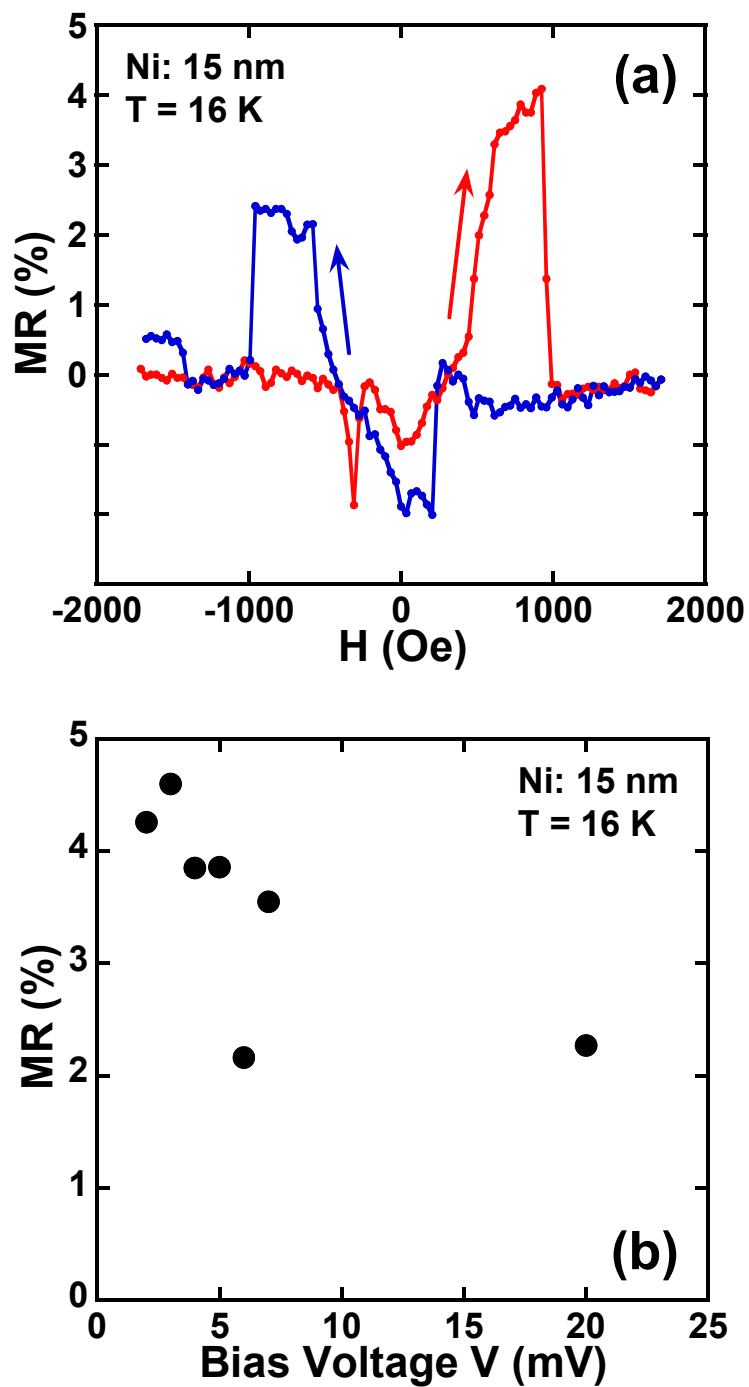


Fig. 5.5. (a) Magnetoresistance characteristics of planar-type Ni-Vacuum-Ni tunnel junction fabricated by SFCE. (b) MR ratio as a function of bias voltage.

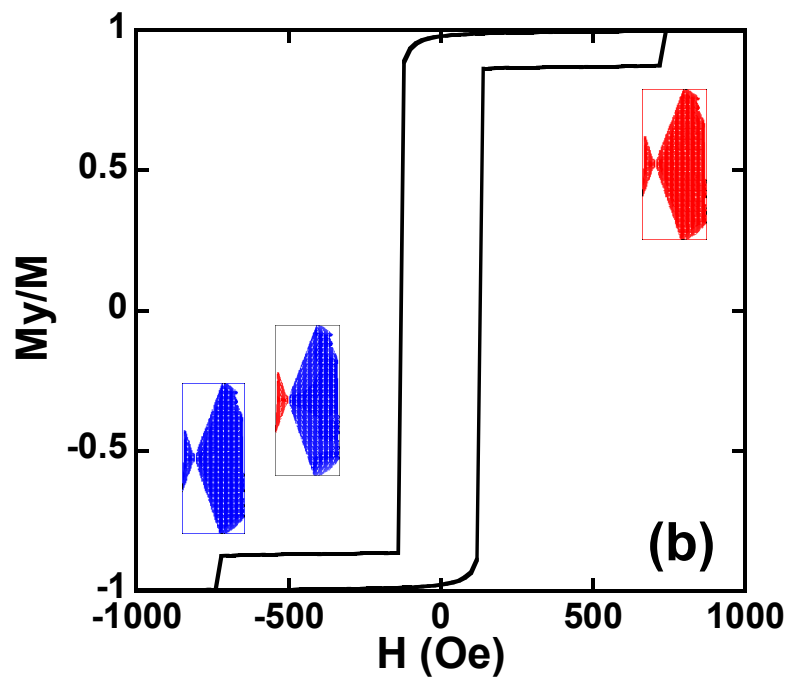
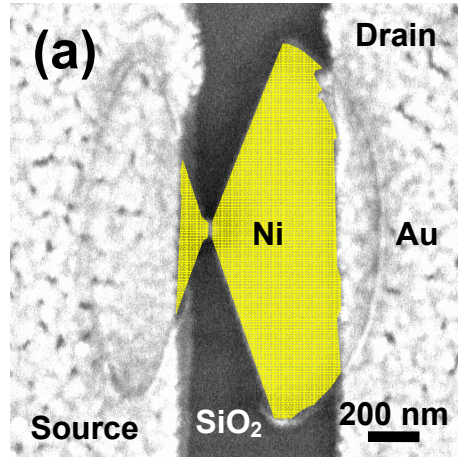


Fig. 5.6. (a) Geometry of Ni electrode placed in the gap between the Au contact pads. (b)  $M$ - $H$  properties of Ni electrode placed in the gap between the Au contact pads.

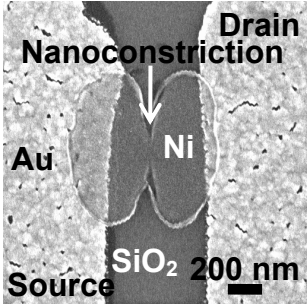
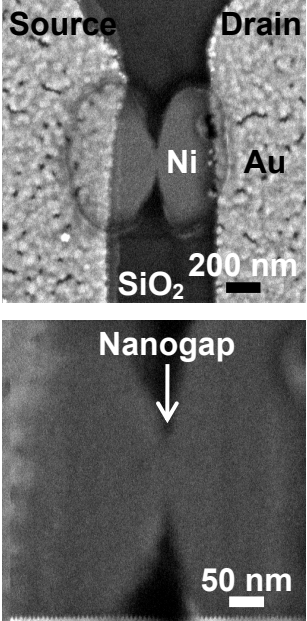


### 5.3.2 Asymmetrical Broad Bean-Shape Electrodes

Table 5.4 shows Ni nanoconstriction connected asymmetrical broad bean-shape electrode before and after performing the stepwise feedback-controlled electromigration (SFCE) method. This asymmetrical broad bean-shape electrode is also induced magnetic shape anisotropy [16]. Figure 5.7(a) exhibits current-voltage ( $I$ - $V$ ) characteristics measured after each SFCE step. Initial resistance of this device is  $280 \Omega$ , which increases to  $23 \text{ k}\Omega$  with progression the SFCE procedure. This result is similar to that of Ni nanoconstriction connected asymmetrical butterfly shape electrode. Therefore, the control of the resistance of the nanoconstriction using the SFCE technique is hardly affected by the shape of the electrode. The electrical properties at 16 K also show a peak in the inelastic electron tunneling spectrum (IETS), as shown in Fig. 5.7(b). This implies that the current is due to the electron tunneling between source and drain electrodes through the vacuum tunnel barrier formed by final SFCE procedure.

Magnetoresistance (MR) properties of the nanogap connected asymmetrical broad bean-shape electrode at 16 K, as shown in Fig. 5.8. The MR ratio of  $\sim 7 \%$  was obtained at 16 K. The resistance increases sharply around 300-400 Oe, and then rapidly decreases to its initial value at 1200-1500 Oe. The difference of coercivity field is induced by magnetic shape anisotropy of the asymmetrical shape of the Ni electrodes. Hence, one can easily fabricate the planar-type ferromagnetic Ni-Vacuum-Ni tunnel junctions using the SFCE technique.

Table 5.4. The SEM images of Ni nanoconstriction connected asymmetrical broad bean-shape electrode before and after the SFCE procedure.

	Before Activation	After Activation
SEM Image		

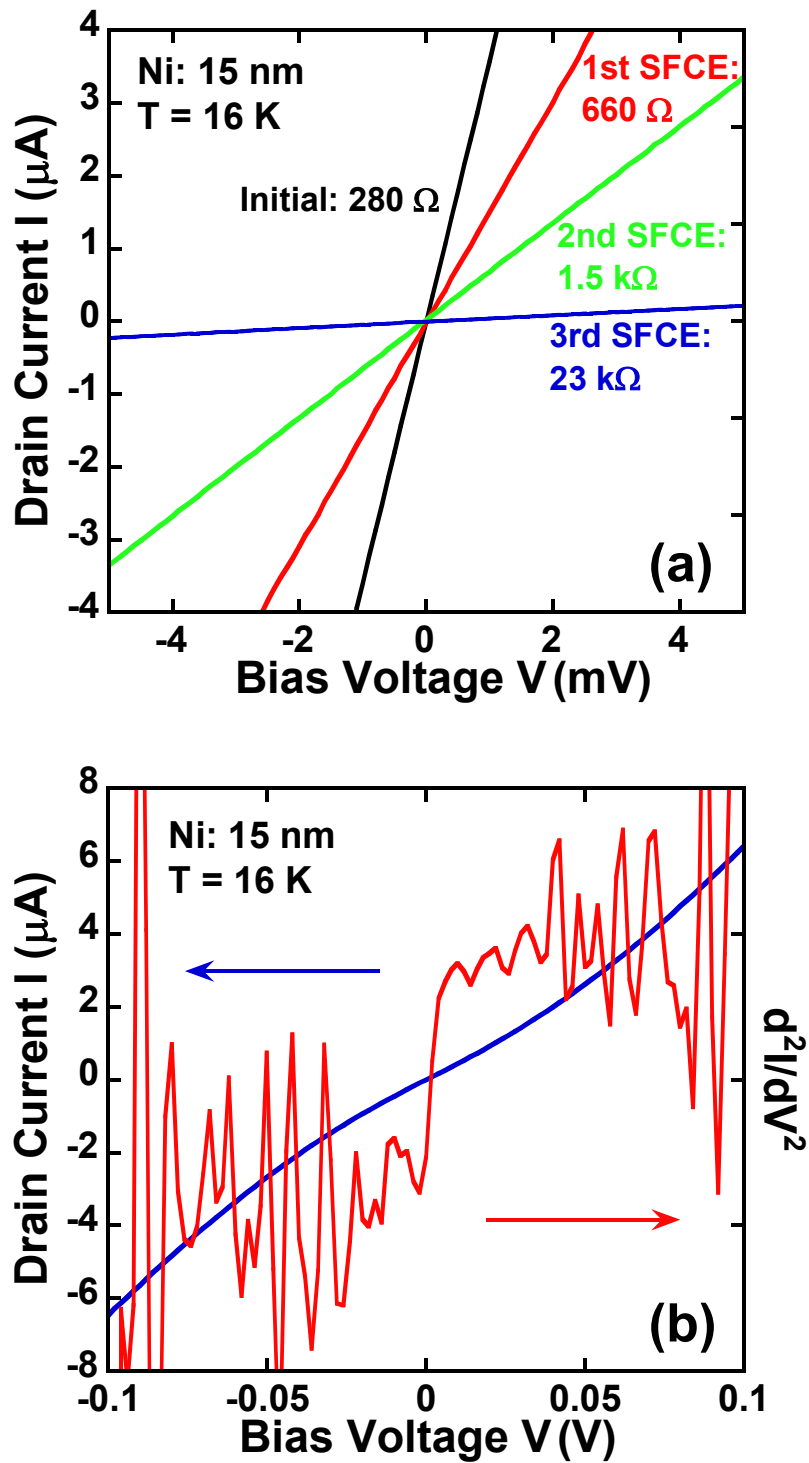


Fig. 5.7. (a)  $I$ - $V$  characteristics of the nanogap during SFCE procedure. (b) Electrical properties after formation of the nanogap using SFCE.

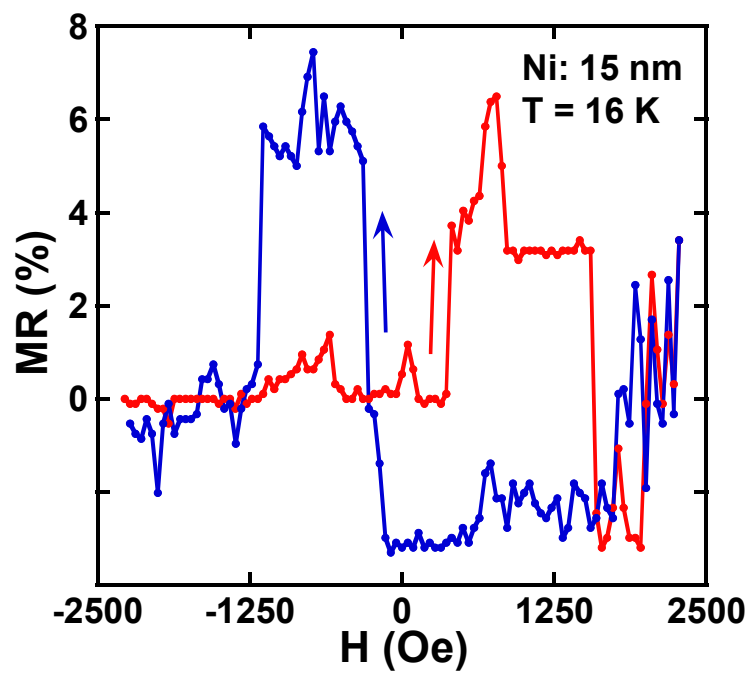


Fig. 5.8. Magnetoresistance characteristics of planar-type Ni-Vacuum-Ni tunnel junction fabricated by SFCE.

## 5.4 Summary

In conclusion, a simple method for the control of the resistance on nanoconstriction and fabrication of planar-type Ni-Vacuum-Ni ferromagnetic tunnel junctions, based on feedback-controlled electromigration, has been presented. The resistance of nanoconstriction after stepwise feedback-controlled electromigration (SFCE) procedure was adjusted to be in tunneling regime. After performing the SFCE procedure, the derivative conductance curve shows inelastic excitations in Ni-Vacuum-Ni tunnel junctions at 16 K. Furthermore, the junction also exhibits magnetoresistance (MR) properties. This suggests that the nanogaps fabricated by SFCE technique act as vacuum tunnel barrier. These results imply that this simple technique can simplify the fabrication of planar-type ferromagnetic tunnel junctions.

## **Chapter 6**

# **Formation of Planar-Type Ni-Vacuum-Ni Ferromagnetic Tunnel Junctions Using Field-Emission-Induced Electromigration**

### **6.1 Introduction**

Fabrication techniques of nanogaps using electromigration (EM) approaches have attracted considerable attention, because EM processes are simple and easy methods for the fabrication of nanogaps. We have proposed a unique method to produce nanogaps, field-emission-induced EM, in which we call this approach “activation” [1-4]. In the activation process, EM is caused by Fowler-Nordheim (F-N) field emission current passing through the nanogap. During the activation, bias voltages are applied to the nanogap with initial gap separation of a few tens of nanometers. Consequently, field emission current flow occurs through the gap and finally activates the metal atoms at the tip of source electrode. Activated metal atoms easily move towards the drain electrode, resulting in a decrease of the separation of the nanogap. Therefore, the tunnel resistance of the nanogap decreases after performing the activation. In other words, the tunnel resistance of the junction consisted of the nanogap is precisely controlled by varying the value of the preset current. In this chapter, magnetoresistance (MR) properties of planar-type Ni-Vacuum-Ni ferromagnetic tunnel junctions formed by the activation technique are investigated. In this tunnel junction system with vacuum barriers, spin-polarized electrons may be transported without physical interaction from insulating barrier materials.

## 6.2 Micromagnetic Simulation

For ferromagnetic Ni nanogaps, a configuration of source and drain electrodes must be designed to give them different magnetic shape anisotropies, so that they undergo magnetic reversal at different values of the applied magnetic field. In order to obtain the optimal shape in which antiparallel (AP) configuration of two magnetic moments is most stable, we have performed micromagnetic modeling of various geometries using the object oriented micromagnetic framework (OOMMF) software built on Landau-Lifshitz-Gilbert equation [5] and have had good success with an asymmetrical butterfly pattern represented in the Fig. 6.1. This structure is contracted 50 % from Fig. 5.1. In this pattern, width of source and drain electrodes is 200 nm and 300 nm, respectively. Length of the electrodes is almost the same, which are 650 nm and 720 nm. Since the source electrode has larger aspect ratio than that of the drain electrode, it is assumed that the coercive field of the source electrode is larger than that of the drain one.

Table 6.1 exhibits parameters of the micro magnetic simulations. The saturated magnetization used in the calculation  $M_s$  is  $480 \times 10^3$  A/m, the exchange couplings  $A_x$  and damping coefficient  $\alpha$  are  $9 \times 10^{-11}$  J/m and 0.5, respectively. We have assumed the anisotropy energy  $K$  to be zero as most of the patterned samples made by lift-off technique are polycrystalline with a very small crystalline anisotropy; we can see more clearly the effect of shape anisotropy. The cell size of the simulations has chosen to be 5 nm. First, a magnetic field of 1000 Oe was applied to  $y$  axis from demagnetization state. Then, the magnetic field is varied from 1000 to -1000 Oe and reverse.

Figure 6.2 shows the calculated hysteresis loop for 30 nm-thick Ni nanogap electrode with asymmetrical butterfly configuration. The gap width between a pair of

electrodes is assumed to be 10 nm in this calculation. The hysteresis curve draws plateau from -400 to -520 Oe and 400 to 520 Oe, suggesting that the magnetization direction of two electrodes can realize a stable AP alignment state. These results imply that spin configurations of Ni nanogap exhibit sharp reverse of spin configuration, as shown in Table 6.2.

Furthermore, another asymmetrical butterfly pattern was also calculated as shown in Fig. 6.3. In this pattern, width of source and drain electrodes is 400 nm and 600 nm, respectively. Length of the electrodes is almost the same, which are 1300 nm and 1440 nm. Since the source electrode has larger aspect ratio than that of the drain electrode, it is assumed that the coercive field of the source electrode is larger than that of the drain one. Table 6.3 shows parameters of the micro magnetic simulations, which is same parameters of Table 6.1.

Figure 6.4 shows the calculated  $M-H$  loop for 30 nm-thick Ni nanogap electrode of Fig. 6.3. The hysteresis curve draws clear plateau from -140 to -340 Oe and 140 to 340 Oe, suggesting that the magnetization direction of two electrodes can realize a stable AP alignment state. These results imply that spin configurations of Ni nanogap exhibit sharp reverse of spin configuration, as shown in Table 6.4.



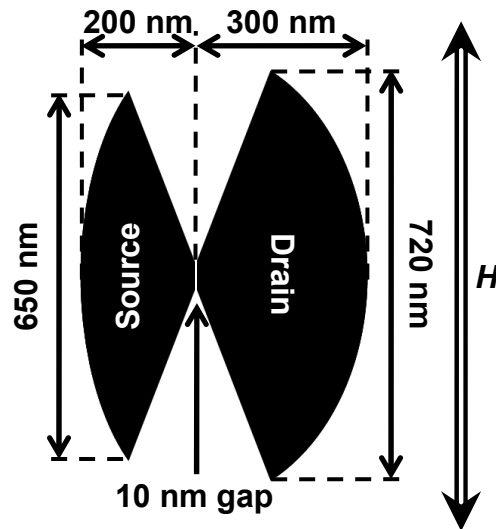


Fig. 6.1. The schematic of Ni nanogap for simulation.

Table 6.1. The basic parameters used for the simulations.

<b>Material Name</b>	<b>Nickel</b>
<b>Saturation Magnetization (Ms)</b>	<b><math>480 \times 10^3</math> A/m</b>
<b>Exchange Stiffness constant (A)</b>	<b><math>9 \times 10^{-12}</math> J/m</b>
<b>Anisotropic Constant (Ku)</b>	<b>0 J/m<sup>3</sup></b>
<b>Damping Constant (<math>\alpha</math>)</b>	<b>0.5</b>
<b>Cell Size</b>	<b>5 nm</b>
<b>Initial Magnetization</b>	<b>random</b>
<b>Sweep step of Field (H)</b>	<b>20 Oe</b>
<b>Thickness</b>	<b>30 nm</b>

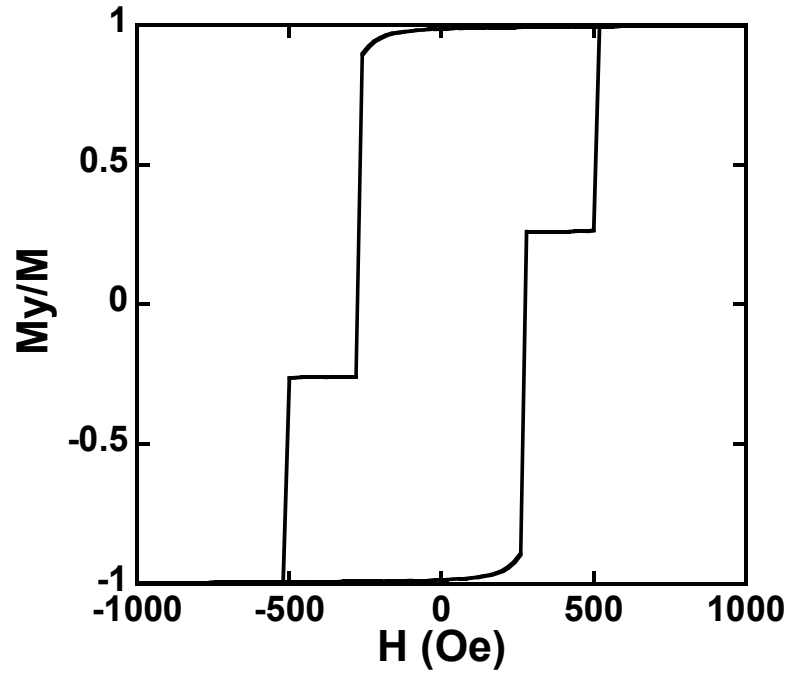
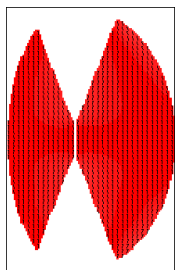
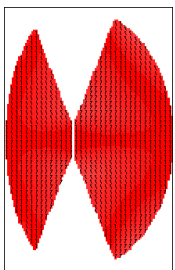
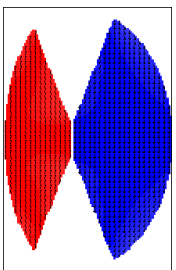
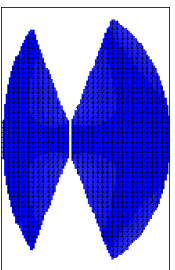
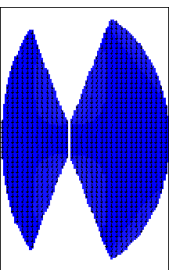


Fig. 6.2. The schematic of Ni nanogap for simulation.

Table 6.2. Spin configuration for Ni nanogap.

H	500 Oe	0 Oe	-400 Oe	-520 Oe	-1000 Oe
Spin Configuration					

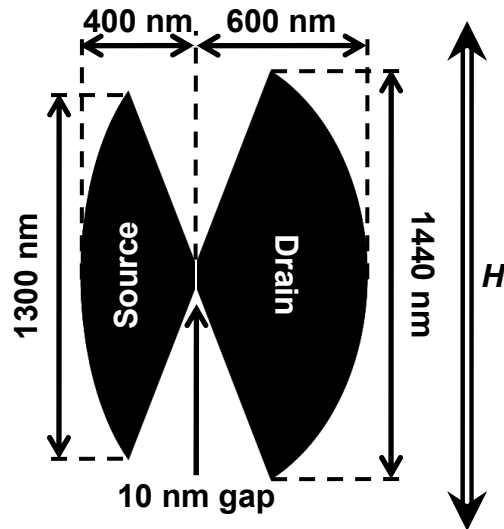


Fig. 6.3. The schematic of Ni nanogap for simulation.

Table 6.3. The basic parameters used for the simulations.

Material Name	Nickel
Saturation Magnetization (Ms)	$480 \times 10^3$ A/m
Exchange Stiffness constant (A)	$9 \times 10^{-12}$ J/m
Anisotropic Constant (Ku)	0 J/m <sup>3</sup>
Damping Constant ( $\alpha$ )	0.5
Cell Size	5 nm
Initial Magnetization	random
Sweep step of Field (H)	20 Oe
Thickness	30 nm

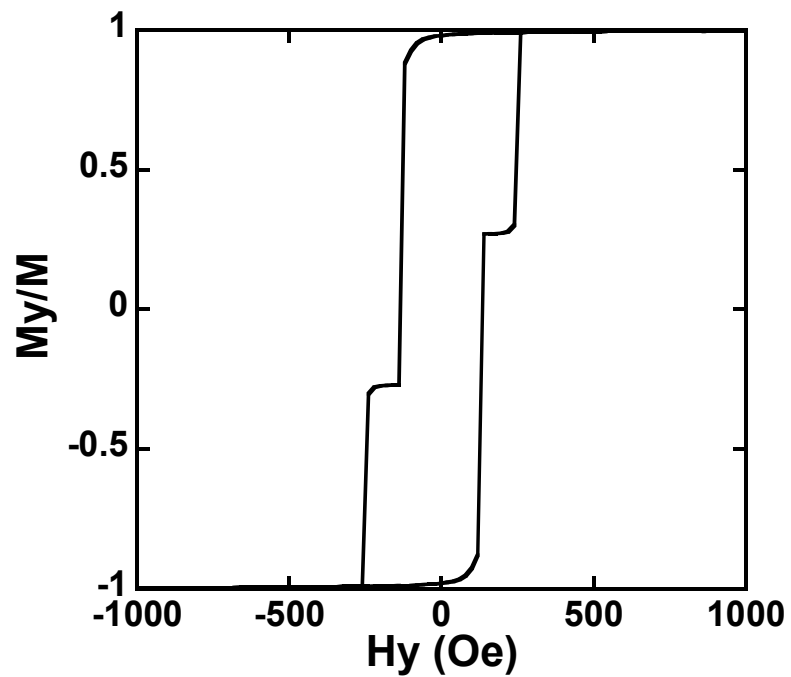
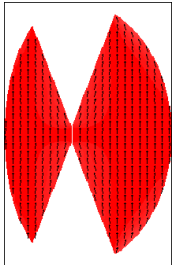
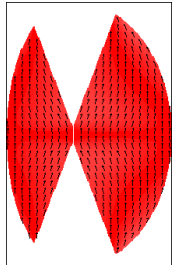
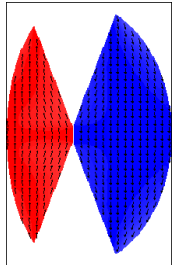
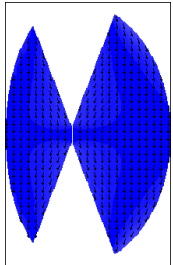
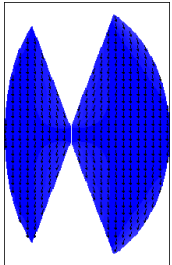


Fig. 6.4. The schematic of Ni nanogap for simulation.

Table 6.4. Spin configuration for Ni nanogap.

H	500 Oe	0 Oe	-140 Oe	-360 Oe	-500 Oe
Spin Configuration					

## **6.3 Planar-Type Ni-Vacuum-Ni Ferromagnetic Tunnel Junctions Fabricated by Activation Technique**

### **6.3.1 Asymmetrical Butterfly-Shape Electrodes with the Size of $720 \times 500 \text{ nm}^2$**

Figure 6.5 shows the schematic of nanogap formation using field-emission-induced electromigration (activation) technique. For the fabrication of devices shown in Table 6.5, electrical contact pads and ferromagnetic nanogaps were prepared by a two-step lithography procedure on Si wafers coated with 100 nm thermal oxide. First, Ti/Au contact pads, separated by 250 nm, were patterned by electron-beam (EB) lithography and EB evaporation onto the surface of SiO<sub>2</sub>. The contact pads were consisted of 5 nm-thick Ti and 25 nm-thick Au films. Then, 25 nm-thick Ni nanogaps with the spacing ranging from 20 to 50 nm were defined in the gap between the Ti/Au contact pads. The roughness of SiO<sub>2</sub> between source and drain electrodes is around 3 nm.

In order to achieve sub-10 nm spacing, initial gap separation between source and drain electrodes is progressively narrowed by the activation method, for electron transport in tunneling regime. Activation process was performed in a vacuum chamber at room temperature so as to mitigate oxidation of Ni atoms near the gap. A scanning electron microscopy (SEM) image of a representative planar-type Ni nanogap with initial gap separation of approximately 20 nm is shown in Table 6.5. The tip shape of the nanogaps was sharpened to generate field emission current caused by electric field concentration at the tip of the source and drain electrodes. We measured all of the electron transport properties during and after the activation step with a semiconductor parameter analyzer using high resolution source-monitor units in a shielded room. The resolution of the system is 0.1 fA/0.5  $\mu$ V. Mechanical vibrations were also suppressed in our measurement setup. A magnetic field was applied parallel to the easy axis of

magnetization along their long axis of the electrodes and was swept up to 2400 Oe.

Figure 6.6(a) shows electrical characteristics of the nanogap before and after performing the activation at room temperature with the preset current  $I_s = 25, 65, \text{ and } 80 \mu\text{A}$ . Initial gap separation of the nanogap was 45 nm. Consequently, the tunnel resistance of the nanogap was decreased from over 100 T $\Omega$  to 169 k $\Omega$  using the activation procedure. Figure 6.6(b) exhibits the current and derivative conductance as a function of the bias voltage at 16 K. The effective barrier height and barrier thickness of the planar-type Ni-Vacuum-Ni ferromagnetic tunnel junction formed by the activation were obtained, respectively, as 4 eV and <1 nm by the fitting of Simmons model [6]. The results suggest that the nanogap formed by the activation technique acts as a planar-type ferromagnetic tunnel junction with vacuum tunnel barrier.

Furthermore, Fig. 6.7(a) shows MR curve of the planar-type Ni nanogap at 16 K. The MR properties were measured at 16 K so as to exclude the influence of the thermal excitation electrons. The figure exhibits typical shape of major loop characteristics. It is shown in Fig. 6.7(a) that the MR value exhibits approximately 11.4 % with the bias voltage of 1.8 mV at 16 K. We can compare the magnitude of the MR with Julliere formula [8]:  $MR = (R_{ap}-R_p)/R_p = 2P^2 / (1-P^2)$ , where  $R_{ap}$  and  $R_p$  are the resistance of the magnetic tunnel junction (MTJ) corresponding to antiparallel and parallel magnetization of the ferromagnetic electrodes, respectively, and  $P$  is the tunneling spin polarization. Using  $P_{Ni} = 0.23$  [9], the Julliere estimate is  $MR = 11.2 \%$ . The MR ratio observed in Fig. 6.7(a) approximately corresponds to that estimated by the formula. Therefore, this result implies that the Ni nanogap acts as a planar-type Ni-Vacuum-Ni ferromagnetic tunnel junction, i.e., Ni electrodes are separated with single vacuum barrier. In fact, the vacuum barrier consisted of the nanogap is clearly exhibited in Table 6.5. The MR value

as a function of the applied bias voltage is represented in Fig. 6.7(b). With increasing the bias voltage from 1.8 to 22.5 mV, the MR value shows strong dependence on the bias voltage and decreases from 11.4 to 3.2 %, respectively. This bias dependence resembles the MR property as a function of bias voltage in electromigrated ferromagnetic breakjunctions with vacuum tunnel barriers [10].

Figure 6.8(a) shows magnetoresistance (MR) curves of the nanogap after performing the activation with  $I_s = 80 \mu\text{A}$ . The curves are offset vertically for clarity. At applied magnetic field of 1200 Oe, the resistance increases rapidly. Then, the increased resistance drops down to the initial magnitude at approximately -1500 Oe, as shown in Fig. 6.8(a). In our measurement setup, the maximum external field is limited to  $\pm 2400$  Oe. Therefore, these switching behaviors draw the typical shape of minor loop characteristics, in which the magnetization of the drain electrode should be reversing because the coercive force of the source is larger than that of the drain, as mentioned above. Furthermore, these minor loop properties imply that the coercive force of both source and drain electrodes increases as compared with the calculated result by Object Oriented MicroMagnetic Framework (OOMMF) shown in Fig. 6.2. It is considered that the surface of the Ni electrodes is usually covered with the native oxide of Ni, NiO. Since NiO is a famous antiferromagnetic material, the magnetization of the source electrode might be rigidly pinned by NiO [7]. The MR ratio of 12.2 % was obtained at 16 K and decreased from 12.2 % to 6.2 % with the increase of the bias voltage from 0.72 to 7.3 mV, as shown in Fig. 6.8(b). Since the nanogap simply consists of single vacuum barrier and Ni electrodes, the MR value is almost corresponding to that predicted by Julliere formula [8].

The temperature dependence of the MR ratio in the planar-type Ni-Vacuum-Ni

ferromagnetic tunnel junction formed by the activation is also exhibited in Fig. 6.9. In this figure, the applied bias voltage is fixed at 1.6 mV, and the measurement temperature is varied from 16 to 270 K. The MR ratio rapidly decreases from 11.6 to 1.2 % with increasing the temperature. It is noted that the dependencies of the MR ratio on the bias voltage and the measurement temperature are generally similar to those of Al<sub>2</sub>O<sub>3</sub>-based conventional MTJ stack. These results shown in Fig. 6.8(b) and Fig. 6.9 might be caused by “Vacuum” tunnel barrier system. In contrast to MgO barriers in Fe(001)/MgO(001)/Fe(001) single-crystalline MTJs [11], “Vacuum” barriers hardly promote efficient bonding and tunneling transmission of particular electron states. Thus, the magnitude of the MR appeared in Ni-Vacuum-Ni tunnel junction system clearly depends on the density of states of majority and minority spin electrons at the Fermi energy of the individual ferromagnetic electrode, as defined by Julliere’s formulation. Actually, the MR ratios in agreement with Julliere’s model are obtained experimentally. Hence, these results imply the activation technique can easily fabricate planar-type Ni-Vacuum-Ni ferromagnetic tunnel junctions and is suitable for the fabrication of various magnetoresistive nanoscale devices with vacuum tunnel barriers.



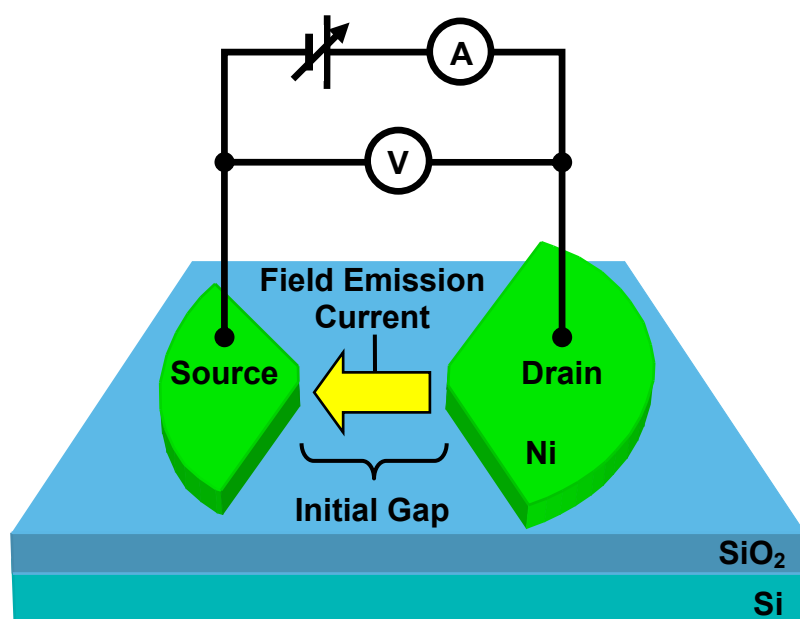
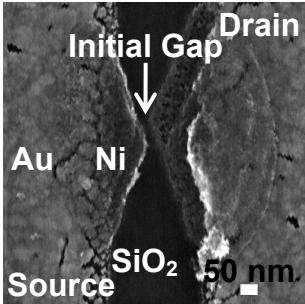
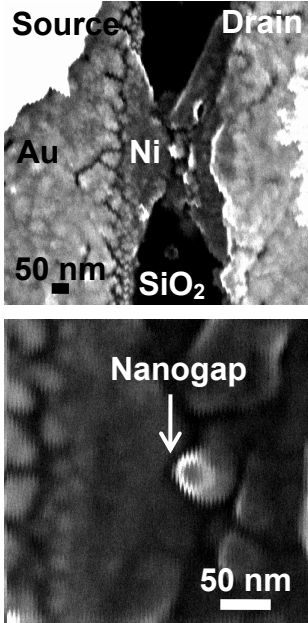


Fig. 6.5. Schematic of activation procedure. Initial gaps of Ni are fabricated on SiO<sub>2</sub>/Si substrates.

Table 6.5. The SEM images of Ni nanogap connected asymmetrical butterfly shape electrode before and after the activation procedure.

	Before Activation	After Activation
SEM Image		

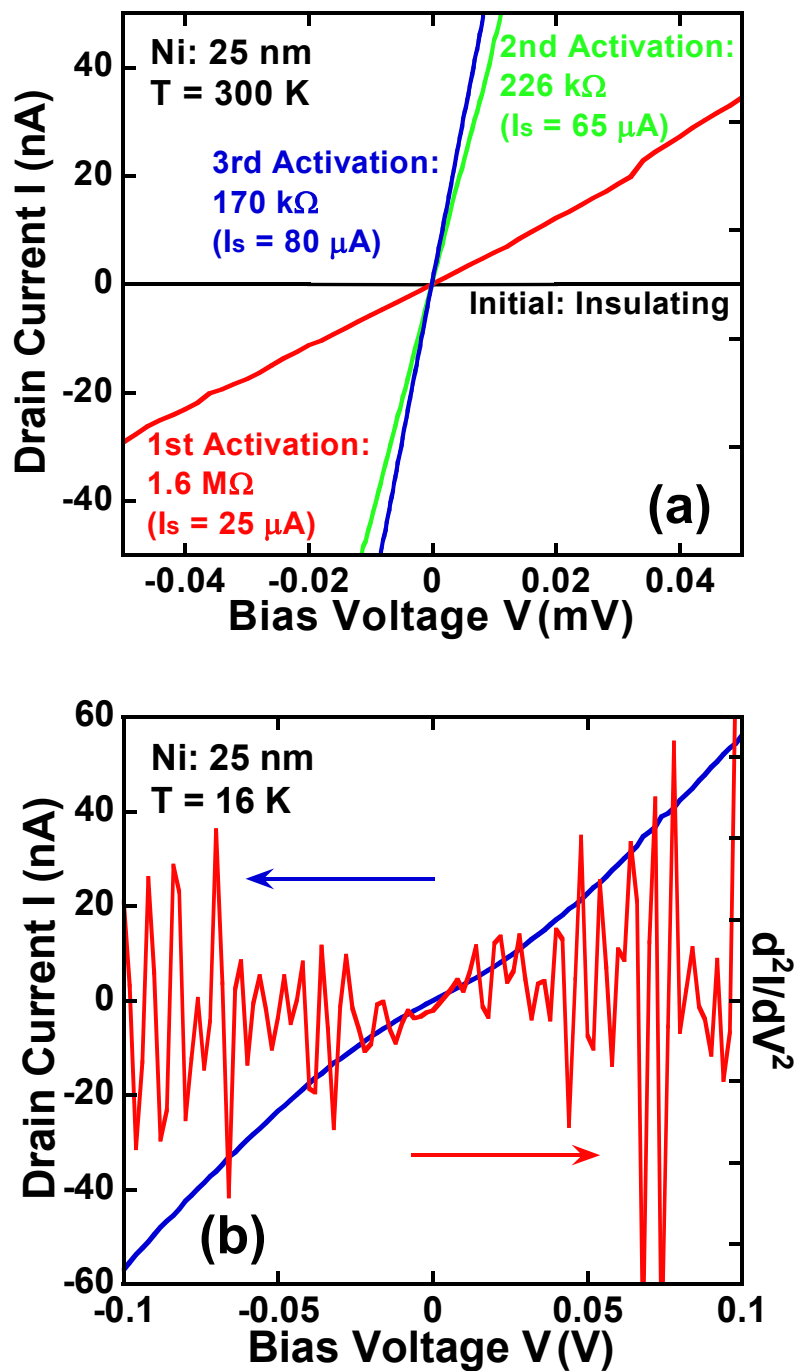


Fig. 6.6. (a)  $I$ - $V$  characteristics of the nanogap during activation procedure at room temperature. (b) Bias voltage dependence of the current and the derivative conductance of the nanogap at 16 K.

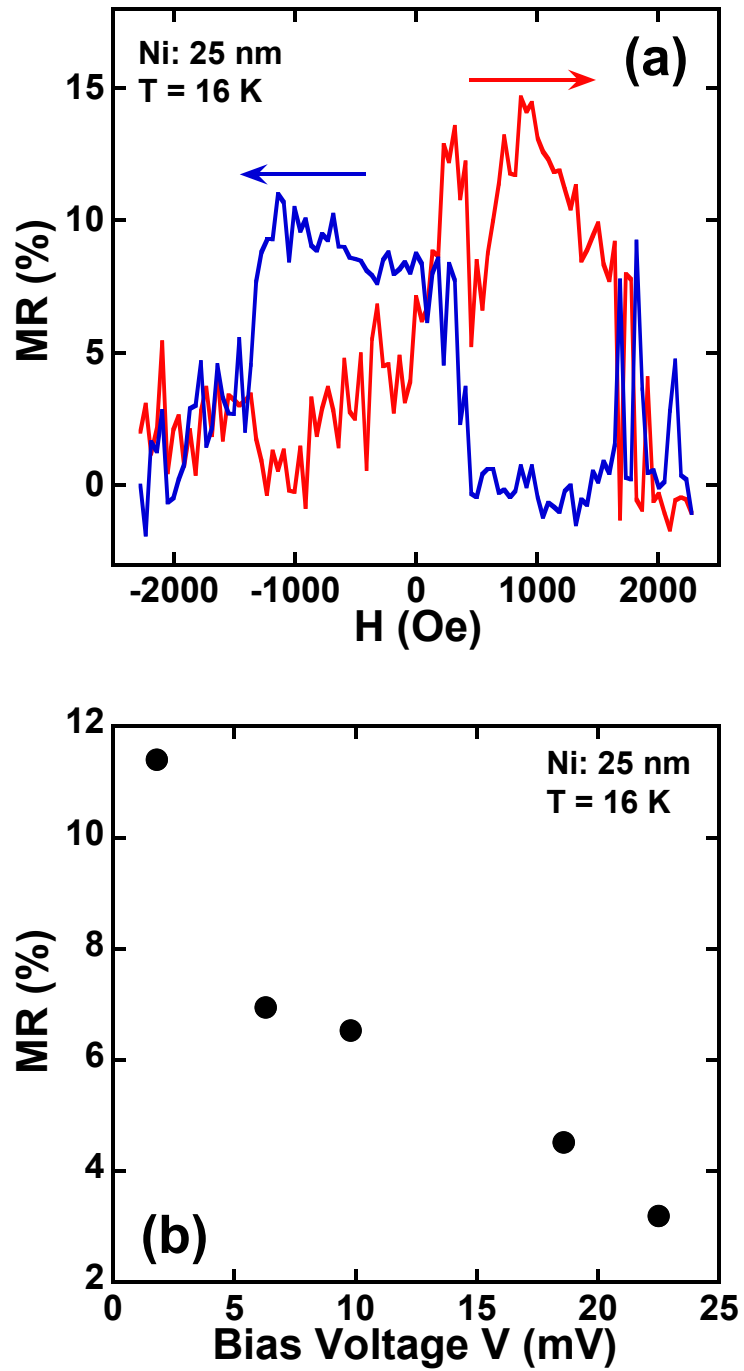


Fig. 6.7. (a) MR characteristics of planar-type Ni-Vacuum-Ni tunnel junction fabricated by activation. (b) MR ratio as a function of bias voltage at 16 K.

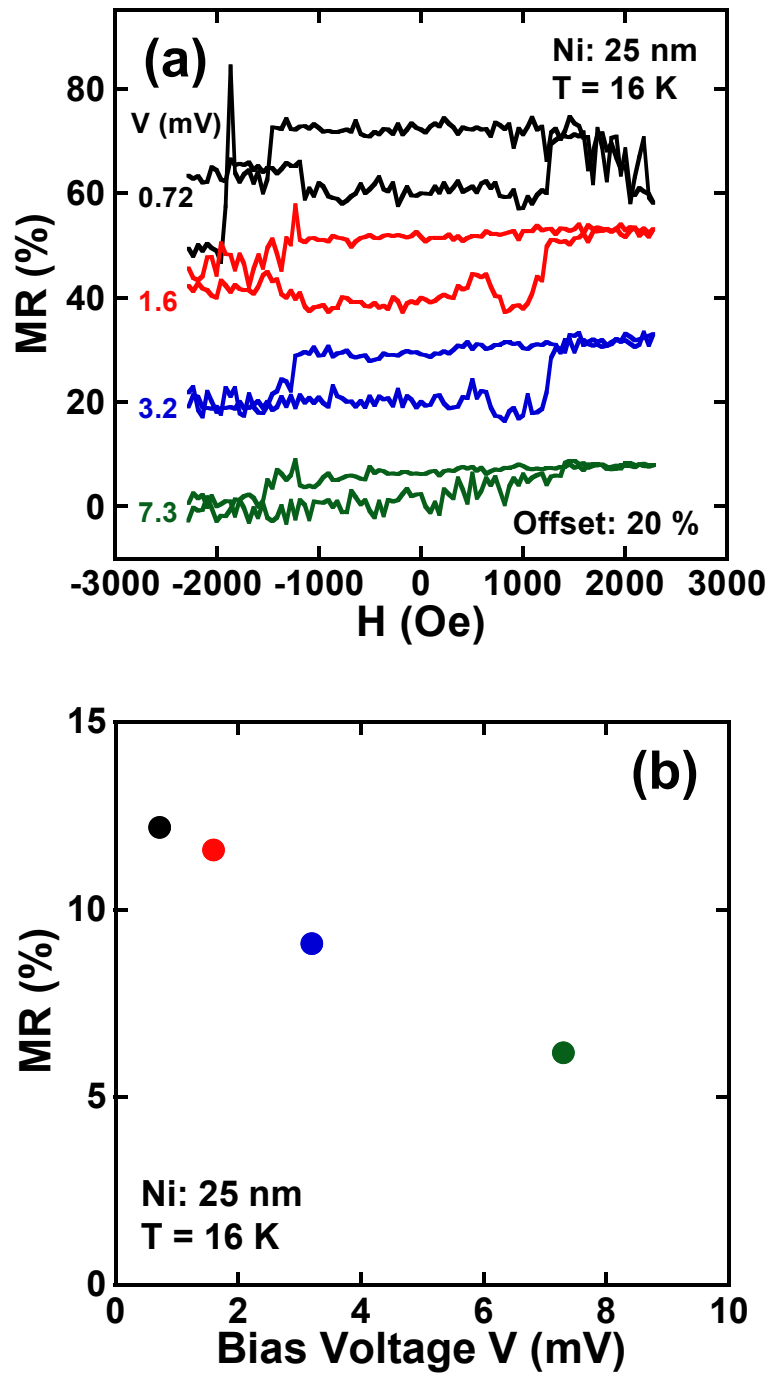


Fig. 6.8. (a) MR properties of the nanogap after performing the activation with  $I_s = 80 \mu\text{A}$ . The curves are offset vertically for clarity. (b) MR ratio as a function of bias voltage at 16 K.

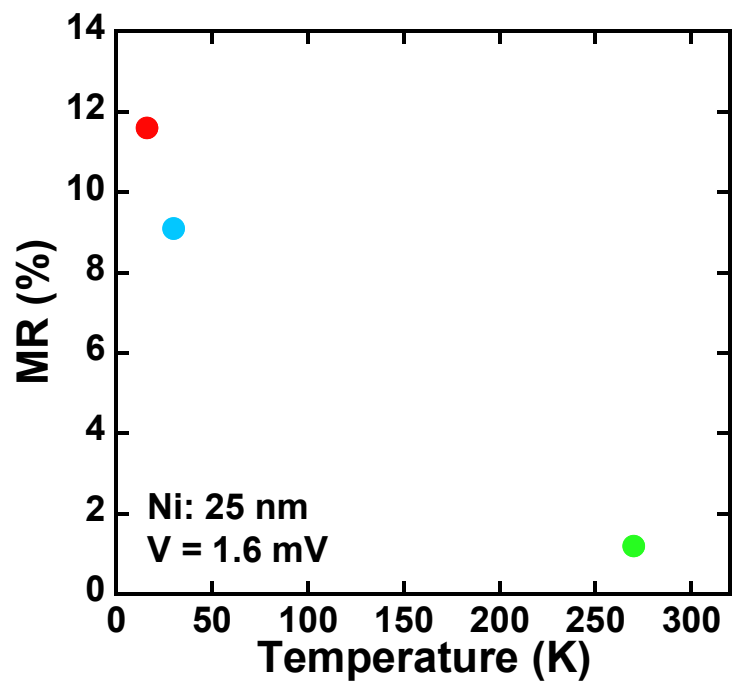


Fig. 6.9. MR ratio as a function of measurement temperature at 1.6 mV in the planar-type Ni-Vacuum-Ni ferromagnetic tunnel junction.

### 6.3.2 Asymmetrical Butterfly-Shape Electrodes with the Size of $1440 \times 1000 \text{ nm}^2$

Table 6.6 shows scanning electron microscopy (SEM) and atomic force microscope (AFM) images of a Ni initial nanogap before and after performing the activation procedure. The separation of the gap is approximately 40 nm, which is completely defined by electron-beam (EB) lithography. The figures clearly indicate that the separation of the initial nanogap reduces from about 40 nm before the activation to less than 10 nm after the activation. These observations strongly imply that the initial gap separation is clearly reduced from approximately 40 nm to less than 10 nm by the activation technique.

Figure 6.10(a) shows the current-voltage ( $I$ - $V$ ) characteristics of the nanogap before and after the activation with the preset current  $I_s$  from 4, 40, and 65  $\mu\text{A}$ . The tunnel resistance  $R$  decreases from the order of 100 T $\Omega$  to 95 k $\Omega$  with increasing the preset current  $I_s$ . Figure 6.10(b) exhibits the current and derivative conductance as a function of the bias voltage at 16 K. Since a sharp peak structures in the inelastic electron tunneling spectrum can be observed around  $\pm 20$  mV, which may be caused by the Ni phonon [12], the current is due to the electron tunneling between source and drain electrodes through the vacuum tunnel barrier. The results suggest that the nanogap formed by the activation technique acts as a planar-type ferromagnetic tunnel junction with vacuum tunnel barrier.

The Magnetoresistance (MR) curve of the planar-type Ni nanogap fabricated by activation technique is shown in Fig. 6.11(a). The resistance increased sharply at a magnetic field of approximately 400 Oe, and then rapidly dropped down to the initial value at about 1800 and -1000 Oe. A MR ratio as large as 80 % was obtained. Fig. 6.11(b) represents the MR ratio as a function of the bias voltage. The MR ratio of the

device decreases from approximately 350 % to 80 % with the increase of the bias voltage. This tendency is also similar to the behavior of electromigrated ferromagnetic breakjunctions with vacuum tunneling gap [10]. As shown in Table 6.6, Ni island structure is placed in the nanogap. The island size was estimated to be 70 nm from the charging energy of Fig. 6.10(b), which is larger than that of the SEM image of Table 6.6. Since the activation process is based on the motion of Ni atoms, the Ni atoms tend to accumulate as Ni dots/clusters in the nanogap and act as multiple islands, which are not resolved even by SEM and AFM. Therefore, these high MR ratios may be due to the single-electron charging effects caused by multiple ferromagnetic tunnel junction system in the nanogap [13]. The results suggest that the activation technique is suitable for the fabrication of planar-type ferromagnetic single-electron transistors (FMSETs) with vacuum tunnel barriers.



Table 6.6. The SEM and AFM images of Ni nanogap connected asymmetrical butterfly shape electrode before and after the activation procedure.

	Before Activation	After Activation
SEM Image	<p>SEM image showing the initial state of the Ni nanogap. The structure consists of a central Ni nanogap connected to two butterfly-shaped electrodes (Au) on a SiO<sub>2</sub> substrate. The electrodes are labeled Source and Drain. An arrow points to the 'Initial Gap' between the Ni electrodes. Scale bar: 200 nm.</p>	<p>SEM image showing the Ni nanogap after activation. The Ni electrodes are now covered with Ni clusters/dots. Labels: Source, Ni, Au, Drain, SiO<sub>2</sub>. Scale bar: 100 nm.</p>
AFM Image	<p>AFM image showing the initial state of the Ni nanogap. Labels: Source, Ni, SiO<sub>2</sub>, Au, Drain. Scale bar: 100 nm.</p> <p>High-magnification AFM image showing the initial gap between the Ni electrodes. Label: Initial Gap. Scale bar: 30 nm.</p>	<p>AFM image showing the Ni nanogap after activation. Labels: Source, Ni, SiO<sub>2</sub>, Au, Drain. Scale bar: 100 nm.</p> <p>High-magnification AFM image showing the Ni dots formed on the Ni electrodes after activation. Label: Ni Dots. Scale bar: 30 nm.</p>

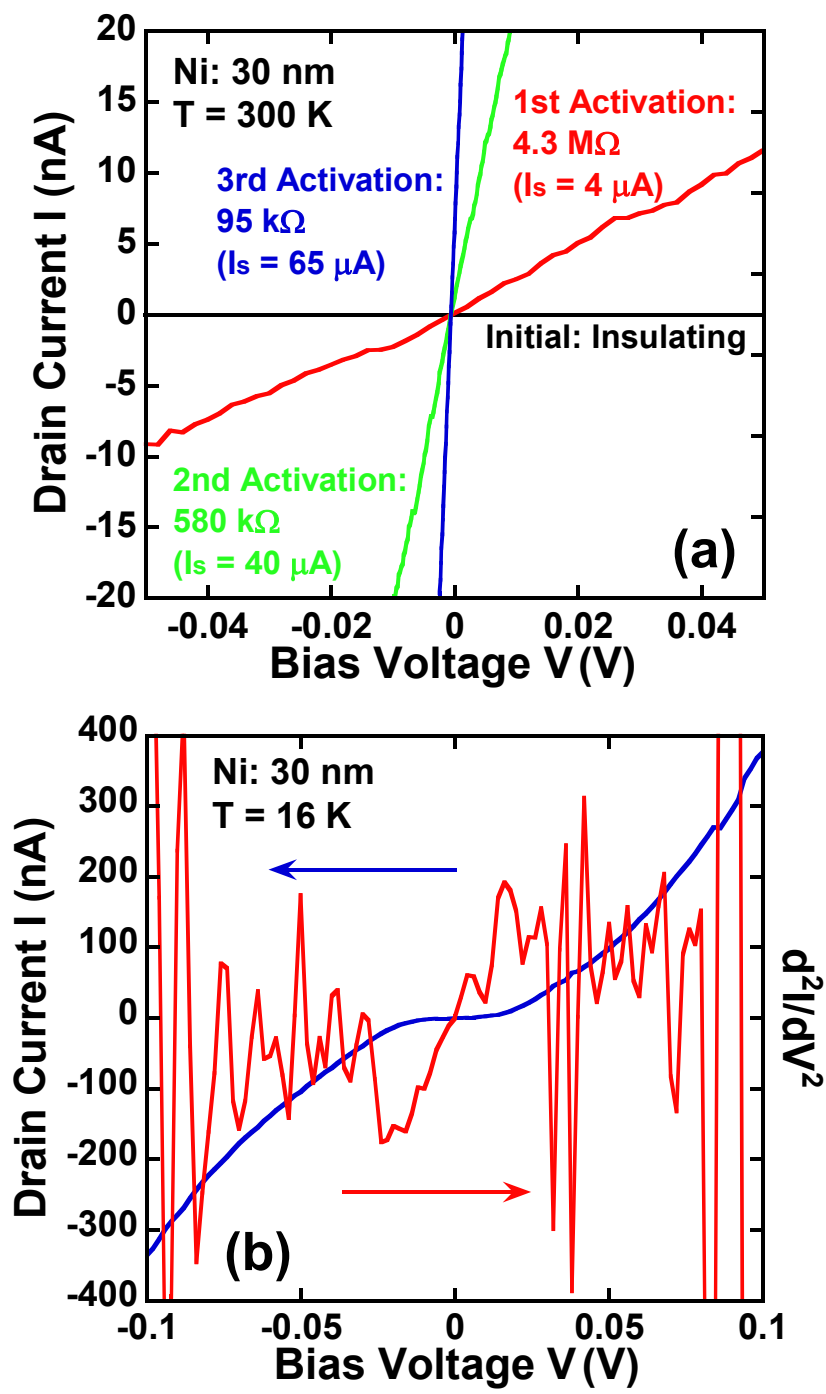


Fig. 6.10. (a)  $I$ - $V$  characteristics of the nanogap during activation procedure at room temperature. (b) Bias voltage dependence of the current and the derivative conductance of the nanogap at 16 K.

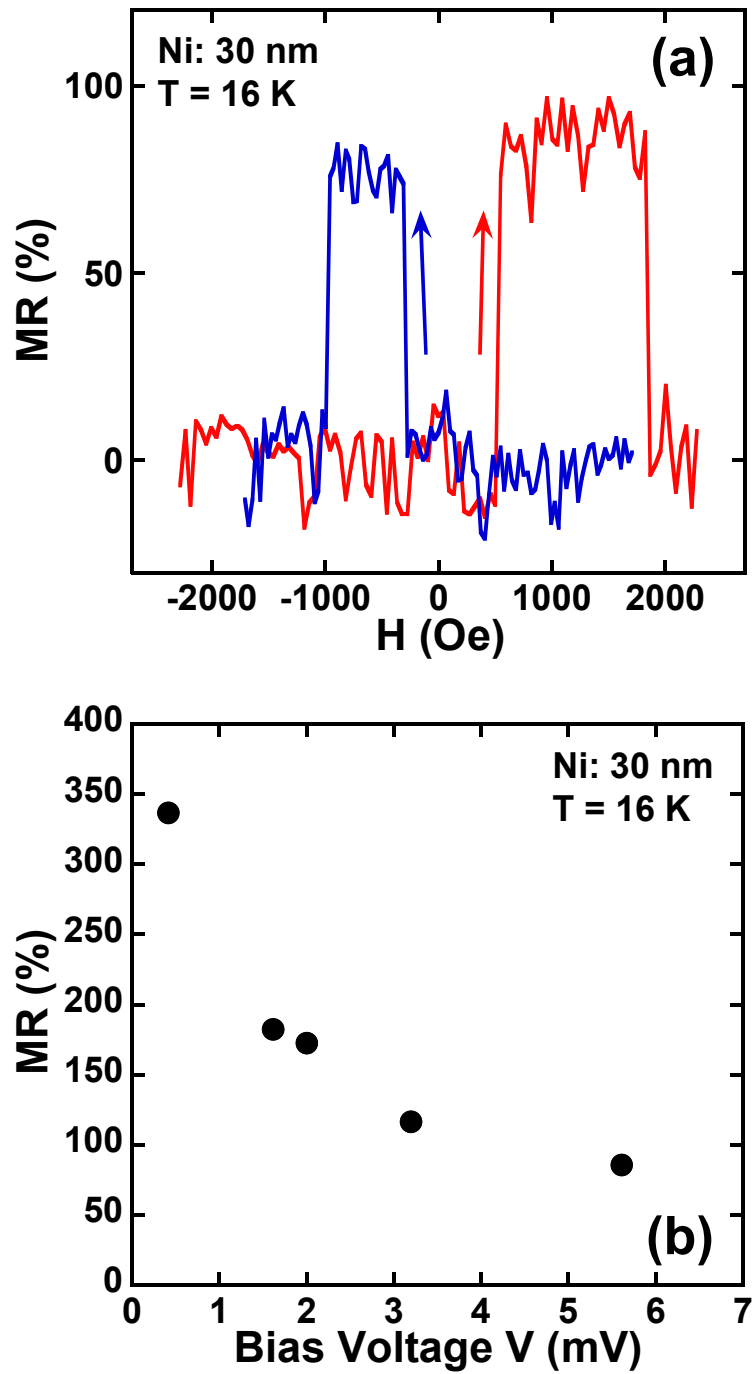


Fig. 6.11. (a) Magnetoresistance characteristics of planar-type Ni-Vacuum-Ni tunnel junction fabricated by activation. (b) MR ratio as a function of bias voltage.

## 6.4 Summary

Planar-type Ni-Vacuum-Ni ferromagnetic tunnel junctions are fabricated using field-emission-induced electromigration (EM), in which we call this approach “activation”. The activation is a simple and easy method for the control of tunnel resistance by only adjusting the magnitude of the preset current. We can easily obtain planar-type ferromagnetic tunnel junctions by monitoring the current passing through ferromagnetic nanogaps using the activation method. In order to induce magnetic shape anisotropy, asymmetrical butterfly-shape Ni nanogaps were patterned.

The resistance of the junction formed by the activation was varied by applying magnetic fields at 16 K. The magnetoresistance (MR) behaviors exhibited the typical shape of minor loop characteristics. The MR ratio decreased from 12.2 to 6.2 % with increasing the bias voltage from 0.72 to 7.3 mV. Furthermore, with increasing the measurement temperature from 16 to 270 K, the MR value decreases from 11.6 to 1.2 %. The MR value was almost corresponding to that estimated by the Julliere formula, suggesting that the nanogap simply acts as a Ni-Vacuum-Ni junction. These results imply that activation technique is effective to fabricate planar-type ferromagnetic nanoscale devices with vacuum tunnel barriers.

On the other hand, MR ratio in excess of 300 % at 16 K was obtained in the Ni nanogap with Ni clusters/dots fabricated by activation process. The MR increases from 80 % to 300 % with decreasing the bias voltage. The Ni clusters/dots act as multiple Ni islands of single-electron transistor. Thus, the high MR ratio may be due to the single-electron charging effects caused by ferromagnetic multiple tunnel junctions. The results strongly suggest that this EM technique can be useful to easily fabricate planar-type ferromagnetic devices with Ni-Vacuum-Ni tunnel junctions.

# **Chapter 7**

## **Planar-Type Single-Electron Transistors Produced by Field-Emission-Induced Electromigration**

### **7.1 Introduction**

Fabrication and control of nanometer-scale devices such as single-electron transistors (SETs) have recently become promising subjects of intensive study. Room temperature operation of the devices is considered to be an important milestone in SETs history. So far, a number of experiments have been reported for the production of SETs using nanofabrication scheme, which involves either highly elaborate electron-beam (EB) lithography [1], or special techniques and processes, such as shadow evaporation [2], deposition of metal nanoparticles [3-7], electromigration (EM) -induced breaking of thin metal wires defined by EB lithography [8, 9] and resistive microstrips with no intentional tunnel junctions [10, 11]. However, the SETs fabricated by these methods have been mainly restricted to the low temperature operation because of its small charging energy. Therefore, in order to investigate planar-type SETs, sophisticated nanofabrication scheme is required because of sub-nanometer dimension of the devices with higher operation temperature.

Previously, we have reported a wide-range control of tunnel resistance of Ni nanogaps having less than 70 nm separations using electromigration method induced by field emission current [12-14]. By applying a voltage to the Ni initial nanogaps, Fowler-Nordheim (F-N) field emission current flows through the nanogaps. The Ni atoms at the tip of the source electrode are sufficiently activated by the F-N field emission current

for the migration. Afterwards, the transfer of the Ni atoms from source to drain electrode is easily generated. Therefore, the separation of the nanogaps after performing the migration becomes narrower than that before the migration, resulting in a decrease of the tunnel resistance of the nanogaps. We call this electromigration procedure “activation”. Similar processes have been reported previously in studies of the formation of Au bridges across 70 nm slits [15] and insulated planar nanoscopic contacts [16]. These phenomena can be understood on the basis of the electrical breakdown procedure in planar contacts. In this paper, we describe a fabrication scheme of planar-type Ni-Vacuum-Ni based SETs with multiple tunnel junctions using activation method. Current-voltage ( $I$ - $V$ ) characteristics of the devices formed by the activation clearly exhibited the suppression of electrical current at low-bias voltages known as the Coulomb Blockade and Coulomb blockade voltage was also modulated by the gate voltage quasi-periodically at room temperature. Furthermore, we observed Coulomb staircase at 16 K. The control procedure of single-electron charging energy and the number of islands in the devices by the preset current of the activation is studied in detail.

## 7.2 Experimental Procedure

Activation experiments were performed on 100 nm thick, thermally grown SiO<sub>2</sub> surface on Si substrates. First, 25 nm thick Au contact pads were fabricated upon 5 nm Ti layer by electron-beam (EB) lithography and EB evaporation. Then, 20 nm thick, arrow-shaped Ni nanogaps with separations of 21-68 nm were formed by the same procedure in the gap between the Au contact pads. The arrow-shaped source-drain electrodes cause the concentration of electric field at the tip of the nanogap electrodes. Figure 7.1(a) shows a scanning electron microscope (SEM) image of the initial nanogap. Before performing the activation, the nanogap in the device exhibited the separation of 33 nm with high tunnel resistance above 100 TΩ.

Following these fabrication processes, we applied the activation procedure to the nanogaps. Initial nanogaps were installed on a stage with manual probes in a vacuum chamber with a pressure of 10<sup>-3</sup>-10<sup>-4</sup> Pa and were optionally selected from among the samples for the activation procedure. Through the experiments, the activation procedure was carried out in the vacuum chamber at room temperature. The electrical properties of the nanogaps during the activation were controlled and measured by a semiconductor parameter analyzer. Figure 7.2 shows flowchart of fabrication for SETs using activation procedure. The detailed activation process for the fabrication of the SETs consists of four main steps: (1) we set the magnitude of preset current  $I_s$ , (2) the voltage  $V$  is applied to the initial nanogap and is ramped up while monitoring the current  $I$  passing through the nanogap, (3) we stop the voltage  $V$  when the current  $I$  reaches a preset current  $I_s$ , and (4) after performing the activation, drain current  $I_d$  - drain voltage  $V_d$  properties of the device are measured with the modulation of gate voltage  $V_g$  to confirm SET characteristics. This procedure was continuously repeated to the devices with

increasing the preset current from 1 nA to 150  $\mu$ A.



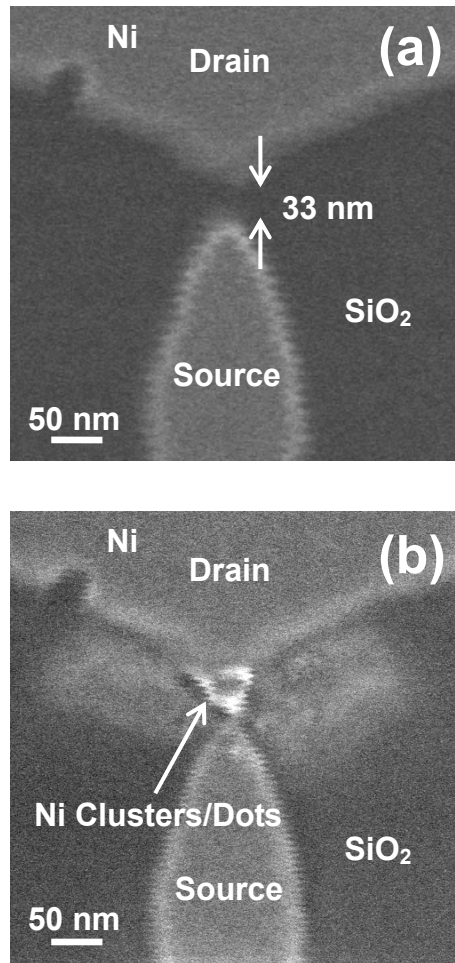


Fig. 7.1. SEM images of nanogap (a) before and (b) after activation with the preset current  $I_s = 150 \mu\text{A}$ .

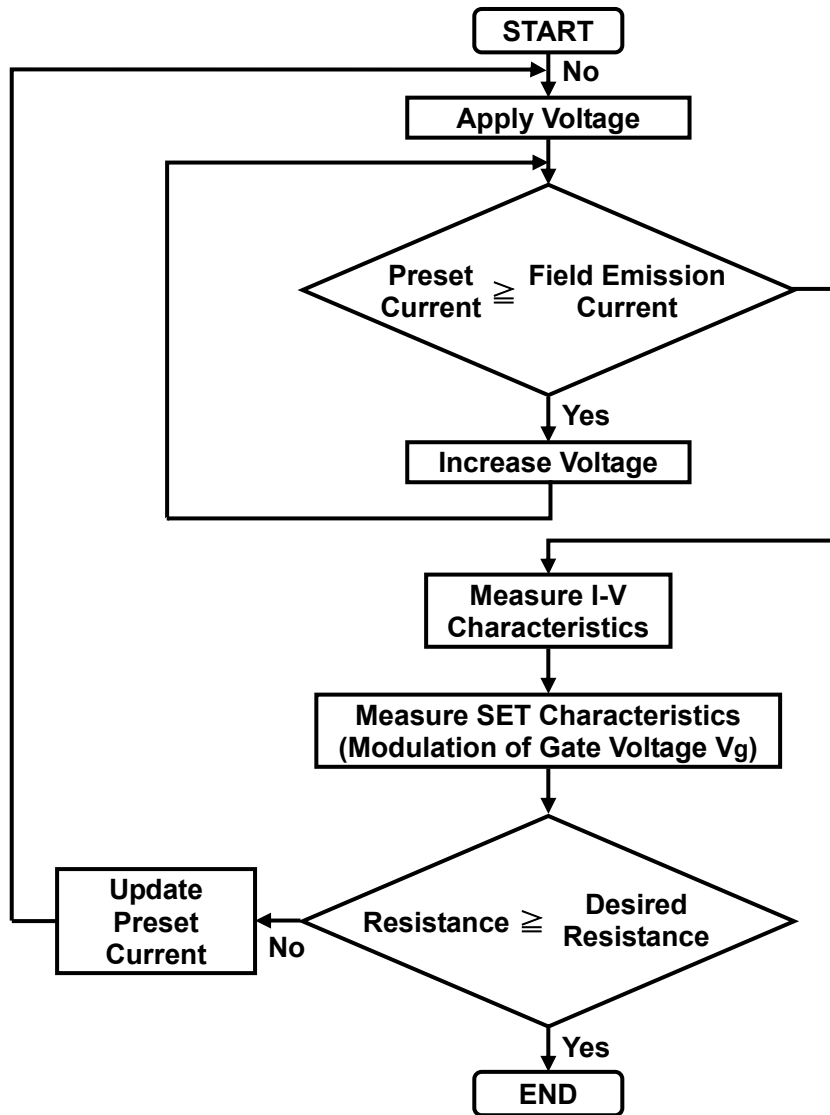


Fig. 7.2. Flowchart of fabrication for SET using activation procedure.

### 7.3 Drain Current-Drain Voltage Properties @ RT

The activation procedure was performed for the fabrication of planar-type Ni-based single-electron transistors (SETs). In the fabrication step of the SETs, as mentioned above, the voltage  $V$  was applied to the nanogaps with the preset current  $I_s$  from 1 nA to 150  $\mu$ A. Figure 7.1(a) shows a scanning electron microscopy (SEM) image of Ni initial nanogap before the activation. In the figure, initial gap separation is estimated to be approximately 33 nm. A SEM image of the nanogap after the activation with the preset current  $I_s = 150 \mu$ A is exhibited in Fig. 7.1(b). The image clearly indicates that the gap separation was narrowed from 33 nm to less than 10 nm by the accumulation of Ni atoms within the gap, suggesting the formation of Ni cluster/dot structures between source and drain electrodes.

Figure 7.3 represents the relation between the tunnel resistance  $R$  of the nanogaps and the preset current  $I_s$  during the activation procedure. The tunnel resistance  $R$ , which is defined as the resistance of the nanogaps in the low-voltage regime, was measured after performing the activation. The result suggests that the tunnel resistance  $R$  was decreased from 100 T $\Omega$  to 100 k $\Omega$  by increasing the preset current  $I_s$  from 1 nA to 150  $\mu$ A and was well controlled by the preset current  $I_s$ . Moreover, a marked decrease in the tunnel resistance  $R$  is clearly seen on the current range of  $100 \text{ nA} < I_s < 10 \mu\text{A}$ . We defined the current range as “Tunneling” in which the electrical properties of the nanogaps vary between “Insulating” and “Metallic” characteristics at room temperature [12-14].

From the point of view of the fabrication scheme of SETs, activation conditions were investigated in “Tunneling” regime, as shown with A, B and C in Fig. 7.3. First, we studied the electrical characteristics of the nanogap activated with the preset current

$I_s = 400$  nA (“A” in Fig. 7.3). Figure 7.4(a) shows the  $I_d$ - $V_d$  characteristics of the nanogap labeled “A” as a function of  $V_g$  and a current map measured as a function of  $V_d$  and  $V_g$  (inset). In the device, the gate voltage  $V_g$  was swept from -37 V to -35 V by 0.1 V step at room temperature. In Fig. 7.4(a), Coulomb blockade can be observed in the  $I_d$ - $V_d$  characteristics corresponding to the charging energy  $E_c = 580$  meV. Moreover, Coulomb blockade voltage was also modulated by the gate voltage  $V_g$  quasi-periodically, resulting in the formation of multiple tunnel junctions of the SETs. In general, Coulomb blockade is clearly visible when the charging energy is about ten to twenty times higher than the value of thermal fluctuation [17-20]. Hence, the device can be operated as the SETs at room temperature. The same measurement procedure was applied to the device after performing the activation with the preset current  $I_s = 650$  nA, as shown with “B” in Fig. 7.3.  $I_d$ - $V_d$  properties and a charging diagram were shown in Fig. 7.4(b). For the increase of the preset current  $I_s$  from 400 nA to 650 nA, the tunnel resistance of the device was reduced from 75 T $\Omega$  to 490 G $\Omega$  as shown in Fig. 7.3. Furthermore, the charging energy  $E_c$  of the device was also decreased from 580 meV to 470 meV with increasing the preset current. In spite of the decrease of the charging energy, several Coulomb peaks were obtained at room temperature, as shown in the inset of Fig. 7.4(b). This proves unambiguously that the device consists of metallic clusters/dots connected to source and drain electrodes through the multiple tunnel junctions, rather than a single junction. Figure 7.4(c) shows the electrical characteristics of the nanogap activated with the preset current  $I_s = 1.5$   $\mu$ A (“C” in Fig. 7.3), which is close to the preset current for “Metallic” activation regime. In the activation condition with  $I_s = 1.5$   $\mu$ A, electrical properties of the device gradually approach to “Metallic” properties. Therefore, the charging energy  $E_c$  of Fig. 7.4(c) was further reduced to 400 meV. Multiple Coulomb

diamonds were, however, still exhibited with the gate voltage. Hence, it is suggested that the Ni atoms tend to accumulate as Ni clusters/dots in the nanogap between source and drain electrodes, and act as multiple islands of the SETs. Furthermore, these results imply that the number of islands can be controlled by the magnitude of the preset current passing through the nanogap during the activation.

Figure 7.5 represents the fabrication conditions of the SETs as a function of initial gap separation  $W$  of the nanogaps and the preset current  $I_s$  of the activation procedure. Filled circles indicate that the devices show Coulomb blockade voltage in the  $I_d$ - $V_d$  characteristics at room temperature. Filled triangles and squares represent the devices with non-linear  $I_d$ - $V_d$  characteristics without Coulomb blockade properties and completely linear  $I_d$ - $V_d$  characteristics, at room temperature, respectively. The labels A, B and C in Fig. 7.5 correspond to those in Fig. 7.3 and 7.4. From the figure, the formation of the SETs operating at room temperature is achieved using the preset current from  $10^{-7}$  A to  $10^{-5}$  A in combination with the initial gap separation of the nanogaps from 21 nm to 68 nm.

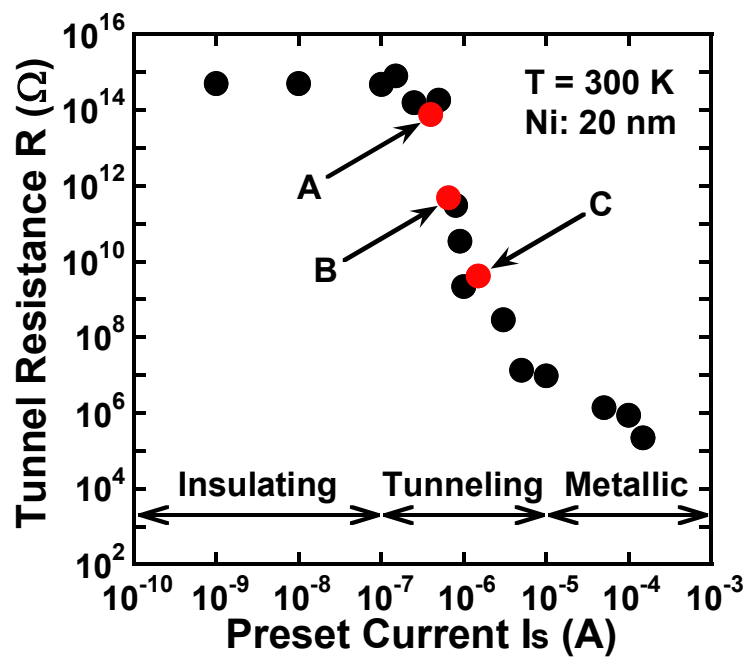


Fig. 7.3. Dependence of tunnel resistances of nanogaps on preset current  $I_s$ . The low-voltage tunnel resistance  $R$  is measured after the activation. The separation of the initial gap is about 33 nm. Labels A, B and C correspond to the devices activated with the preset current  $I_s = 400$  nA, 650 nA and 1.5  $\mu$ A, respectively.

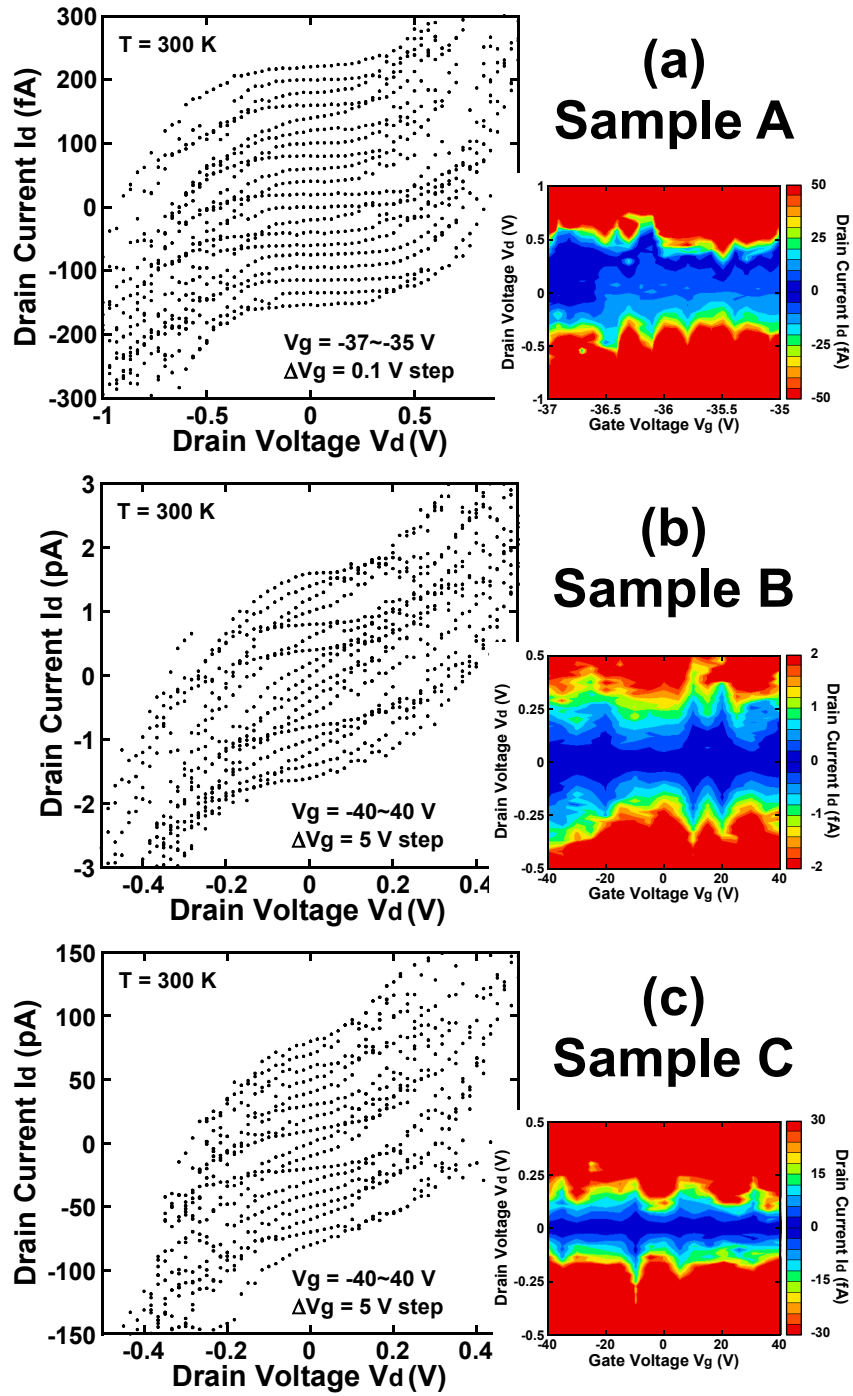


Fig. 7.4.  $I$ - $V$  characteristics of samples (a) A, (b) B, and (c) C at room temperature for different gate voltages. For clarity, each curve is shifted 20 fA (sample A), 200 fA (sample B), and 10 pA (sample C). The insets show current maps of the drain current  $I_d$ , versus  $V_d$  and  $V_g$  (stability diagram). The samples A, B, and C correspond to those in Fig. 7.3.

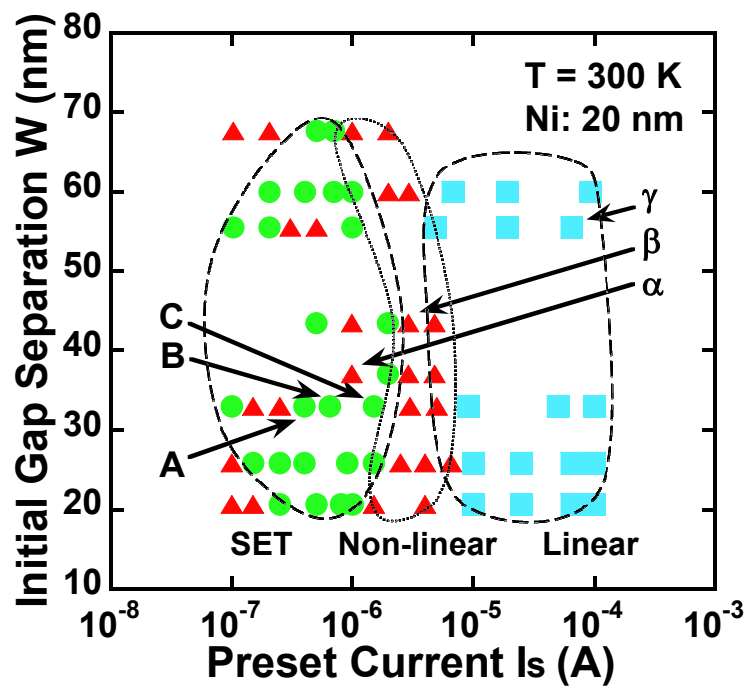


Fig. 7.5. Fabrication conditions of SETs as a function of initial gap separation  $W$  and preset current  $I_s$ . The symbols indicated devices with SET properties ( $\bullet$ ), non-linear  $I$ - $V$  without SET properties ( $\blacktriangle$ ), and linear  $I$ - $V$  properties ( $\blacksquare$ ). Labels A, B, and C and  $\alpha$ ,  $\beta$ , and  $\gamma$  correspond to those in Figs. 7.3 and 7.4 and Fig. 7.6, respectively.



## 7.4 Drain Current-Drain Voltage Properties @ 16 K

Particularly, the devices labeled  $\alpha$ ,  $\beta$  and  $\gamma$  didn't show Coulomb blockade properties at room temperature. However, when we cooled the devices to 16 K, the  $I_d$ - $V_d$  curves exhibited a clear suppression of the conductivity around zero bias regime, as shown in Figs 7.6(a), (b) and (c). The charging energy estimated from the  $I_d$ - $V_d$  curves of sample  $\alpha$  (Fig. 7.6(a)) and sample  $\beta$  (Fig. 7.6(b)) was 400 meV and 300 meV, at 16 K, respectively. This is due to the fact that the activation condition of sample  $\beta$  is closer to "Metallic" regime than that of sample  $\alpha$ . Furthermore, Coulomb staircases and periodic differential conductance peaks can be seen at 16 K in sample  $\gamma$  activated with the preset current  $I_s = 70 \mu\text{A}$ , as shown in Fig. 7.6(c). This result suggests that the single-electron transistor (SET) having asymmetrical two tunnel junctions with single island structure is formed using the activation condition within "Metallic" regime. It is noted that the charging energy of sample  $\gamma$  is determined to be 190 meV at 16 K but completely linear  $I_d$ - $V_d$  characteristics are obtained at room temperature. These results indicate that the charging energy of the devices was decreased from 400 meV to 190 meV even at 16 K with increasing the preset current from 1  $\mu\text{A}$  to 70  $\mu\text{A}$ , respectively.

Figure 7.7 shows the charging energy  $E_c$  of the devices as a function of the preset current  $I_s$  during the activation. The charging energy of the devices strongly relates with the preset current of the activation procedure, rather than the initial gap separation of the nanogaps. The results imply that the growth of Ni islands with increasing the preset current causes the increase of the size of the islands and results in the decrease of the number of the islands. Consequently, the preset current  $I_s$  in the activation procedure can control the charging energy and the number of islands during the formation of the SETs. Therefore, it is considered that initial gap separation and preset current are

important parameters so as to optimize the fabrication scheme of planar-type SETs by activation method.

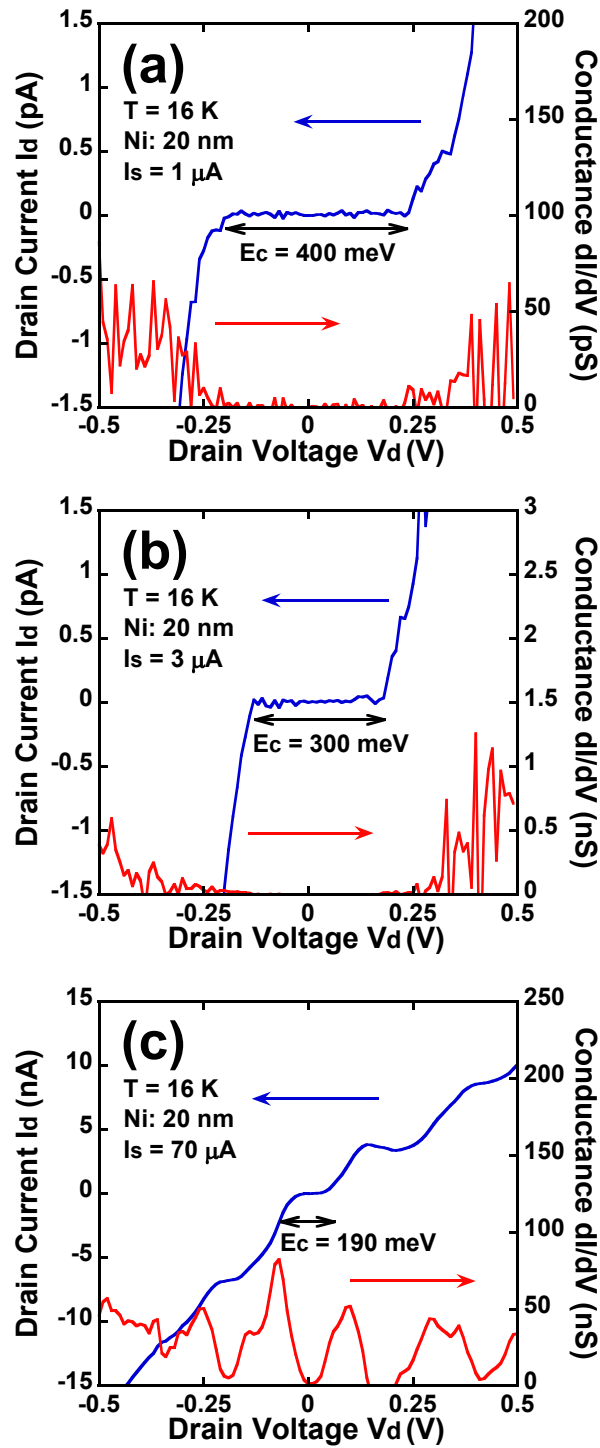


Fig. 7.6.  $I$ - $V$  characteristics and corresponding differential conductance of SET devices at 16 K. Samples (a)  $\alpha$ , (b)  $\beta$ , and (c)  $\gamma$  represent devices activated with different preset current  $I_s = 1\ \mu\text{A}$ ,  $3\ \mu\text{A}$ , and  $70\ \mu\text{A}$ , respectively.

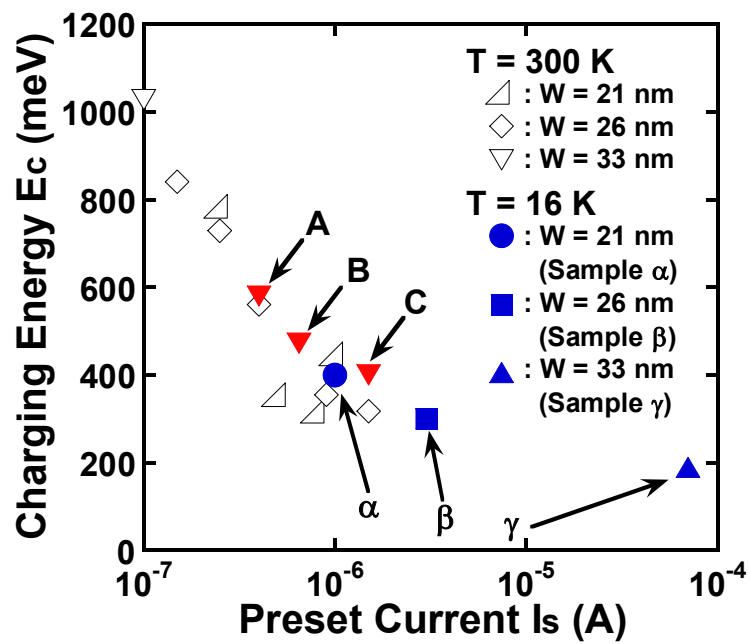


Fig. 7.7. Charging energy  $E_c$  versus preset current  $I_s$  of SET devices at 16 K and room temperature. Labels A, B, and C and  $\alpha$ ,  $\beta$ , and  $\gamma$  correspond to those in Figs. 7.3, 7.4 and 7.5 and Figs. 7.5 and 7.6, respectively.

## 7.5 Summary

In conclusion, we present a novel technique for the fabrication of planar-type Ni-based single-electron transistors (SETs) consisting of nanogaps. This method is based on electromigration induced by F-N field emission current and is called “activation”. When the activation was applied to the nanogaps, the  $I_d$ - $V_d$  characteristics of the nanogaps at room temperature displayed Coulomb blockade properties. Additionally, Coulomb blockade voltage was modulated by the gate voltage quasi-periodically, resulting in the formation of multiple islands of SETs. Furthermore, as the preset current  $I_s$  was increased, the charging energy  $E_c$  was decreased. It is suggested that the control of the charging energy  $E_c$  is possible with the preset current  $I_s$  of the activation. In contrast to the previously reported method, the present method allows us to simplify the fabrication process further and control the charging energy and the number of the islands of the planar-type Ni-based SETs at room temperature. The activation is simple and easy method for the fabrication of planar-type SETs.

# Chapter 8

## General Conclusions

### 8.1 Planar-Type Ni-Ni oxide-Ni Ferromagnetic Tunnel Junctions Obtained by SPM Local Oxidation

Scanning probe microscopy (SPM) local oxidation technique was applied to Ni thin films for the fabrication of nanoscale magnetoresistive devices. For the observation of magnetoresistance (MR) difference across the junction, the Ni channel was asymmetrically patterned by focus ion beam lithography and photolithography, in order to induce magnetic shape anisotropy. Ni oxide wires formed by SPM local oxidation act as insulating barrier. Non-linear current-voltage ( $I$ - $V$ ) characteristics were obtained from planar-type Ni-Ni oxide-Ni ferromagnetic tunnel junctions. This suggests that Ni oxide wires formed by SPM local oxidation technique act as an insulating barrier material for the electron. The MR properties of planar-type Ni-Ni oxide-Ni ferromagnetic tunnel junction were clearly observed by applying a magnetic field. MR ratio exhibited above 100 % at 16K and decreased with increasing the bias voltage and measurement temperature. This result strongly suggests that planar-type Ni-Ni oxide-Ni ferromagnetic tunnel junctions show the possibilities for nanoscale magnetoresistive devices.

## **8.2 Stepwise Feedback-Controlled Electromigration for Fabrication of Planar-Type Ni-Vacuum-Ni Ferromagnetic Tunnel Junctions**

A simple method for the control the resistance of the nanoconstrictions and fabrication of planar-type ferromagnetic tunnel junctions, based on the break of metal nanoconstrictions induced by stepwise feedback-controlled electromigration (SFCE). In order to induce magnetic shape anisotropy, asymmetrical butterfly shape and broad bean shape were patterned for Ni nanoconstrictions. Using the SFCE technique, the resistance of nanoconstrictions can be controlled from metallic regime to tunneling regime. Since a peak in the inelastic electron tunneling spectrum of electrical properties after performing the SFCE process can be observed, the current due to the electron tunneling between Ni electrodes through the vacuum barrier. Furthermore, magnetoresistance (MR) curves of planar-type Ni-Vacuum-Ni ferromagnetic tunnel junctions clearly show the major loop properties at 16 K. The MR ratio of approximately 4 % at 16 K decreases with the increase of the bias voltage. These results suggest that the SFCE technique can be useful to easily fabricate planar-type ferromagnetic devices with Ni-Vacuum-Ni tunnel junctions.

## **8.3 Formation of Planar-Type Ni-Vacuum-Ni Ferromagnetic Tunnel Junctions Using Field-Emission-Induced Electromigration**

We have investigated a novel technique for the formation of nanogaps, which is based on field-emission-induced electromigration (activation). In the nanogaps with asymmetrical butterfly shape, the tunnel resistance of the nanogaps decreased from 100

T $\Omega$  to 100 k $\Omega$  with increasing the preset current  $I_s$  during activation procedure. Magnetoresistance (MR) ratio of 12.2 % was obtained from planar-type Ni-Vacuum-Ni ferromagnetic tunnel junction at 16 K. The MR ratio approximately corresponds to that estimated by Julliere formula and decreases with increasing the applied bias voltage. On the other hand, MR ratio in excess of 300 % at 16 K was obtained in the Ni nanogap fabricated by this newly proposed activation process. The results strongly suggest that this EM technique can be useful to easily fabricate planar-type ferromagnetic devices with Ni-Vacuum-Ni tunnel junctions.

#### **8.4 Planar-Type Single-Electron Transistors Produced by Field-Emission-Induced Electromigration**

Planar-type single-electron transistors (SETs) fabricated using field-emission-induced electromigration (activation) were reported. This technique is based on electromigration induced by F-N field emission current. When the activation was applied to the nanogaps, the  $I_d$ - $V_d$  characteristics of the nanogaps at room temperature displayed Coulomb blockade properties. Additionally, Coulomb blockade voltage was modulated by the gate voltage quasi-periodically, resulting in the formation of multiple islands of SETs. Furthermore, as the preset current  $I_s$  was increased, the charging energy  $E_c$  was decreased. It is suggested that the control of the charging energy  $E_c$  is possible with the preset current  $I_s$  of the activation. In contrast to the previously reported method, the present method allows us to simplify the fabrication process further and control the charging energy and the number of the islands of the planar-type Ni-based SETs at room temperature. The activation is a simple and easy method for the fabrication of planar-type SETs.



## 8.5 Summary

In conclusions, scanning probe microscopy (SPM) local oxidation, stepwise feedback-controlled electromigration (SFCE), and field-emission-induced electromigration (activation) are proposed as novel nanofabrication techniques. These novel techniques can be fabricated oxide of vacuum tunnel barriers with nanometer scale. This suggests that planar-type ferromagnetic nanoscale devices can be fabricated using the techniques.

Planar-type ferromagnetic tunnel junctions fabricated by these techniques exhibit tunneling transport and magnetoresistance characteristics at 16 K. Furthermore, electrical properties of planar-type single-electron transistors (SETs) can be controlled using activation technique.

Finally, we can imagine experiments probing the electrical and magnetoresistive characteristics of planar-type ferromagnetic single-electron transistors (FMSETs) much more controllably than the experiments in Chapter 6 and 7 by sophisticated these techniques. It would be interesting to observe the interplay of spin and charge in FMSETs.

## Acknowledgements

The author would like to express my sincere gratitude to my supervisor, Associate Professor Jun-ichi Shirakashi for providing me this precious study opportunity as a student of post-graduate course in his laboratory.

The author would like to thank Professor Nobuyoshi Koshida, Professor Yoshiyuki Suda, Professor Toshiyuki Sameshima, Associate Professor Hiroki Minoda, and Professor Yasushi Takemura for their critical comments, advice and useful discussions.

The author would like to express hearty thanks to all members of Shirakashi and Koshida Labs., especially Mr. S. Nishimura, Y. Shibata (Murata Manufacturing Co.), T. Kawashima (JEOL Ltd.), Y. Eto (TOSHIBA Co.), Y. Kuwabara, Dr. H. Yoshimura, Mr. T. Ohta, and M. Romain for their expert technical assistance and valuable discussions.

The author is very grateful to T. Ogino (Canon Inc.), K. Kayashima (Sony Co.), M. Motoyama (Hitachi Ltd.), K. Takahashi (Sony Co.), S. Itami, W. Kume, M. Hanada, T. Watanabe, S. Ueno, R. Yasutake, K. Takiya, and I. Atsumo for their valuable cooperation in my experiments.

This study is partially supported by Research Fellowships of the Japan Society for the Promotion of Science for Young Scientists and Human Resource Development Program for Scientific Powerhouse.

Finally I would like to extend my indebtedness to father, mother, grandfather and grandmother for their endless love, understanding, support, encouragement and sacrifice throughout my study.

# References

## *Chapter 1*

- [1] J. Bardeen and W. H. Brattain, *Phys. Rev.* **74** (1947) 230.
- [2] W. Shockley, *Bell Syst. Tech. J.* **28** (1949) 435.
- [3] M. N. Baibich, J. M. Broto, A. Fert, F. Nguyen Van Dau, F. Petroff, P. Eitenne, G. Creuzet, A. Friederich, and J. Chazelas, *Phys. Rev. Lett.* **61** (1988) 2472.
- [4] J. Barnaś, A. Fuss, R. E. Camley, P. Grünberg, and W. Zinn, *Phys. Rev B* **42** (1990) 8110.
- [5] M. Julliere, *Phys. Let. A* **54** (1975) 225.
- [6] P. M. Tedrow and R. Meservey, *Phys. Rev. B* **7** (1973) 318.
- [7] T. Miyazaki and N. Tezuka, *J. Magn. Magn. Mater.* **139** (1995) L231.
- [8] J. S. Moodera, L. R. Kinder, T. M. Wong, and R. Meservey, *Phys. Rev. Lett.* **74** (1995) 3273.
- [9] K. Ono, H. Shimada, and Y. Ootuka, *J. Phys. Soc. Jpn.* **66** (1997) 1261.
- [10] L. F. Schelp, A. Fert, F. Fetta, P. Holody, S. F. Lee, J. L. Maurice, F. Petroff, and A. Vaurès, *Phys. Rev. B* **56** (1997) R5747.
- [11] S. Mitani, S. Takahashi, K. Takanashi, K. Yakushiji, S. Maekawa, and H. Fujimori, *Phys. Rev. Lett.* **81** (1998) 2799.
- [12] J. Wunderlich, T. Jungwirth, B. Kaestner, A. C. Irvine, A. B. Shick, N. Stone, K. –Y. Wang, U. Rana, A. D. Giddings, C. T. Foxon, R. P. Campion, D. A. Williams, and B. L. Gallagher, *Phys. Rev. Lett.* **97** (2006) 077201.
- [13] S. Takahashi and S. Maekawa, *Phys. Rev. Lett.* **80** (1998) 1758.
- [14] J. Shirakashi and Y. Takemura, *J. Appl. Phys.* **89** (2001) 7365.
- [15] J. Shirakashi and Y. Takemura, *J. Appl. Phys.* **91** (2002) 7442.

[16] J. Shirakashi and Y. Takemura, *J. Appl. Phys.* **93** (2003) 6873.

## ***Chapter 2***

[1] H. R. Zeller and I. Giaever, *Phys. Rev.* **181** (789) 1969.

[2] J. Lambe and R. C. Jaklevic, *Phys. Rev. Lett.* **22** (1371) 1969.

[3] K. K. Likharev, *IEEE Trans. Magn.* **23** (1987) 1142.

[4] S. A. Wolf, D. D. Awschalom, R. A. Buhrman, J. M. Daughton, S. von Molnár, M. L. Roukes, A. Y. Chtchelkanova, and D. M. Treger, *Science* **294** (2001) 1488.

[5] K. Ono, H. Shimada, and Y. Ootuka, *J. Phys. Soc. Japan* **66** (1997) 1261.

[6] J. Wunderlich, T. Jungwirth, B. Kaestner, A. C. Irvine, A. B. Shick, N. Stone, K. -Y. Wang, U. Rana, A. D. Giddings, C. T. Foxon, R. P. Campion, D. A. Williams, and B. L. Gallagher, *Phys. Rev. Lett.* **97** (2006) 077201.

[7] M. M. Deshmukh and D. C. Ralph, *Phys. Rev. Lett.* **89** (2002) 266803.

[8] A. N. Pasupathy, R. C. Bialczak, J. Martinek, J. E. Grose, L. A. K. Donev, P. L. McEuen, and D. C. Ralph, *Science* **306** (2004) 86.

[9] S. Sahoo, T. Kontos, J. Furer, C. Hoffmann, M. Gräber, A. Cottet, and C. Schönenberger, *Nat. Phys.* **1** (2005) 99.

[10] J. Shirakashi and Y. Takemura, *J. Appl. Phys.* **89** (2001) 7365.

[11] J. Shirakashi and Y. Takemura, *J. Appl. Phys.* **91** (2001) 7442.

[12] J. Shirakashi and Y. Takemura, *J. Appl. Phys.* **93** (2001) 6873.

[13] D. V. Averin and K. K. Likharev, in *Mesoscopic Phenomena in Solids*, edited by B. L. Altshuler, P. A. Lee, and R. A. Webb (North-Holland, Amsterdam, 1991), p. 173.

[14] M. Johnson and R. H. Silsbee, *Phys. Rev. Lett.* **55** (1985) 1790.

[15] M. Johnson and R. H. Silsbee, *Phys. Rev. B* **37** (1988) 5326.

- [16] M. Johnson, Phys. Rev. Lett. **70** (1993) 2142.
- [17] P. M. Tedrow and R. Meservey, Plasma Phys. Rep. **238** (1994) 174.
- [18] S. Takahashi and S. Maekawa, Phys. Rev. Lett. **80** (1998) 1758.
- [19] J. Barnaś and A. Fert, Phys. Rev. Lett. **80** (1998) 1058.
- [20] K. Majumdar and S. Hershfield, Phys. Rev. B **57** (1998) 11521.

### ***Chapter 3***

- [1] Y. Nakamura, ChiiDong Chen, and Jaw-Shen Tsai, Jpn. J. Appl. Phys. **35** (1996) L1465.
- [2] D. L. Klein, P. L. McEuen, J. E. B. Katari, R. Roth, and A. P. Alivisatos, Appl. Phys. Lett. **68** (1996) 2574.
- [3] M. A. Reed, C. Zhou, C. J. Muller, T. P. Burgin, and J. M. Tour, Science **278** (1997) 252.
- [4] A. Bezryadin, C. Dekker, and G. Schmid, Appl. Phys. Lett. **71** (1997) 1273.
- [5] A. F. Morpurgo, C. M. Marcus, and D. B. Robinson, Appl. Phys. Lett. **74** (1999) 2084.
- [6] Y. Kashimura, H. Nakashima, K. Furukawa, and K. Torimitsu, Thin Solid Films **438-439** (2003) 317.
- [7] H. Park, A. K. L. Lim, J. Park, A. P. Alivisatos, and P. L. McEuen, Appl. Phys. Lett. **75** (1999) 301.
- [8] J. Shirakashi and Y. Takemura, IEEE Trans. Mag. **40** (2004) 2640.
- [9] Y. Tomoda, Y. Shibata, J. Shirakashi, and Y. Takemura, J. Appl. Phys. **99** (2006) 08T312.

- [10]Y. Tomoda, S. Kayashima, T. Ogino, M. Motoyama, Y. Takemura, and J. Shirakashi, *J. Magn. Magn. Mater.* **310** (2007) e641.
- [11]K. Takahashi, Y. Tomoda, S. Itami, and J. Shirakashi, *Int. Conf. Nanoscience + Technology (ICN+T 2008)*, Keystone, CO, USA.
- [12]S. Kayashima, K. Takahashi, M. Motoyama, and J. Shirakashi, *Jpn. J. Appl. Phys.* **46** (2007) L907.
- [13]S. Kayashima, K. Takahashi, M. Motoyama, and J. Shirakashi, *J. Phys. Conf. Ser.* **100** (2008) 052022.
- [14]Y. Tomoda, K. Takahashi, M. Hanada, W. Kume, and J. Shirakashi, *J. Vac. Sci. and Technol. B* **27** (2009) 813.
- [15]Y. Tomoda, K. Takahashi, M. Hanada, W. Kume, S. Itami, T. Watanabe, and J. Shirakashi, *IEEE Trans. Mag.* **45** (2009) 3480.
- [16]Y. Tomoda, M. Hanada, W. Kume, S. Itami, T. Watanabe, and J. Shirakashi, *J. Phys. Conf. Ser.* **200** (2010) 062035.
- [17]J. A. Dagata, J. Schneir, H. H. Harary, C. J. Evans, M. T. Postek, and J. Bennett, *Appl. Phys. Lett.* **56** (1990) 2001.
- [18]J. A. Dagata, T. Inoue, J. Itoh, K. Morimoto, and H. Yokoyama, *J. Appl. Phys.* **84** (1998) 6891.
- [19]R. Garcia, M. Calleja, and H. Rohrer, *J. Appl. Phys.* **86** (1999) 1898.
- [20]F. Perez-Murano, K. Birkelund, K. Morimoto, and J. A. Dagata, *Appl. Phys. Lett.* **75** (1999) 199.
- [21]Y. Takemura, S. Kidaka, K. Watanabe, Y. Nasu, T. Yamada, and J. Shirakashi, *J. Appl. Phys.* **93** (2003) 7346.

- [22]K. I. Bolotin, F. Kuemmeth, A. N. Pasupathy, and D. C. Ralph, Appl. Phys. Lett. **84** (2004) 3154.
- [23]Y. Noguchi, T. Nagase, T. Kubota, T. Kamikado, and S. Mashiko, Thin Solid Films **499** (2006) 90.
- [24]M. L. Trouwborst, S. J. van der Molen, and B. J. van Wees, J. Appl. Phys. **99** (2006) 114316.
- [25]D. R. Strachan, D. E. Smith, D. E. Johnston, T. -H. Park, M. J. Therien, D. A. Bonnell, and A. T. Johnson, Appl. Phys. Lett. **86** (2005) 043109.
- [26]G. Esen and M. S. Fuhrer, Appl. Phys. Lett. **87** (2005) 263101.
- [27]R. Hoffmann, D. Weissenberger, J. Hawecker, and D. Stöffler, Appl. Phys. Lett. **93** (2008) 043118.
- [28]Z. K. Keane, L. H. Yu, and D. Natelson, Appl. Phys. Lett. **88** (2006) 062514.
- [29]T. Takahashi, Y. Tomoda, S. Itami, and J. Shirakashi, J. Vac. Soc. and Technol. B **27** (2009) 805.
- [30]M. Yoshida, Y. Oshima, and K. Takayanagi, Appl. Phys. Lett. **87** (2005) 103104.
- [31]J. L. Cost-Krämer, N. García, P. García-Mochales, P. A. Serena, M. I. Marqués, and A. Correia, Phys. Rev. B **55** (1997) 5416.
- [32]F. Elhoussine, S. Mátéfi-Tempfli, A. Encinas, and L. Piraux, Appl. Phys. Lett. **81** (2002) 1681.
- [33]R. H. Fowler and L. Nordheim, Proc. Roy. Soc. A **121** (1928) 626.
- [34]I. A. Blech and E. Kinsbron, Thin Solid Films **25** (1975) 327.
- [35]H. J. Mamin, P. H. Guethner, and D. Rugar, Phys. Rev. Lett. **65** (1990) 2418.
- [36]C. S. Chang, W. B. Su, and Tien T. Tsong, Phys. Rev. Lett. **72** (1994) 574.
- [37]G. S. Hsiao, R. M. Penner, and J. Kingsley, Appl. Phys. Lett. **64** (1994) 1350.

[38]D. Fujita and T. Kumakura, Appl. Phys. Lett. **82** (2003) 2329.

#### ***Chapter 4***

[1] J. A. Dagata, J. Schneir, H. H. Harary, C. J. Evans, M. T. Postek, and J. Bennett, Appl. Phys. Lett. **56** (1990) 2001.

[2] J. Shirakashi and Y. Takemura, IEEE Trans. Magn. **40** (2004) 2640.

[3] Y. Takemura and J. Shirakashi, Adv. Eng. Mat. **7** (2005) 170.

[4] Y. Tomoda, Y. Shibata, J. Shirakashi, and Y. Takemura, J. Appl. Phys. **99** (2006) 08T312.

[5] J. G. Simmons, J. Appl. Phys. **34** (1963) 1793.

[6] M. Julliere, Phys. Lett. A **54** (1975) 225.

[7] N. Tezuka, M. Oogane, and T. Miyazaki, J. Magn. Magn. Mater. **198-199** (1999) 149.

[8] J. S. Moodera, Lisa R. Kinder, Terrilyn M. Wong, and R. Meservey, Phys. Rev. Lett. **74** (1995) 3273.

[9] N. Tezuka and T. Miyazaki, Jpn. J. Appl. Phys. **37** (1998) L218.

[10]Y. Ando, J. Murai, H. Kubota, and T. Miyazaki, J. Appl. Phys. **87** (2000) 5209.

[11]C. Lü, et al., Phys. Lett. A **319** (2003) 205.

[12]X. F. Han, et al., J. Magn. Magn. Mater. **282** (2004) 225.

[13]J. Zhang and R. White, J. Appl. Phys. **83** (1998) 6512.

[14]J. Shirakashi and Y. Takemura, J. Appl. Phys. **89** (2001) 7365.

[15]N. García, M. Muñoz, G. G. Qian, H. Rohrer, I. G. Saveliev, and Y. -W. Zhao, Appl. Phys. Lett. **79** (2001) 4550.

[16]S. Maekawa and U. Gäfvert, IEEE. Trans. Magn. **18** (1982) 707.



- [17] C. Cowache, B. Diény, S. Auffret, M. Cartier, R. H. Taylor, R. O'Barr, and S. Y. Yamamoto, *IEEE Trans. Magn.* **34** (1998) 843.

## ***Chapter 5***

- [1] H. Park, A. K. L. Lim, J. Park, A. P. Alivisatos, and P. L. McEuen, *Appl. Phys. Lett.* **75** (1999) 301.
- [2] R. Sordan, K. Balasubradamanian, M. Burghard, and K. Kern, *Appl. Phys. Lett.* **87** (2005) 013106.
- [3] S. Kayashima, K. Takahashi, M. Motoyama, and J. Shirakashi, *Jpn. J. Appl. Phys.* **46** (2007) L907.
- [4] S. Kayashima, K. Takahashi, M. Motoyama, and J. Shirakashi, *J. Phys. Conf. Ser.* **100** (2008) 052022.
- [5] K. I. Bolotin, F. Kuemmeth, A. N. Pasupathy, and D. C. Ralph, *Appl. Phys. Lett.* **84** (2004) 3154.
- [6] Y. Noguchi, T. Nagase, T. Kubota, T. Kamikado, and S. Mashiko, *Thin Solid Films* **499** (2006) 90.
- [7] M. L. Trouwborst, S. J. van der Molen, and B. J. van Wees, *J. Appl. Phys.* **99** (2006) 114316.
- [8] D. R. Strachan, D. E. Smith, D. E. Johnston, T. -H. Park, M. J. Therien, D. A. Bonnell, and A. T. Johnson, *Appl. Phys. Lett.* **86** (2005) 043109.
- [9] Z. K. Keane, L. H. Yu, and D. Netelson, *Appl. Phys. Lett.* **88** (2006) 062514.
- [10] K. Takahashi, Y. Tomoda, S. Itami, and J. Shirakashi, *J. Vac. Sci. and Technol. B*, **27** (2009) 805.
- [11] H. Heersche, G. Lientschnig, K. O'Neil, H. S. J. van der Zant, and H. W.

- Zandbergen, Appl. Phys. Lett. **91** (2007) 072107.
- [12] T. Taychatanapat, K. I. Bolotin, F. Kuemmeth, and D. C. Ralph, Nano Lett. **7** (2007) 652.
- [13] D. R. Stachan, D. E. Johnston, B. S. Guiton, S. S. Datta, P. K. Davies, D. A. Bonnell, and A. T. C. Johnson, Phys. Rev. Lett. **100** (2008) 056805.
- [14] OOMMF is Object Oriented MicroMagnetic Framework, a micromagnetic simulation code available free from NIST at <http://math.nist.gov/oommf/>.
- [15] J. G. Simmons, J. Appl. Phys. **34** (1963) 1793.
- [16] Kirill I. Bolotin, F. Kuemmeth, Abhay N. Pasupathy, and D. C. Ralph, Nano Lett. **6** (2006) 123.

## ***Chapter 6***

- [1] S. Kayashima, K. Takahashi, M. Motoyama, and J. Shirakashi, Jpn. J. Appl. Phys. **46** (2007) L907.
- [2] S. Kayashima, K. Takahashi, M. Motoyama, and J. Shirakashi, J. Phys. Conf. Ser. **100** (2008) 052022.
- [3] Y. Tomoda, K. Takahashi, M. Hanada, W. Kume, and J. Shirakashi, J. Vac. Sci. and Technol. B, **27** (2009) 813.
- [4] Y. Tomoda, K. Takahashi, M. Hanada, W. Kume, S. Itami, T. Watanabe, and J. Shirakashi, IEEE Trans. Mag. **45** (2009) 3480.
- [5] OOMMF is Object Oriented MicroMagnetic Framework, a micromagnetic simulation code available free from NIST at <http://math.nist.gov/oommf/>.
- [6] J. G. Simmons, J. Appl. Phys. **34** (1963) 1793.
- [7] S. A. Makhlof, H. Al-Attar, and R. H. Kodama, Solid State Com. **145** (2008) 1.

- [8] M. Julliere, Phys. Let. A **54** (1975) 225.
- [9] R. Meservey and P. M. Tedrow, Phys. Rep. **238** (1994) 173.
- [10] K. I. Bolotin, F. Kuemmeth, A. N. Pasupathy, and D. C. Ralph, Nano Lett. **6** (2006) 123.
- [11] S. Yuasa, T. Nagahama, A. Fukushima, Y. Suzuki, and K. Ando, Nat. Mater. **3** (2004) 868.
- [12] Y. Tomoda, S. Kayashima, T. Ogino, M. Motoyama, Y. Takemura, and J. Shirakashi, J. Magn. Magn. Mater. **310** (2007) e641.
- [13] J. Shirakashi and Y. Takemura, J. Appl. Phys. **89** (2001) 7365.

## ***Chapter 7***

- [1] K. Liu, Ph. Avouris, J. Bucchignano, R. Martel, S. Sun, and J. Michl, Appl. Phys. Lett. **80** (2002) 865.
- [2] Y. Nakamura, C. D. Chen, and J. S. Tsai, Jpn. J. Appl. Phys. **35** (1996) L1465.
- [3] S. I. Khondaker and Z. Yao, Appl. Phys. Lett. **81** (2002) 4613.
- [4] U. C. Coskun, H. Mebrahtu, P. B. Huang, J. Huang, D. Sebba, A. Biasco, A. Makarovski, A. Lazarides, T. H. LaBean, and G. Finkelstein, Appl. Phys. Lett. **93** (2008) 123101.
- [5] W. Chen, H. Ahmed, and K. Nakazoto, Appl. Phys. Lett. **66** (1995) 3383.
- [6] A. Bezryadin, C. Dekker, and G. Schmid, Appl. Phys. Lett. **71** (1997) 1273.
- [7] D. L. Klein, P. L. McEuen, J. E. B. Katari, R. Roth, and A. P. Alivisatos, Appl. Phys. Lett. **68** (1996) 2574.
- [8] H. Park, A. K. L. Lim, A. P. Alivisatos, J. Park, and P. L. McEuen, Appl. Phys. Lett.

- 75 (1999) 301.
- [9] K. I. Bolotin, F. Kuemmeth, A. N. Pasupathy, and D. C. Ralph, *Appl. Phys. Lett.* **84** (2004) 3154.
- [10] V. A. Krupenin, A. B. Zorin, M. N. Savvateev, D. E. Presnov, and J. Niemeyer, *J. Appl. Phys.* **90** (2001) 2411.
- [11] X. Luo, A. O. Orlov, and G. L. Snider, *Microelectronics J.* **36** (2005) 308.
- [12] S. Kayashima, K. Takahashi, M. Motoyama, and J. Shirakashi, *Jpn. J. Appl. Phys.* **46** (2007) L907.
- [13] S. Kayashima, K. Takahashi, M. Motoyama, and J. Shirakashi, *J. Phys. Conf. Ser.* **100** (2008) 052022.
- [14] Y. Tomoda, K. Takahashi, M. Hanada, W. Kume, and J. Shirakashi, *J. Vac. Sci. and Technol. B*, **27** (2009) 813.
- [15] A. Anaya, A. L. Korotkov, M. Bowman, J. Waddell, and D. Davidovic, *J. Appl. Phys.* **93** (2003) 3501.
- [16] A. Bramanti, G. Maruccio, P. Visconti, S. D'Amico, R. Cingolani, and R. Rinaldi, *IEEE Trans. Electron Devices.* **53** (2006) 2958.
- [17] J. Shirakashi, K. Matsumoto, N. Miura, and M. Konagai, *Jpn. J. Appl. Phys.* **37** (1998) 1594.
- [18] J. Shirakashi, K. Matsumoto, N. Miura, and M. Konagai, *Appl. Phys. Lett.* **72** (1998) 1893.
- [19] J. Shirakashi, K. Matsumoto, N. Miura, and M. Konagai, *J. Appl. Phys.* **83** (1998) 5567.
- [20] C. Dubuc, J. Beauvais, and D. Drouin, *IEEE Trans. Nanotechnol.* **7** (2008) 68.

## List of Publications

### < Papers >

- 1) Y. Tomoda, Y. Shibata, J. Shirakashi, and Y. Takemura  
“Magnetoresistance effect of planar-type ferromagnetic tunnel junctions”  
J. Appl. Phys. **99** (2006) 08T312.
- 2) Y. Tomoda, S. Kayashima, T. Ogino, M. Motoyama, Y. Takemura, and J. Shirakashi  
“Planar-Type Ferromagnetic Tunnel Junctions Fabricated by SPM Local Oxidation”  
J. Magn. Magn. Mater. **310** (2007) e641-e643.
- 3) K. Takahashi, Y. Tomoda, S. Itami, and J. Shirakashi  
“Control of Channel Resistance on Metal Nanowires by Electromigration Patterning Method”  
J. Vac. Sci. Technol. B **27** (2009) 953-957.
- 4) Y. Tomoda, K. Takahashi, M. Hanada, W. Kume, and J. Shirakashi  
“Fabrication of Nanogap Electrodes by Field-Emission-Induced Electromigration”  
J. Vac. Sci. Technol. B **27** (2009) 813-816.
- 5) Y. Tomoda, K. Takahashi, M. Hanada, W. Kume, S. Itami, T. Watanabe, and J. Shirakashi  
“Magnetoresistance Properties of Planar-Type Tunnel Junctions with Ferromagnetic Nanogap System Fabricated by Electromigration Method”  
IEEE Trans. Mag. **45** (2009) 3480-3483.
- 6) Y. Tomoda, K. Takahashi, M. Hanada, W. Kume, S. Itami, T. Watanabe, and J. Shirakashi  
“Fabrication of Planar-Type Ferromagnetic Tunnel Junctions Using Electromigration Method and Its Magnetoresistance Properties”  
J. Phys. Conf. Ser. **200** (2010) 062035.

- 7) W. Kume, Y. Tomoda, M. Hanada, and J. Shirakashi  
“Fabrication of Single-Electron Transistors Using Field-Emission-Induced Electromigration”  
J. Nanosci. Nanotechnol. (2010), in print.
  
- 8) S. Itami, Y. Tomoda, R. Yasutake, and J. Shirakashi  
“Influence of Feedback Parameters on Resistance Control of Metal Nanowires by Stepwise Feedback-Controlled Electromigration”  
J. Nanosci. Nanotechnol. (2010), in print.

< **International Conferences** >

- 1) J. Shirakashi, Y. Tomoda, Y. Shibata, R. Ito, H. Sato, and Y. Takemura  
“Planar Type Diodes with Ferromagnetic Lateral Tunnel Junctions Fabricated by SPM Local Oxidation”  
49th Annual Conference on Magnetism and Magnetic Materials (MMM-49),  
November 7-11, 2004, Jacksonville, USA. Abstract Book, pp.331.
  
- 2) Y. Shibata, Y. Tomoda, J. Shirakashi, and Y. Takemura  
“Local Oxidation Nanolithography of Ferromagnetic Thin Films Using Tapping Mode SPM”  
50th Annual Conference on Magnetism and Magnetic Materials (MMM-50), October  
30 - November 3, 2005, San Jose, CA, USA. Abstract Book, pp.214.
  
- 3) Y. Tomoda, Y. Shibata, J. Shirakashi, and Y. Takemura  
“Magnetoresistance Effect of Planar-Type Ferromagnetic Tunnel Junctions”  
50th Annual Conference on Magnetism and Magnetic Materials (MMM-50), October  
30 - November 3, 2005, San Jose, CA, USA. Abstract Book, pp.486.
  
- 4) Y. Tomoda, S. Kayashima, Y. Shibata, J. Shirakashi, and Y. Takemura  
“Planar-type Ferromagnetic Tunnel Junctions Fabricated by SPM Local Oxidation”  
17th International Conference on Magnetism (ICM-17), August 20-25, 2006, Kyoto,  
Japan. Abstract Book, pp. 581.
  
- 5) Y. Tomoda, S. Nishimura, J. Shirakashi, and Y. Takemura  
“Local Oxidation Nanolithography of Co Thin Films Using SPM”  
10th Joint MMM-Intermag Conference, January 7-11, 2007, Baltimore, Maryland,  
USA. Abstract Book, pp. 253.

- 6) Y. Tomoda, K. Takahashi, M. Hanada, W. Kume, and J. Shirakashi  
“Fabrication of Nanogap Electrodes by Field-Emission-Induced Electromigration”  
The 2008 International Conference on Nanoscience + Technology (ICN+T 2008),  
July 21-25, 2008, Keystone, CO, USA. Abstract Book, pp. 75.
  
- 7) K. Takahashi, Y. Tomoda, S. Itami, and J. Shirakashi  
“Control of Channel Resistance on Metal Nanowires by Electromigration Patterning  
Method”  
The 2008 International Conference on Nanoscience + Technology (ICN+T 2008),  
July 21-25, 2008, Keystone, CO, USA. Abstract Book, pp. 94.
  
- 8) Y. Tomoda, K. Takahashi, M. Hanada, W. Kume, S. Itami, T. Watanabe, and J.  
Shirakashi  
“Magnetoresistance Properties of Planar-Type Tunnel Junctions with Ferromagnetic  
Nanogap System Fabricated by Electromigration Method”  
International Magnetics Conference 2009 (Intermag 2009), May 4-8, 2009,  
Sacramento, CA, USA. Abstract Book, pp. 135.
  
- 9) Y. Tomoda, M. Hanada, W. Kume, S. Itami, T. Watanabe, and J. Shirakashi  
“Fabrication of Planar-Type Ferromagnetic Tunnel Junctions Using Electromigration  
Method and Its Magnetoresistance Properties”  
International Conference on Magnetism 2009 (ICM 2009), July 26-31, 2009,  
Karlsruhe, Germany. Abstract Book, pp. 293.
  
- 10) W. Kume, Y. Tomoda, M. Hanada, and J. Shirakashi  
“Fabrication of Single-Electron Transistors Using Field-Emission-Induced  
Electromigration”  
International Conference on Nanoscience and Technology China 2009  
(ChinaNANO 2009), September 1-3, 2009, Beijing, China. Abstract Book,  
pp. 65-66.



- 11) T. Watanabe, Y. Tomoda, and J. Shirakashi  
“Magnetoresistance Properties of Planar-Type Ferromagnetic Tunnel Junctions with Vacuum Barriers Fabricated by Field-Emission-Induced Electromigration”  
International Conference on Nanoscience and Technology China 2009 (ChinaNANO 2009), September 1-3, 2009, Beijing, China. Abstract Book, pp. 327-328.
- 12) S. Itami, Y. Tomoda, R. Yasutake, and J. Shirakashi  
“Influence of Feedback Parameters on Resistance Control of Metal Nanowires by Stepwise Feedback-Controlled Electromigration”  
International Conference on Nanoscience and Technology China 2009 (ChinaNANO 2009), September 1-3, 2009, Beijing, China. Abstract Book, pp. 460.

< Domestic Conferences >

- 1) 柴田義大、佐藤 寛、友田悠介、伊東良太、竹村泰司、白樫淳一  
“タッピングモードを用いた SPM 局所酸化法による強磁性体へのナノリソ  
グラフィ”  
第 28 回日本応用磁気学会 学術講演会、21a-G-5、2004 年 9 月 21-24 日、沖縄
- 2) 友田悠介、伊東良太、柴田義大、佐藤 寛、竹村泰司、白樫淳一  
“SPM 局所酸化法により作製したプレーナ型強磁性トンネル接合ダイオード”  
第 28 回日本応用磁気学会 学術講演会、22p-F-4、2004 年 9 月 21-24 日、沖縄
- 3) 柴田義大、友田悠介、白樫淳一、竹村泰司  
“タッピングモード SPM による強磁性体への局所酸化ナノリソグラフィ”  
第 52 回応用物理学関係連合講演会、31p-YD-13、2005 年春季、埼玉
- 4) 柴田義大、友田悠介、白樫淳一、竹村泰司  
“Fe 極薄膜への SPM 局所酸化ナノリソグラフィ”  
第 29 回日本応用磁気学会 学術講演会、20p-D-4、2005 年 9 月 19-22 日、長野
- 5) 友田悠介、柴田義大、白樫淳一、竹村泰司  
“プレーナ型強磁性トンネル接合ダイオードにおける磁気抵抗効果”  
第 29 回日本応用磁気学会 学術講演会、22p-F-11、2005 年 9 月 19-22 日、長野
- 6) 友田悠介、西村信也、白樫淳一、竹村泰司  
“Co 極薄膜への SPM 局所酸化ナノリソグラフィ法の適用”  
第 30 回日本応用磁気学会 学術講演会、11aD-10、2006 年 9 月 11-14 日、島根
- 7) 荻野拓海、西村信也、友田悠介、白樫淳一  
“SPM 局所摩擦場による Si に対する 20 nm 以下級スクラッチリソグラフィ”  
第 54 回応用物理学関係連合講演会、29p-S-7、2007 年春季、神奈川

- 8) 高橋佳祐、伊丹壯一郎、友田悠介、白樫淳一  
“電圧フィードバックエレクトロマイグレーションにおける制御パラメータの検討”  
第 69 回応用物理学学会学術講演会、4a-H-4、2008 年秋季、愛知
- 9) 花田道庸、友田悠介、久米彌、高橋佳祐、白樫淳一  
“電界放射電流誘起型 EM を用いたナノギャップ電極の特性制御における電極形状の検討”  
第 69 回応用物理学学会学術講演会、4a-H-5、2008 年秋季、愛知
- 10) 久米彌、友田悠介、花田道庸、高橋佳祐、白樫淳一  
“電界放射電流誘起型エレクトロマイグレーションによる単電子トランジスタ作製条件の検討”  
第 69 回応用物理学学会学術講演会、4a-H-6、2008 年秋季、愛知
- 11) 友田悠介、高橋佳祐、花田道庸、久米彌、伊丹壯一郎、白樫淳一  
“プレナー型強磁性ナノ構造におけるナノギャップの作製と磁気抵抗特性”  
第 69 回応用物理学学会学術講演会、4a-H-7、2008 年秋季、愛知
- 12) 友田悠介、久米彌、花田道庸、高橋佳祐、白樫淳一  
“電界放射電流誘起型エレクトロマイグレーション法による単電子トランジスタの作製”  
電子情報通信学会 電子デバイス研究会 (ED)/ シリコン材料・デバイス研究会 (SDM)「機能ナノデバイスおよび関連技術」、2009 年 2 月 26 日-27 日、北海道
- 13) 友田悠介、高橋佳祐、花田道庸、久米彌、伊丹壯一郎、渡邊敬登、白樫淳一  
“エレクトロマイグレーションによる強磁性ナノギャップの作製と磁気抵抗特性”  
第 56 回応用物理学関係連合講演会、31a-L-9、2009 年春季、茨城
- 14) 花田道庸、友田悠介、久米彌、上野俊介、高橋佳祐、白樫淳一  
“電界放射電流誘起型 EM により作製されたナノギャップの検討”  
第 56 回応用物理学関係連合講演会、1p-ZQ-1、2009 年春季、茨城

- 15) 久米彌、友田悠介、上野俊介、花田道庸、高橋佳祐、白樫淳一  
“電界放射電流誘起型 EM でのナノギャップ電極の特性制御における電圧増加幅の検討”  
第 56 回応用物理学関係連合講演会、1p-ZQ-2、2009 年春季、茨城
- 16) 上野俊介、久米彌、花田道庸、友田悠介、高橋佳祐、白樫淳一  
“電界放射電流誘起型 EM を用いたナノギャップ電極の同時特性制御の検討”  
第 56 回応用物理学関係連合講演会、1p-ZQ-3、2009 年春季、茨城
- 17) 伊丹壮一郎、高橋佳祐、友田悠介、安武龍太郎、白樫淳一  
“電圧フィードバック EM での抵抗制御特性に対する電圧制御パラメータの効果”  
第 56 回応用物理学関係連合講演会、1p-ZQ-5、2009 年春季、茨城
- 18) 友田悠介、渡邊敬登、花田道庸、久米彌、伊丹壮一郎、白樫淳一  
“電界放射電流誘起型 EM により作製した強磁性トンネル接合における磁気抵抗特性”  
第 70 回応用物理学学会学術講演会、10a-ZD-24、2009 年秋季、富山
- 19) 安武龍太郎、伊丹壮一郎、友田悠介、白樫淳一  
“電圧フィードバック EM におけるマイグレーションメカニズムの検討”  
第 70 回応用物理学学会学術講演会、10a-ZH-2、2009 年秋季、富山
- 20) 伊丹壮一郎、友田悠介、安武龍太郎、白樫淳一  
“電圧フィードバック EM におけるチャンネル形状狭窄過程の検討”  
第 70 回応用物理学学会学術講演会、10a-ZH-3、2009 年秋季、富山
- 21) 滝谷和聡、友田悠介、久米彌、花田道庸、渡邊敬登、白樫淳一  
“電界放射電流誘起型 EM によるナノスケールデバイスの作製(1): 単電子トランジスタの検討”  
第 70 回応用物理学学会学術講演会、10a-ZH-4、2009 年秋季、富山

- 22) 渡邊敬登、友田悠介、花田道庸、久米彌、伊丹壯一郎、滝谷和聡、白樫淳一  
“電界放射電流誘起型 EM によるナノスケールデバイスの作製(2): 強磁性トンネル接合の検討”  
第 70 回応用物理学学会学術講演会、10a-ZH-5、2009 年秋季、富山
- 23) 上野俊介、友田悠介、久米彌、花田道庸、渡邊敬登、白樫淳一  
“電界放射電流誘起型 EM による強磁性トンネル接合の集積化技術の検討”  
第 70 回応用物理学学会学術講演会、10a-ZH-6、2009 年秋季、富山
- 24) 上野俊介、友田悠介、久米彌、滝谷和聡、渡邊敬登、白樫淳一  
“電界放射電流誘起型エレクトロマイグレーションによる単電子トランジスタの集積化”  
電子情報通信学会 電子デバイス研究会 (ED)/シリコン材料・デバイス研究会 (SDM)「機能ナノデバイスおよび関連技術」、2010 年 2 月 22 日-23 日、沖縄
- 25) 滝谷和聡、友田悠介、渡邊敬登、久米彌、上野俊介、白樫淳一  
“電界放射電流誘起型エレクトロマイグレーション法によるプレーナ型強磁性トンネル接合の作製”  
電子情報通信学会 電子デバイス研究会 (ED)/シリコン材料・デバイス研究会 (SDM)「機能ナノデバイスおよび関連技術」、2010 年 2 月 22 日-23 日、沖縄
- 26) 安武龍太郎、友田悠介、伊丹壯一郎、久米彌、厚母息吹、白樫淳一  
“分割型電圧フィードバック EM によるマイグレーション過程の検討”  
第 57 回応用物理学関係連合講演会、19a-P10-4、2010 年春季、神奈川
- 27) 厚母息吹、友田悠介、伊丹壯一郎、安武龍太郎、白樫淳一  
“分割型電圧フィードバック EM による金属ナノチャネルの抵抗制御性の向上に関する研究”  
第 57 回応用物理学関係連合講演会、19a-P10-5、2010 年春季、神奈川
- 28) 伊丹壯一郎、友田悠介、安武龍太郎、厚母息吹、白樫淳一  
“分割型電圧フィードバックエレクトロマイグレーションによる Ni ナノチャネルの磁気抵抗特性制御”  
第 57 回応用物理学関係連合講演会、19a-P10-6、2010 年春季、神奈川

- 29) 滝谷和聡、友田悠介、久米彌、上野俊介、花田道庸、渡邊敬登、白樫淳一  
“電界放射電流誘起型 EM における新たな通電手法の検討”  
第 57 回応用物理学関係連合講演会、19a-P10-9、2010 年春季、神奈川県
- 30) 花田道庸、友田悠介、久米彌、上野俊介、滝谷和聡、白樫淳一  
“パッシベーション処理を施したナノギャップ電極における電界放射電流誘起型 EM による特性制御の検討”  
第 57 回応用物理学関係連合講演会、19a-P10-10、2010 年春季、神奈川県
- 31) 久米彌、友田悠介、花田道庸、上野俊介、滝谷和聡、白樫淳一  
“電界放射電流誘起型 EM により作製した単電子トランジスタの特性制御”  
第 57 回応用物理学関係連合講演会、19a-P10-11、2010 年春季、神奈川県
- 32) 上野俊介、友田悠介、久米彌、滝谷和聡、花田道庸、白樫淳一  
“電界放射電流誘起型 EM による単電子トランジスタの集積化の検討”  
第 57 回応用物理学関係連合講演会、19a-P10-12、2010 年春季、神奈川県

< Others >

- 1) Y. Tomoda, Y. Shibata, J. Shirakashi and Y. Takemura  
“Magnetoresistance effect of planar-type ferromagnetic tunnel junctions”  
Virtual Journal of Nanoscale Science & Technology, **13** (18) May 8, 2006.
  
- 2) 西村信也、友田悠介、白樫淳一  
“動的探針制御による SPM 局所酸化ナノリソグラフィー”  
エスアイアイ・ナノテクノロジー株式会社主催  
走査型プローブ顕微鏡セミナー2006 ～SPM-FIB-SEM のコラボレーション  
～ 2006年6月29日、東京
  
- 3) Y. Tomoda, S. Kayashima, M. Motoyama, K. Takahashi and J. Shirakashi  
“Magnetoresistance Effect of Planar-Type Ferromagnetic Nanostructures”  
電気通信大学・東京農工大学 第4回合同シンポジウム  
「コヒーレント光科学とナノ未来材料」、P83、2007年12月1日、東京農工大学
  
- 4) 西村信也、友田悠介、白樫淳一、越田信義  
“シリコンへの SPM 微細加工技術”  
科学研究費補助金特定領域研究 「シリコンナノエレクトロニクスの新展開  
ーポストスケーリングテクノロジーー」 第二回成果報告会、P107、  
2008年3月7日-8日、東京
  
- 5) 友田悠介、西村信也、白樫淳一、越田信義  
“強磁性ナノ構造での磁気特性制御”  
科学研究費補助金特定領域研究 「シリコンナノエレクトロニクスの新展開  
ーポストスケーリングテクノロジーー」 第二回成果報告会、P108、  
2008年3月7日-8日、東京

- 6) Y. Tomoda, S. Kayashima, M. Motoyama, K. Takahashi and J. Shirakashi  
“Magnetoresistance Properties of Planar-Type Ferromagnetic Nanostructures”  
文部科学省大学院教育改革支援プログラム「科学立国人材育成プログラム」  
ナノ未来科学研究拠点 2007 年度コロキウム、P18、2008 年 3 月 8 日、  
東京農工大学
- 7) 友田悠介、西村信也、白樫淳一、越田信義  
“半導体・強磁性体へのナノ加工技術の開発とナノデバイス作製への適用”  
科学研究費補助金特定領域研究 「シリコンナノエレクトロニクスの新展開  
—ポストスケーリングテクノロジー—」 第四回全体会議、P106、  
2008 年 8 月 7 日-8 日、名古屋
- 8) 友田悠介、西村信也、白樫淳一、越田信義  
“半導体・強磁性体へのナノスケール加工とデバイス応用”  
科学研究費補助金特定領域研究 「シリコンナノエレクトロニクスの新展開  
—ポストスケーリングテクノロジー—」 第三回成果報告会、P107、  
2009 年 1 月 28 日-29 日、東京
- 9) 友田悠介、久米彌、花田道庸、高橋佳祐、白樫淳一  
“電界放射電流誘起型エレクトロマイグレーション法による単電子トランジ  
スタの作製”  
電子情報通信学会技術研究報告 vol. 108、 No. 437、 ED2008-232  
(SDM2008-224)、pp. 47-52、2009 年 2 月.
- 10) 友田悠介、白樫淳一  
“プレナー型強磁性ナノ構造におけるナノギャップの作製と磁気抵抗特性”  
文部科学省大学院教育改革支援プログラム「科学立国人材育成プログラム」  
合宿コロキウム(研修会)、2009 年 3 月 7 日-8 日、ホテル エバーグリーン富士



- 11) K. Takahashi, Y. Tomoda, S. Itami and J. Shirakashi  
“Control of Channel Resistance on Metal Nanowires by Electromigration Patterning Method”  
Virtual Journal of Nanoscale Science & Technology, **19** (15) April 13, 2009.
- 12) 西村信也、友田悠介、白樫淳一、越田信義  
“半導体・強磁性体へのナノスケール加工とデバイス応用”  
科学研究費補助金特定領域研究 「シリコンナノエレクトロニクスの新展開—ポストスケーリングテクノロジー—」 第六回全体会議、P106、  
2009年8月6日-7日、名古屋
- 13) Y. Tomoda, T. Watanabe, M. Hanada, W. Kume, S. Itami, and J. Shirakashi  
“Magnetoresistance Properties of Planar-Type Ferromagnetic Tunnel Junctions Fabricated by Field-Emission-Induced Electromigration”  
電気通信大学・東京農工大学 第6回合同シンポジウム  
「ナノ未来材料とコヒーレント光科学」、T76、2009年12月5日、東京農工大学
- 14) 太田敢行、Bernard GELLOZ、友田悠介、西村信也、白樫淳一、越田信義  
“シリコンナノ構造の電子機能”  
科学研究費補助金特定領域研究 「シリコンナノエレクトロニクスの新展開—ポストスケーリングテクノロジー—」 第四回成果報告会、P106、  
2010年1月19日-20日、東京
- 15) 上野俊介、友田悠介、久米彌、滝谷和聡、渡邊敬登、白樫淳一  
“電界放射電流誘起型エレクトロマイグレーションによる単電子トランジスタの集積化”  
電子情報通信学会技術研究報告 **vol. 109**、No. 422、ED2009-202 (SDM2009-199)、pp. 35-39、2010年2月.
- 16) 滝谷和聡、友田悠介、渡邊敬登、久米彌、上野俊介、白樫淳一  
“電界放射電流誘起型エレクトロマイグレーション法によるプレーナ型強磁性トンネル接合の作製”  
電子情報通信学会技術研究報告 **vol. 109**、No. 422、ED2009-203 (SDM2009-200)、pp. 41-45、2010年2月.

17) 友田悠介

第1回東京農工大学奨励奨学金奨学生

平成18年7月18日 授与

18) 友田悠介

文部科学省 大学院教育改革支援プログラム

「科学立国人材育成プログラム」 リサーチ・アシスタント

平成19年11月1日～平成20年3月31日

平成21年4月8日～平成22年3月31日

19) 友田悠介

独立行政法人日本学術振興会 特別研究員

平成20年度採用 (DC2)

平成20年4月1日～平成22年3月31日

< Awards >

- 1) T. Watanabe, Y. Tomoda, and J. Shirakashi  
(Selected for the Best Poster Award of ChinaNANO 2009)  
"Magnetoresistance Properties of Planar-Type Ferromagnetic Tunnel Junctions with Vacuum Barriers Fabricated by Field-Emission-Induced Electromigration"  
International Conference on Nanoscience and Technology China 2009 (ChinaNANO 2009), September 1-3, 2009, Beijing, China.
  
- 2) Y. Tomoda, T. Watanabe, M. Hanada, W. Kume, S. Itami, and J. Shirakashi  
(Selected for the Poster Award of the Symposium)  
"Magnetoresistance Properties of Planar-Type Ferromagnetic Tunnel Junctions Fabricated by Field-Emission-Induced Electromigration"  
東京農工大学・電気通信大学 第6回合同シンポジウム  
「ナノ未来材料とコヒーレント光科学」、T76、2009年12月5日、東京農工大学
  
- 3) 上野俊介、友田悠介、久米彌、花田道庸、滝谷和聡、白樫淳一  
“電界放射電流誘起型 エレクトロマイグレーションによる単電子トランジスタの集積化”  
電子情報通信学会技術研究報告、vol. 109、 no. 422、 ED2009-202 (SDM2009-199)、 pp. 35-39、 2010年2月。  
(電子情報通信学会電子デバイス研究会論文発表奨励賞)